A COMPREHENSIVE SIMULATION-BASED METHODOLOGY FOR THE DESIGN AND OPTIMIZATION OF ORTHOPAEDIC INTERNAL FIXATION IMPLANTS

A Dissertation

Presented to

The Faculty of the Graduate School

At the University of Missouri

In Partial Fulfillment

Of the Requirements for the Degree

Doctor of Philosophy

By

JOSHUA ARNONE

Dr. A. Sherif El-Gizawy, Dissertation Supervisor

MAY 2011

The undersigned, appointed by the dean of the Graduate School,

have examined the dissertation entitled

A Comprehensive Simulation-Based Methodology for the Design and Optimization of Orthopaedic Internal Fixation Implants

Presented by Joshua Arnone

A candidate for the degree of

Doctor of Philosophy

And hereby certify that, in their opinion, it is worthy of acceptance.

Dr. A. Sherif El-Gizawy

Dr. Jinn-Kuen Chen

Dr. Yuwen Zhang

Dr. Sheila Grant

Dr. Carol Ward

Dr. Gregory Della Rocca

Dr. Brett Crist

To Annie, my wife and best friend. Thank you for your support and encouragement.

ACKNOWLEDGEMENTS

First, I would like to thank Dr. Sherif El-Gizawy for going far above and beyond the call of duty of a research advisor. Additionally, I thank Dr. Carol Ward for her time, expertise, and willingness to collaborate with me since I first started orthopaedic-related research as an undergrad. I also owe much gratitude to Drs. Gregory Della Rocca and Brett Crist for their support and insight into the needs of orthopaedic trauma surgery.

I would also like to thank the University of Missouri Research Board (MURB) for partially funding the study. I also thank Lyman Jellema and Dr. Yohannes Haile Selassie of the Cleveland Museum of Natural History for providing access to the Hamann-Todd collection of human femur specimens. Much gratitude is also extended to Dr. Charles Kunos and staff of the Case Western University Hospital Department of Radiation Oncology for sharing their CT scanner and expertise.

I thank John Roche of Hubble Power Systems, Centralia, MO, for providing materials, access to machinery, and expertise during the prototyping phase. I also thank Rex Gish, Mike Scheller, and Shane Coral for assistance during the experimental phase. Additionally, I thank the National Center for Supercomputing Applications (NCSA), located at the University of Illinois at Urbana-Champaign, for providing supercomputer access. Finally, I thank Dr. J. Michael Plavcan, Dr. Jackson Cothren, and the Center for Advanced Spatial Technologies at the University of Arkansas for collaboration and training on Polyworks software.

TABLE OF CONTENTS

TABLE OF FIGURES

TABLE OF TABLES

ABSTRACT

Internal fixation implants are widely used by orthopaedic surgeons to stabilize various types of fractures in injured patients. However, the irregular geometry of the human skeletal system, as well as the significant variation in the size and shape of bones among the population, pose great challenges in efficiently and effectively designing such devices. As a result, the need for improvement in regard to performance and fit is evident in many current internal fixation implants, particularly for high load-bearing regions such as the femur. For this reason, a comprehensive methodology was developed to design and optimize implants with maximal structural integrity and contour fitting among the population, while minimizing its influence on human biomechanics. The systematic methodology uniquely employs both new and existing techniques in medical imaging analysis, non-linear finite element methods, and optimization to obtain optimal designs prior to experimental testing. Its efficacy was demonstrated using two case studies involving the design of internal fixation implants used to stabilize various femoral shaft fractures: intramedullary nailing and locking plate systems. Comparison of finite element results – from simulated physiological loading conditions and loads induced by "virtual surgery" – among the optimized implants and those currently used in the operating room showed much improvement in regard to reliability, fit, and alteration of natural biomechanics. Subsequent experimental testing verified that the results predicted by the developed simulation-based methodology

represented actual physiological scenarios within acceptable percent error and were valid for design purposes.

CHAPTER I. INTRODUCTION

Conventional Design Process for Orthopaedic Internal Fixation Implants

Internal fracture fixation implants are commonly used to treat trauma injuries by providing fracture stability during recovery. In addition to satisfying biocompatibility requirements established by the U.S Food and Drug Administration (FDA), fixation implants must have sufficient mechanical integrity to withstand physiological loading conditions present at the fracture site. Post-operative static, dynamic, and cyclic forces typically present at the site all contribute in generating stress in the implant. Additionally, insertion techniques can induce high stresses in the implant as well as in surrounding bone tissue. These post-operative and insertion-induced stresses can potentially lead to fracture instability due to mechanical failure of the implant and/or bone.

Conventionally, the process of orthopaedic implant design is based on computer aided design (CAD), prototyping, and experimental testing in order to assess implant performance and biomechanical behavior of the treated skeletal region. This approach is iterative in nature and requires numerous iterations – or "redesigns" – to converge to a final optimum solution. In most cases, an "acceptable" solution is chosen before an optimum is reached – as is generally true for product development in any industry.

Many current implant designs and orthopaedic techniques are "standard" because they have been used in the past with some success, although they may not be optimum. The rigorous path one must take to attain FDA approval for a class III

implantable device does account for this to some extent. Prototyping and experimental costs, as well as limitations in a current design approach that's largely based on trial-by-error, also play a role in impeding the advancement of implant design. Further complicating the design process, the size and shape of bones differ significantly among individuals. Yet the more closely an implant conforms to the form of the local bone geometry, the more successful the repair will be in the short and long term. Developing implants that can accommodate this large degree of skeletal variation proves to be among the greatest challenges for implant design.

Recently, the use of finite element methods (FEM) for structural analysis has been adopted by many in the orthopaedic market as a standard technique for implant design. This allows engineers to predict implant/bone behavior earlier during the design process and to make engineering decisions accordingly. However, FEM for orthopaedic applications requires not only CAD modeling of the implant, but also modeling of the surrounding local bone tissue. Although commercial software is available for generating bone models from CT scans, the process itself is time-consuming.

Simulation-Based Design and Optimization

In light of the present-day inefficiencies of implant design methods, a comprehensive simulation-based approach is proposed to not only design, but also optimize, implantable fixation devices prior to experimental testing. The approach integrates design, analysis, and optimization into a digital computer-aided system. The time and costs required to design, analyze, and optimize a product can be significantly

less than traditional prototyping and experimental methods based on trial-by error. This is largely due to the reduction in manufacturing time and costs for multiple prototypes, material costs, experimental testing time and costs, and time required to analyze experimental results and make engineering decisions based on those results.

The proposed simulation-based approach does not replace the need for experimental verification of a product; it allows the engineers to begin the experimental phase with a product design that is already optimized – or at least very close to the optimum. The experimental phase is therefore not used as an iterative trial-by-error optimization process, but rather as for final verification that the product meets the objective and satisfies all design constraints.

The three core techniques used in the proposed approach are CAD/medical imaging, FEM, and numerical optimization. Each of these techniques have already been applied to orthopaedic product development to an extent (as outlined in the following chapter); however, the simulation-based approach addresses many current inefficiencies and provides a systematic, comprehensive design and optimization process applicable to any type of orthopaedic implantable device. The process is also flexible to allow for adaptation to specific needs among various implant types.

A unique feature of the approach is that implant optimization applies to both structural performance and fit. The intent is to provide a methodology that aids in determining the optimum implant shape(s), size(s), and material(s) that best accommodate the vast geometry variation among patients and provides adequate structural stability while minimizing the effect the implant has on patient biomechanics.

Details concerning each step of the methodology are outlined in Chapter 3, and the efficacy of the approach is demonstrated using two case studies in Chapter 4.

CHAPTER II. BACKGROUND & LITERATURE REVIEW

Medical Imaging & Computer-Aided Design

Computer-aided design (CAD) has been an essential tool for product design engineers since its conception in the 1960's, particularly since the 1980's with the development of graphical 3D solid modeling. With the rapid expansion of computational technology, the application of CAD in the biomedical industry has grown, leading to many novel advances in the industry. The technique, in its most simplistic form, allows for graphical 3D representation and manipulation of design concepts, as well as the generation of 2D technical drawings, permitting more efficient communication between the design engineers, technicians, and physicians.

Not only is CAD useful for modeling new product designs, but also for digitally reconstructing patient-specific musculoskeletal tissue. Medical imaging modalities, such as computed tomography (CT) and magnetic resonance imaging (MRI) scans, coupled with image segmentation and surface generating software, allow for accurate digital reconstruction of organ models [1-9]. Most reconstruction methods can be characterized in two major categories: the volume-based approach and the contour-based approach [7, 10]. The volume-based approach uses the marching cube method to generate triangular-meshed "iso-surfaces" [11, 12]. This technique has been widely adopted for visualizing 3D medical images because of its high resolution, computational efficiency, and its data structure [7]. However, because of the large number of non-uniform, skewed triangles that comprise the iso-surfaces, the marching cube method is

not suitable for numerical simulation and manufacturing purposes without extensive post-processing [7].

In contrast, the contour-based approach extracts cross-sectional surface boundaries of the tissue(s) from each of the medical images comprising a particular scan. The surface boundaries can be obtained by either manual selection/tracing [13] or semi-automatic methods based on defining initial voxel thresholds [14-20] or edge detection algorithms [21-23]. Once the series of closed-contours are acquired, a 3D boundary is generated by connecting the contours with a triangular meshed or parametric surface. The voxel thresholding/manual segmentation techniques, as well as surface generation, contour interpolation, and smoothing, are discussed in greater detail in chapter 3.

Finite Element Method

The finite element method (FEM) is a powerful numerical technique used to digitally simulate complex physical systems. Simulation systems, including structural, thermal, fluid flow, and electromagnetic, can be mathematically defined as "responses of a problem domain subject to environmental conditions" [24]. Environmental conditions that apply to the problem domain's boundary surfaces, such as external loading (forces, heat flux, current, mass flow, etc.) and constraints (displacement, temperature, voltage, etc.), are also known as boundary conditions. However, environmental conditions can also be distributed throughout the volume of the domain which include gravitational attraction, inertial forces, and temperature change.

The scope of this dissertation is concerned with structural analysis, where the deformation of the domain (3D model) is determined by calculating the displacement field

$$\{u_i\} = \{u_{xx} + u_{yy} + u_{zz}\}, \tag{I}$$

the strain field

$$\{\varepsilon_i\} = \begin{bmatrix} \epsilon_{xx} & \epsilon_{xy} & \epsilon_{xz} \\ \epsilon_{yx} & \epsilon_{yy} & \epsilon_{yz} \\ \epsilon_{zx} & \epsilon_{zy} & \epsilon_{zz} \end{bmatrix}, \tag{II}$$

and the stress field

$$\{\sigma_i\} = \begin{bmatrix} \sigma_{xx} & \sigma_{xy} & \sigma_{xz} \\ \sigma_{yx} & \sigma_{yy} & \sigma_{yz} \\ \sigma_{zx} & \sigma_{zy} & \sigma_{zz} \end{bmatrix} \tag{III}$$

at each spatial location *i* in the domain. The unknown responses of Eqs. (I-III) must satisfy the equilibrium principal

$$\sum F_{x,i} = m_i a_{x,i}\,, \sum F_{y,i} = m_i a_{y,i}\,, \sum F_{z,i} = m_i a_{z,i}\,, \tag{IV}$$

where $\sum F_{n,i}$ is the summation of boundary conditions applied to each domain point *i* in the *n* direction, *m* is the mass of each point *i*, and a_n is the acceleration of each point *i*. For static structural analysis, the equilibrium Eqs. (IV) become

$$\sum F_{x,i} = 0\,, \sum F_{y,i} = 0\,, \sum F_{z,i} = 0\,. \tag{V}$$

Assuming a linear elastic stress-strain relationship, the equilibrium equations can be rewritten as

$$\frac{\partial}{\partial x}\sigma_{xx,i} + \frac{\partial}{\partial y}\sigma_{xy,i} + \frac{\partial}{\partial z}\sigma_{xz,i} + F_{x,i} = 0$$

$$\frac{\partial}{\partial x}\sigma_{xx,i} + \frac{\partial}{\partial y}\sigma_{xy,i} + \frac{\partial}{\partial z}\sigma_{xz,i} + F_{x,i} = 0 \qquad \text{(VI)}$$

$$\frac{\partial}{\partial x}\sigma_{xx,i} + \frac{\partial}{\partial y}\sigma_{xy,i} + \frac{\partial}{\partial z}\sigma_{xz,i} + F_{x,i} = 0$$

where F_n is the environmental condition at each domain point *i*. The assumed linear stress-strain relationships, also known as Hooke's Law, are

$$\varepsilon_{xx,i} = \frac{\sigma_{xx,i}}{E_{xx,i}} - \nu_{xy,i}\frac{\sigma_{yy,i}}{E_{yy,i}} - \nu_{xz,i}\frac{\sigma_{zz,i}}{E_{zz,i}} + \alpha\Delta T_i \,,$$

$$\varepsilon_{yy,i} = \frac{\sigma_{yy,i}}{E_{yy,i}} - \nu_{yz,i}\frac{\sigma_{zz,i}}{E_{zz,i}} - \nu_{xy,i}\frac{\sigma_{xx,i}}{E_{xx,i}} + \alpha\Delta T_i \,, \qquad \text{(VII)}$$

$$\varepsilon_{zz,i} = \frac{\sigma_{zz,i}}{E_{zz,i}} - \nu_{zx,i}\frac{\sigma_{xx,i}}{E_{xx,i}} - \nu_{yz,i}\frac{\sigma_{yy,i}}{E_{yy,i}} + \alpha\Delta T_i \,,$$

$$\varepsilon_{xy,i} = \frac{\sigma_{xy,i}}{G_{xy,i}} \,, \varepsilon_{yz,i} = \frac{\sigma_{yz,i}}{G_{yz,i}} \,, \varepsilon_{xy,i} = \frac{\sigma_{zx,i}}{G_{zx,i}} \,,$$

where $E_{nn,i}$ is the elastic modulus constant in *n* direction for each domain point *i*, $\nu_{mn,i}$ is the Poisson's ratio at each point *i*, and $G_{mn,i}$ is the shear modulus at each point *i*.

Under the assumption of small deformations, the six equations describing the strain-displacement relationships are

$$\varepsilon_{xx,i} = \frac{d}{\partial x}u_{x,i} \;,\; \varepsilon_{yy,i} = \frac{d}{\partial y}u_{y,i} \;,\; \varepsilon_{zz,i} = \frac{d}{\partial z}u_{z,i} \qquad \text{(VIII)}$$

$$\varepsilon_{xy,i} = \frac{\partial}{\partial y}u_{x,i} + \frac{\partial}{\partial x}u_{y,i} \;,\; \varepsilon_{yz,i} = \frac{\partial}{\partial z}u_{y,i} + \frac{\partial}{\partial y}u_{z,i} \;,\; \varepsilon_{zx,i} = \frac{\partial}{\partial x}u_{z,i} + \frac{\partial}{\partial z}u_{x,i} \,.$$

The fifteen governing equations above (Eqs. (VI-VIII)) can be used to solve for the fifteen unknown responses of Eqs. (I-III) for each point in the domain. According to the standard model of particle physics, physical object are actually comprised of an infinite

number of points as there is no limit to how many times a volume can be divided. Therefore, in order to solve the response of a physical system, the governing equations need be applied an infinite number of times in order to represent the entire domain. However, FEM is able to address this issue by dividing continuum objects into a finite number of elements. Responses are calculated at each element vertex, or node, and then interpolated within each element. An element's displacement field $\{u\}_e$, therefore, becomes a function of nodal displacement by

$$\{u\}_e = [N]_e\{d\}_e \,, \tag{IX}$$

where $[N]_e$ is the matrix of interpolative shape functions and $\{d\}_e$ is the displacement of each node corresponding to the element. When shape functions of an element are represented by first order polynomials, the element is referred to being a linear, or lower-order, element. Increasing the polynomial order of an element – resulting in a higher-order element – increases its accuracy. This technique for obtaining a more realistic response is known as p-element convergence. Alternatively, accuracy can be increased by increasing the number of elements comprising the domain (n-element convergence). As either the polynomial order of the shape functions or the number of elements approach infinity, the simulation domain approaches perfect representation.

By discretizing the domain, the static equilibrium system of equations for each element can be represented as

$$[K]_e\{d\}_e = \{F\}_e \tag{X}$$

where $[K]$ is the stiffness matrix (dependent on material constitutive properties) and $\{F\}$ is the vector characterized by the environmental conditions. However, Eq. (IX) is valid

assuming a linear system response. However, most physical systems have non-linear characteristics, meaning that the responses are not linearly proportional to the external loads. Non-linear characteristics can be categorized by large geometric deformations, topology nonlinearity (*eg..* changes in contact status, failure in structural members, etc.), and non-linear material properties (*e.g.* non-linear elasticity, plasticity, hysteresis, creeping, kinematic/isotropic hardening, etc.) [24]. In many cases, non-linearities can be accounted for – or at least approximated – by expressing the stiffness matrix as a function of nodal displacement as deemed appropriate by the particular simulation system:

$$[K(d)]_e\{d\}_e = \{F\}_e \, . \tag{XI}$$

In the case of non-linear analysis, the Newton-Raphson method is typically implemented to solve the response in time increments using a tangent, linearized stiffness matrix at each increment:

$$[K]\{\Delta d\} = \{\Delta F\} \, . \tag{XII}$$

The equilibrium equation is then solved in time increments using

$$[K(d_t)]\{d_t\} = \{F_t\} \, . \tag{XIII}$$

If the residual force of an equilibrium iteration, denoted by

$$F_t^R = (F_{t-1} + \Delta F) - F_t \ , \tag{XIV}$$

is smaller than a user-define criterion, then the time step is said to have converged, otherwise, another equilibrium iteration is initiated for that time step [24].

In the case of orthopaedic implant design and analysis, FEM is valuable for simulating static and dynamic physiological loading conditions on intact, fractured, and treated bone systems. The resulting stress/strain within the implant and surrounding tissue, as well as the interaction behavior between the implant and tissue, can be observed without the need for in vivo trials. FEM also has the advantage of being the only current method able to examine the entire stress/strain field of a device. Since its first application towards orthopaedic research in 1972 [25], FEM has been applied to the design and analysis of fixation implants and prosthetics as well as biomechanical analysis of various bone and artificial tissue [25-52]. Many difficulties have arisen, however, do to the geometric and material complexity of the human body. Applying quality meshes to patient-specific skeletal tissue models in a time-efficient manner which yield reliable, practical results continues to be a challenge.

Optimization

Optimization techniques are an essential tool for new product design. Traditionally, “acceptable” designs were reached through a trial and error process involving CAD, prototyping, and experimental testing. Appropriate design updates relied heavily on engineering experience and understanding of the product market, but were limited by time, available test equipment and materials, and budget. In other words, if the design did not satisfy all the constraints, or if it did but was obviously over-designed, then the engineer would propose modified designs until experimental testing yielding acceptable results. This approach is time-consuming and expensive. Numerical

optimization techniques now make it possible to approach design optima prior to experimentation, saving time and cutting costs.

An optimization problem consists of an objective function(s) and design constraints. The goal is to maximize or minimize the objective function(s) – or in some cases, reach a nominal value – while satisfying design constraints defined by the market, customer requirements, material limitations, manufacturing techniques, etc. For applications involving the design and optimization of orthopaedic implants, appropriate objective functions include minimizing mass, providing nominal stiffness (*i.e.* similar to bone stiffness in order to minimize stress shielding), or maximizing implant fit considering the large variability in human bone geometry. Typical constraints include material yield strength (for implant and bone), dimensional maxima and minima, cost, etc. Fig. 1 illustrates the generic workflow of the optimization process.

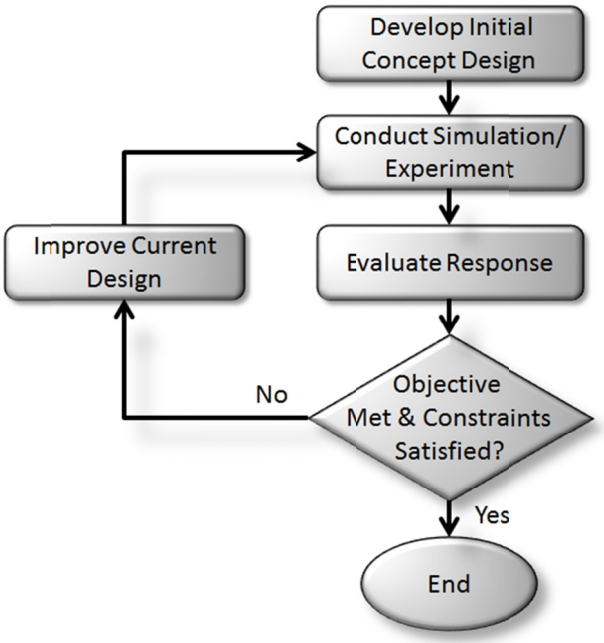

Fig. 1. General steps for design optimization

When integrated with FEM simulations, structural/shape optimization consists of three major modules [53]:

1.) Design model – parameterized geometry domain w/ variables defined

2.) Analysis model – calculates the structural response (FEM)

3.) Optimization algorithm – updates design variables based on response

One of the major challenges with this approach is that a seamless, robust link between the design and analysis models is required for a successful optimization study [53, 54]. As the design model design variables are updated in the study, remeshing is required. If the changes are significantly large, then conventional meshing techniques may not be sufficient without experienced user-input. Several remedies have been proposed and demonstrated such as isogeometric shape optimization [53, 54], using *β*-splines or NURB (non-uniform rational basis spline) surfaces [53, 54], and adaptive meshing [55] (used by commercial software packages such as ANSYS [24], SolidWorks Simulation [56], and Pro/Mechanica [57]).

Common structural optimization algorithms currently implemented in commercial and user-developed software include gradient-based algorithms, such as sequential quadratic programming (SQP) and gradient projection (GDP), and genetic algorithm (GA) [58-60].

Topology optimization, a variant of shape optimization, takes a slightly different approach to optimize structures. This method is concerned with "laying out material in an optimal manner", whereas the previously described approach is more dependent on

the initial design variables (*i.e.* number/orientation of sides, holes, and other features are not permanent) [61]. Techniques for solving FEM-integrated topology optimization include the solid isotropic material with penalization (SIMP) method [61], topology optimization by penalty (TOP) method [62], and dynamic implicit boundary-based moving superimposed finite element method (s-FEM) [63].

Several studies have applied structural optimization techniques in the field of orthopaedic implant design. Kayabasi *et al*. applied a numerical shape optimization technique integrated with the finite element method to the design and analysis of a hip implant [64]. Gefen used manual optimization techniques with structural finite element methods to analyze fixation screw features, materials, and coatings [65]. Gerhart *et al.* developed a purely experimental model system for producing, testing, and optimizing particulate composites for structural tissue engineering [66]. Ueda *et al*. utilized the Taguchi fractional factorial method to determine the optimal levels of three design factors of a surgical drill and their percentage contribution to performance [67]. Several popular commercial CAD/FEA software packages, such as SolidWorks and ANSYS Workbench, have adopted a similar design of experiments (DoE) approach for structural optimization [24, 56]. Although the techniques exist, it is not apparent that automated structural optimization has been successfully applied to the design of internal fracture fixation implants for the purpose of minimizing implant mass while satisfying design constraints associated with the factor of safety.

Two recent studies have analyzed and quantified implant/bone fit of internal fixation plates for the tibia [68, 69]: 1.) Goyal *et al.* applied manual fitting and fixation

techniques using currently-available tibial plates on a set of 101 cadaver specimens. Their method, based on trial-and-error, was used to analyze and quantify anatomic fit in the sagittal, coronal, and axial planes [68]; 2.) Schmutz *et al*. developed an alternative semi-automatic approach for analyzing implant fit and demonstrated it using 21 CT data sets. Results of their approach suggested that current tibial plates adequately fit only 19% of the study samples [69]. Both studies affirmed that human bone geometry variation has a significant effect on implant contour fit. However, to the best of the author's knowledge, only one study has been conducted on optimizing implant/bone fit [70]. Its scope was concerned with the development of an optimal implant contour with suitable fit for the maximum number of patients considering human bone variability. The technique adopted for this approach was based on level-set segmentation to generate a statistical shape model representing a target population [70]. The optimization loop, however, still required manual interpretation of the fit assessment and subsequent manual design updates.

Optimization techniques have also been applied to simulate the phenomenon of bone remodeling [71, 72]. According or Wolff's law, formulated in the 19th century and still widely accepted, bone adapts to changing mechanical stimulation in order to optimize energy expenditure by minimizing mass and strain [71-73]. An improved understanding of the phenomenon and how it affects the interaction between bone and internal fixation implants – before and after full recovery – will lead to improved implant design by reducing bone atrophy due to implant-induced stress shielding. As a result, the quality of patient care would increase, and costs associated with secondary

operations due to long-term bone atrophy will be minimized. Additionally, it may help develop improved structural optimization methods, as demonstrated by Nowak [71] and Harrigan *et al*. [72], which could be applied to implant design.

The proposed optimization methodology is unique in that it is the first to address both fit and structural optimization and does so without manual updating of design variables.

CHAPTER III. METHODOLOGY

The flowchart shown in fig. 2 illustrates the simulation-based methodology proposed for the design and optimization of orthopaedic implants. Although the comprehensive process is systematic in nature, there exists a significant degree of freedom in exactly how the steps are carried out for a specific application and what software packages are used. The methodology is open-ended and allows for the adaptation to various design scenarios. The ultimate goal is to obtain a design that is as close to optimal as possible prior to prototyping and testing.

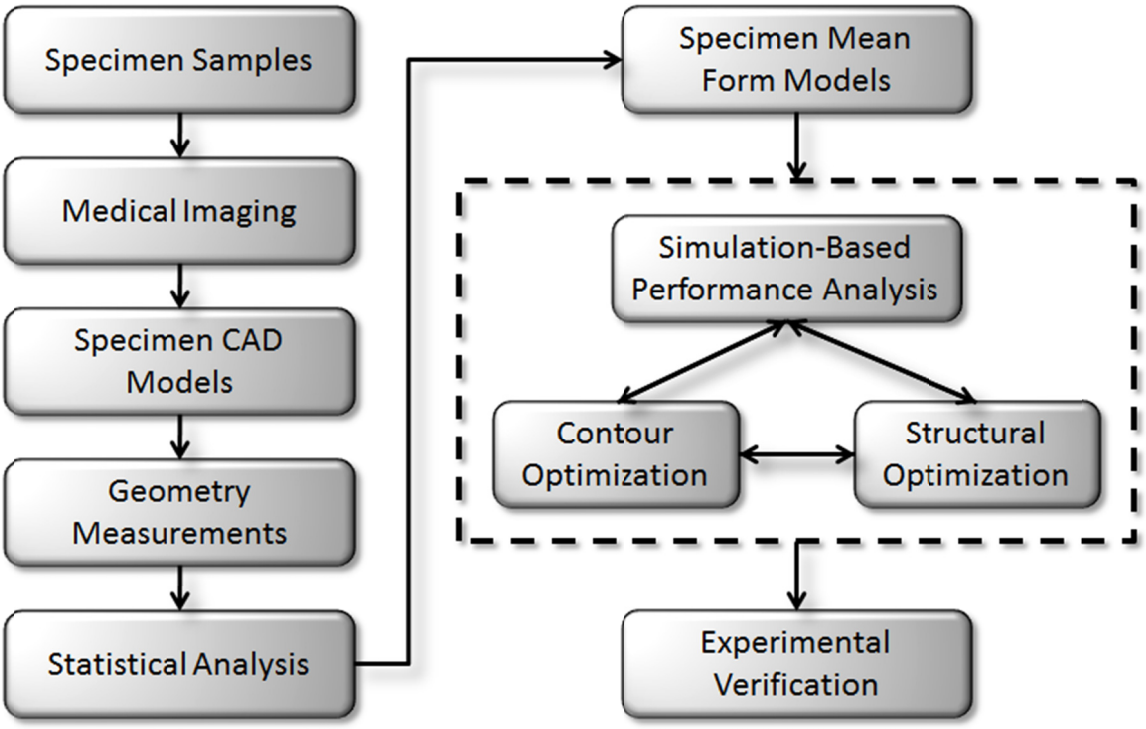

Fig. 2. Design methodology flowchart

1. Specimen Samples

An understanding of human skeletal variation is vital for the successful design of orthopaedic instrumentation. Patient variation occurs not just in physiological, hormonal, molecular, and behavioral responses to normal activity, disease, and trauma, but also in basic gross anatomy. For orthopaedic applications, osteological variation is highly important as the same implant design may perform differently for various patients. It is widely recognized that size variation needs to be considered, but skeletal shape (*e.g.* curvature, proportion, etc.) is another key way in which individuals differ. Size and shape variation are partly functions of race, sex, and age, as well as more random individual factors. Quantifying skeletal variation provides an important foundation for designing implantable fixation devices that accommodate the entire population.

Skeletal morphology can be visualized in a number of ways thanks to new imaging modalities. Clinically, X-ray computed tomography (CT) scan technology can be used to generate 3D images of bones. These can in turn be processed and converted to surface models, including internal as well as external geometries. Despite the risks inherent in any radiographic imaging modality, this is the only reliable way to obtain accurate 3D images of a patient's skeletal anatomy. Thus CT images are currently the most effective way to assess individual patient anatomy for the purpose of developing custom patient-specific instrumentation; however, the clinical approach is less

promising for broader considerations of skeletal variation required for mass-produced instrumentation.

For determining optimal shapes and sizes of implantable devices, great promise lies in the use of skeletal collections located in museums. The Hamann-Todd Osteological Collection in Cleveland, Ohio, contains approximately 3,000 human skeletons from the early 19th century in rural Cleveland. Similarly, the Terry Collection is another from the 19th century that also catalogs skeletons by sex and race. Other skeletal collections in the US and around the world are also available and represent various human populations. Skeletal variation can be studied in these specimens directly – and without patient risk.

2. Medical Imaging

Once the specimen sample are collected, digital 3D models can then be generated via image segmentation techniques using commercial, open source, or user-developed software. However, medical imaging techniques, such as CT scanning, are required to digitize the samples before the models can be generated. The images are characterized as a 3-D array of voxel intensity data, where each voxel intensity value represents the tissue density at a finite location. The more voxels in each CT slice (or 2-D layer, usually orientated in the axial direction), the higher the image's resolution will be. Additionally, the smaller the slice thickness, the higher the resolution will be in the sagittal and coronal planes. The image data is typically saved as a series of DICOM

(digital imaging and communications in medicine) files, with each file representing a 2-D slice of the 3-D array.

Commercial software packages such as Amira (Visage Imaging, 2011) and Mimics (Materialize, 2011) can be used to segment the voxel date into regions of cortical bone, cancellous bone, and other various tissue types. First, once the series of DICOM files are loaded into the program, built-in automated tools can be used to make the initial selection of the type of tissue(s) desired to be modeled. This is accomplished by defining a voxel intensity range that represents the tissue, and then selecting which continuous region(s) of tissue to which it applies. Alternatively, the voxel intensity range can be applied to the entire image.

With either of these automated techniques, it is highly probable that numerous unwanted small holes will be present within the segmented voxel region. Additionally, unwanted islands may be selected outside of the desired bone tissue region. These undesirable artifacts require a second segmentation phase involving manual selection/removal techniques. This is accomplished by viewing each slice layer-by-layer – in all three Cartesianal orientations – and performing the necessary "touch-ups."

For bone tissue modeling, manual segmentation is especially crucial for cancellous bone and thin cortical bone regions. Cancellous bone is inherently porous, giving it a non-uniform density. In many cases, particularly when generating bone models for the purpose of finite element simulations, it is more desirable to generate solid continuum models where porosity is represented by effective material properties acquired through experimental testing. Additionally, bone tissue geometry

measurements are on the macro-scale and do not require porosity to be modeled. Therefore, in nearly all applications for orthopaedic implant design, the pores within cancellous bone regions can be filled.

Holes are frequently present within thin-walled regions of cortical bone following automated image segmentation techniques, particularly with low resolution images or relatively large slice thicknesses compared to the size of the bone features. Additionally, singularities – where the inner and outer surfaces touch at a point – are often present in the surface model generated from the segmented data. This occurs when adjacent segmented voxel regions within a CT slice (from any view orientation) only touch at a corner shared by two of the voxels – as is common for cortical wall thicknesses of one or two voxels. These holes and singularities must be filled using the manual segmentation techniques described for cancellous bone in order for quality bone models to be generated.

These segmentation techniques using commercial software requires expensive software license fees to accomplish this through time-consuming manual and semi-automatic segmentation techniques. Alternatively, open-source programs, such as the Insight Segmentation and Registration Toolkit (ITK), can be downloading and implemented for research purposes free of charge. In any case, current methods do not provide a time- and cost-efficient technique for segmenting thin cortical walls and highly porous bone regions so that unwanted artifacts are present in the final 3-D model. Nor do they provide automated means of removing "islands" created by noise. Therefore, a fully automated method using MATLAB code was developed by the author

in order to reduce the time required for quality image segmentation. Voxel intensity ranges corresponding to cortical and cancellous bone on the CT scan – as well as slice CT slice information and cropping coordinates – are entered as input. The program then reads each dicom file and stores the coordinate locations of voxels representing cortical and cancellous bone in corresponding point cloud matrices. Noise is then removed by filling holes and removing "islands" given the minimum allowed size of each as input. The fully automated procedure is outlined in the steps below and demonstrated using an intact femur CT scan.

Note: the proposed automated segmentation technique was developed after the presented case studies were complete. The tedious nature of the techniques used in the case studies gave rise to the need to develop the automated method.

Step 1

First, the following user-defined CT specifications and segmentation parameters are read into the code via GUI (fig. 3): the number of scan slices, the number of pixels per column and per row, and the upper and lower voxel intensity limits for both cortical and cancellous bone. A counter begins to record the total processing time at the end of each step, and a wait bar is generated in order to monitor progress.

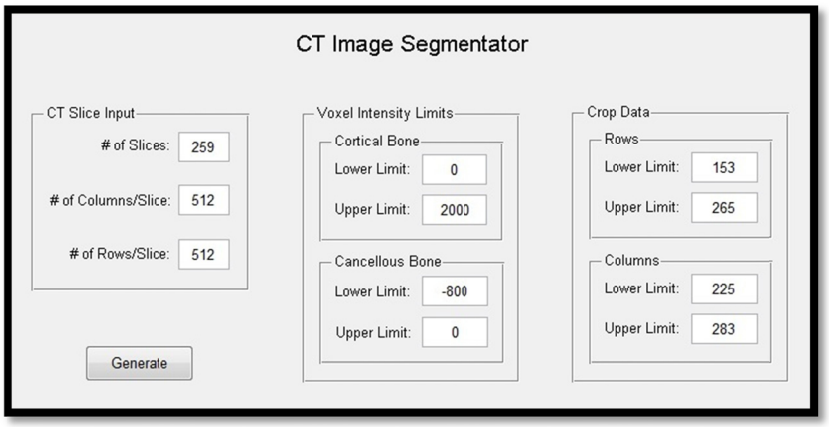

Fig. 3 GUI showing input parameters used for trial run

A 3-D array is then pre-allocated with zeros with dimensions equal to the voxel dimensions of the CT scan. Each slice of the CT scan is then imported as the intensity of each voxel is recorded into the 3-D array. Two additional 3-D arrays - also having the same dimensions as the CT scan - are then pre-allocated zeros: one for representing cortical bone and the other for cancellous bone.

Steps 2 & 3

Two sequential image segmentation loops then begin by determining whether the intensity of each voxel in the CT scan falls within the range of either of the two types bone tissue, and assigns a 1 to the corresponding location in the appropriate bone tissue array.

Step 4

A following segmentation loop uses an edge-detection technique based on contrasting intensities of adjacent voxels (greater than 300 in the axial plane) and assigns a 1 to the corresponding cortical bone array and a 0 to the corresponding

cancellous bone array. This step is performed because the thin cortical walls in the proximal and distal condyles are less dense and, therefore, have lower voxel intensities. This can result in the previous segmentation loops assigning a 1 to the corresponding cancellous bone array rather than the cortical bone array. This step partially resolves this problem, and additional corrective measurements are performed in steps 6 and 8.

Step 5

Small cortical bone "islands" within the cancellous bone region will potentially form during the previous segmentation loops due to noise in the CT scan and the frequent similarity in voxel intensity between cortical and cancellous bone. Therefore, another loop is performed where these islands are removed. For each element in the cortical bone array that has been assign a 1 during the segmentation loops, the program counts how many adjacent elements in the axial plane have - up to this point - been labeled as cortical bone and how many elements have been labeled as cancellous bone. If the number of adjacent cortical bone elements is less than 4 and if the number of adjacent cancellous bone elements is greater than 4, then the corresponding elements in the cancellous and cortical bone arrays are assigned a 1 and a 0, respectively. The entire step is repeated three times.

Step 6

To further enhance the integrity of the cortical bone point cloud in the upper and lower condyles – where the cortical wall is thin and where cancellous bone is adjacently located – the present step was developed in order to convert all cancellous

bone elements that are adjacent to elements currently segmented as cortical bone elements, into cortical bone elements. This method is anatomically valid because the material property change along the cortical/cancellous bone interface is characterized as more of a gradient than a discontinuous change.

For each element in the cancellous bone array with a value of 1, the program examines each adjacent element in the corresponding location in the cortical bone array; if at least one of the elements has a value of 1, a 0 is assign to the element in the cancellous bone array and a 1 to the cortical bone array.

Step 7

Some areas within the cancellous bone region have such a low density due to its porosity that the cancellous bone array may have holes - or regions of 0's within regions on 1's. The lower voxel intensity limit for cancellous bone could be reduced in order to solve this issue; however, the solution would lead to additional problems as many cancellous “islands" would form in the empty space of the scan due to noise.

The present solution solves the problem using a similar counting method described in step 5. For each voxel location that has not yet been defined as cortical or cancellous bone in the appropriate arrays, the program counts how many adjacent elements in the cancellous array have a value of 1. If the number is greater than three, the corresponding cancellous bone element is assigned a value of 1. The entire process is repeated five times.

Step 8

A final step in ensuring the integrity of the cortical wall is taken by converting any remaining cancellous bone elements that are exposed to the outer cortical bone surface into cortical bone elements. For each element in the cancellous bone array with a value of 1, the program counts how many adjacent elements are segmented as cortical bone and how many are not segmented as either type of bone tissue (empty space). If at least one adjacent element is cortical bone and at least one is empty, then the corresponding element in the cortical bone array is given the value of 1, and the cancellous bone element is given a value of zero.

Step 9

Finally, data points are plotted in 3-D showing the spatial locations of cortical bone voxels and cancellous bone voxels (fig. 4 and Fig. 5). Further development of the code will include being able to export the point cloud data into a usable format for CAD manipulation. The code syntax for this technique is found in Appendix B.

Accuracy

Reliability and accuracy of the fully-automated segmentation approach depends solely on user-input: *i.e.* the voxel intensity threshold values representing each segmented material. Care should be taken to insure that the defined thresholds accurately represent the corresponding bone material.

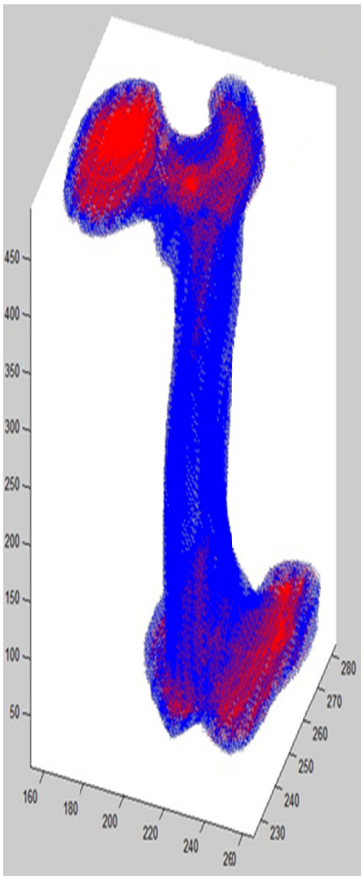

Fig. 4. Point cloud model showing cortical bone (blue) and cancellous bone

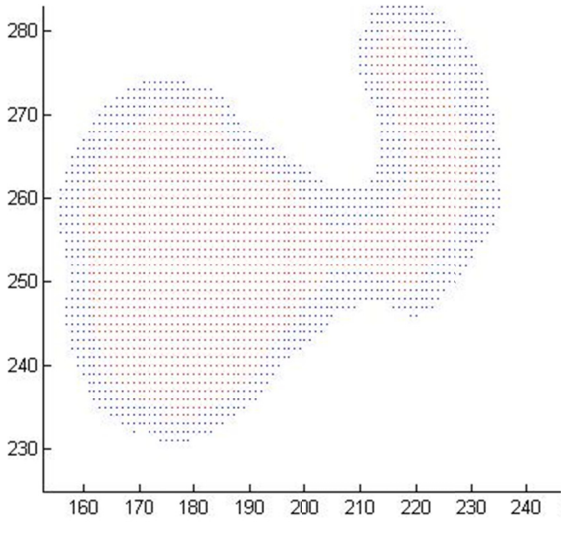

(red)

Fig. 5. Axial slice (left: hip joint, right: greater trochanter) of point cloud model showing cortical bone (blue) and cancellous bone (red)

3. Specimen CAD Models

Once image segmentation for each femur specimen is complete, the resulting bone tissue geometry data is used to generate a 3D CAD model characterized by a closed triangular-meshed surface. An intact femur is used as a demonstrative example. An initial surface model comprising of approximately 500,000 faces (fig. 6) was generated directly from the segmentation data using a surface generation module in Amira. The triangles comprising the meshed surface were very small. In addition, significant aliasing occurred on the curved surface.

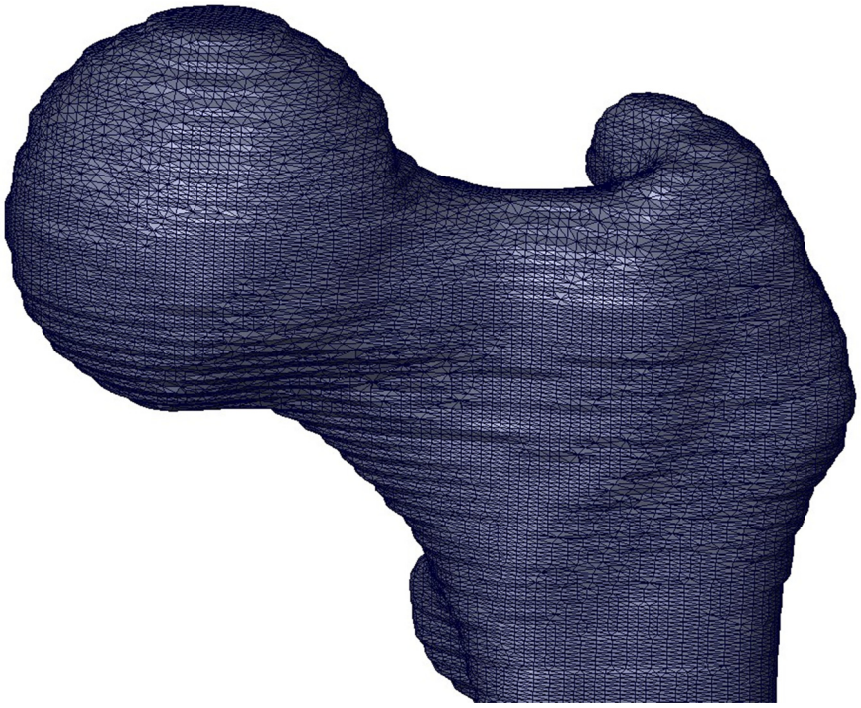

Fig. 6. Proximal view of a femur surface model following the initial surface generation

A surface smoothing module built into Amira was then used to reduce surface aliasing. The module iteratively makes small adjustments in the coordinates of each vertex by shifting them towards the average position of adjacent vertices. For this first

phase of surface smoothing, 600 iterations were performed using a lambda coefficient of 0.1 (fig. 7). The parameter values chosen were based on trial by error to determine the best combination.

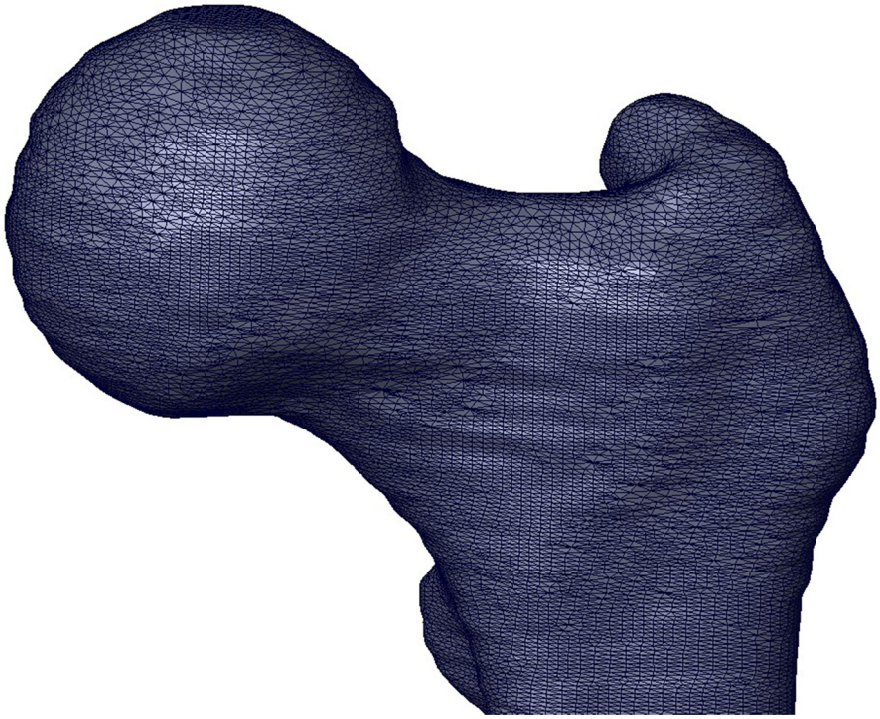

Fig. 7. Proximal view of a femur surface model following the first smoothing phase

In order to be effective, further smoothing requires that the size of the triangular faces is increased. Increasing the face size is also important when the models will be used for intensive processing – such as in the surface averaging technique and numerical simulation. Reducing the number of vertices decreases the total processing time as well the required memory. However, surface quality of the mesh must also be maintained by ensuring that the edge lengths of each triangle are approximately the same length.

Therefore, an iterative technique involving surface simplification and smoothing was developed. For each iteration, the number of faces was first reduced by 10,000 while satisfying upper and lower limit constraints regarding edge length. The upper and lower limit constraints were initially defined as 1.2 mm and 0.8 mm, respectively. An option for preserving the slice structure of the model was enabled in order to ensure that the final model geometry accurately represented the CT scan data. Each iteration concluded with subtle smoothing of the simplified surface using only one smoothing pass.

Eventually, the initial constraints prevent further simplification as defined by the desired number of faces to reduce by. When this occurred, both constraints were increased by 0.1 mm, and the simplification and smoothing passes continued. The process was repeated until the upper limit reached 4.0 mm. Then, the process still continued, but the number of faces was reduced by only 1,000, and only the lower limit was increased until it reached 3.9 mm. One final iteration was then performed with the lower limit set to 1.95 mm – giving the triangular-meshed surface models edge lengths within the range of 1.95 to 2.00 mm.

When the surface generation, simplification, and smoothing process was complete (fig. 8), the data was saved in stereolithography (STL) format. For the present application, a quality STL model has triangular edges of approximately the same length, no holes in its surface, and small angle differences between adjacent surface triangles. These stipulations are necessary for quality 3D meshing with tetrahedral elements – the

element type most suitable for complicated geometry but also very susceptible to poor mesh generation.

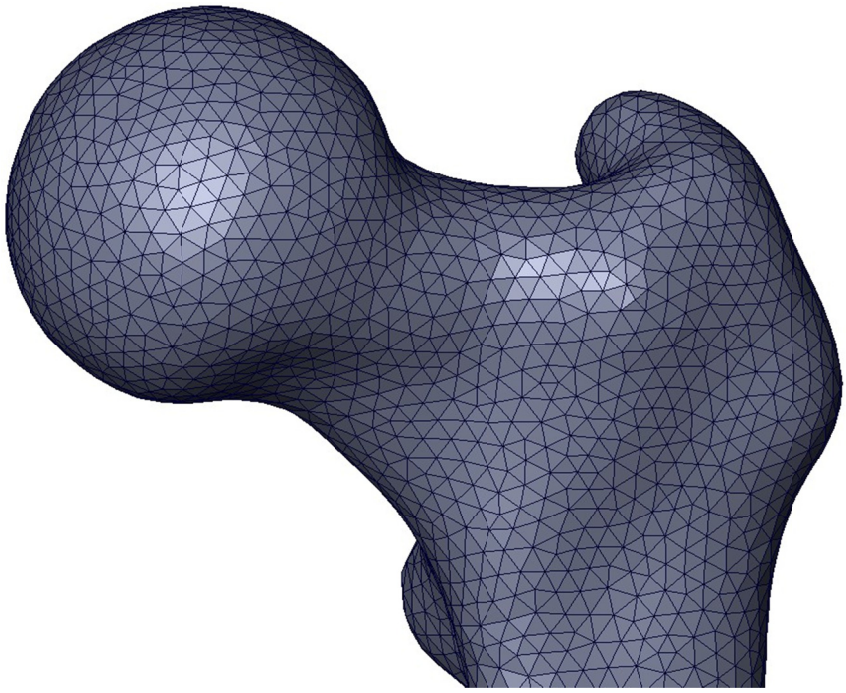

Fig. 8. Proximal view of a femur surface model following the simplification and smoothing process

4. Geometry Measurements

Relatively new CAD methods – available in commercial programs like Mimics, Polworks Rapidform, and Amira – can easily quantify surface areas, cross-sectional shapes and sizes, bone curvatures and angles, and surface topographic variation, in addition to more standard linear dimensions. The benefit of utilizing medical application-based CAD programs allows the user to superimpose CT slices on the corresponding 3-D model, which can aid in acquiring measurements from the specimen sample. Even standard CAD programs such as SolidWorks (Dassault Systèmes, 2011),

Pro/Engineer (PTC, 2011), and Unigraphics NX (Siemens, 2011) are capable of dimensional inquiry of specimen models.

5. Statistical Analysis

Geometry measurement derived from specimen samples can then be used to quantify normal human morphology and variation, as well as test hypotheses about the type and extent of variation with respect to body size, age, sex, race, or other parameters via analysis of variance (ANOVA). Using standard statistical analysis techniques, researchers and design engineers can determine how much variation affects the region of interest and which factors are associated (*e.g*. sex, age, etc.).

6. Specimen Mean Form Models

Based on techniques developed for the automotive industry, mean form models are generated from the specimen sample population and sub-populations. Originally, the mean form method was intended for quantifying small dimensional variances in manufactured parts from assembly lines; however, the technique was adopted in the present study to take into account large variances in human skeletal geometry and generate "average" models.

Specimen CAD models are first imported into Polyworks (InnovMetric, 2011), a universal 3D metrology software platform used for digitizing and reverse engineering, where “average” point cloud models representing each sample subgroup and subpopulation, as well as the total population, are derived. This process required that each specimen model be scaled to equal length based on the average – a necessary step

in order to minimize the resulting distortion, particularly in the proximal and distal ends, while still capturing shape variation (the trade-off being that size variation is not considered). Following model scaling, specimens in each sample subgroup are manually aligned using an “n-point” method: specimen models are aligned based on selecting prominent features, and the corresponding displacement vectors were minimized. An optimization algorithm is then used to find the "best-fit" alignment by minimizing the displacement vectors between each corresponding surface node location.

Finally, the optimized surface geometry for each sample subgroup is generated by calculating the average location of each corresponding node. The process of alignment and averaging can be repeated for each sample subpopulation and also for the total population using the subgroup average models as input.

7. Implant Contour Optimization

In the majority of cases where patient-specific implant manufacturing is not economically practical and, therefore, mass production must be adopted, contour optimization regarding implant/patient fit is accomplished using the specimen mean form models as design "templates." The logic behind this technique is that if the implant is designed to match the shape of the specimen mean form model of interest, then the likelihood that the shape will be sufficient for the entire population is maximized. Subsequent simulation and experimental testing may conclude that additional shapes are required in order to accommodate large skeletal geometry variations within the population. Implant sizes, on the other hand, can be determined

from statistical analysis, which is currently a standard practice in implant design. A significant benefit of this new method for fit optimization is that it utilizes a non-iterative approach to develop the optimal implant contour(s).

8. Simulation-Based Performance Analysis

The performance of existing implant designs, as well as conceptual designs, is then quantified and compared using finite element methods. Simulating post-operative physiological loading conditions using specimen models (fractured or healed) fixated with the devices of interest allows design engineers to predict structural behavior. Additionally, "virtual surgery" techniques simulating the implant insertion process provide similarly useful information. The reliability of the simulated results is dependent of four factors: realistic material properties, accurate loading/boundary conditions, mesh quality, and mesh independence.

Material Properties

Equilibrium equations and equations of motion used to solve nodal displacement during the simulations require material property constants as input. For anisotropic materials, such as biologically inert metals and composites, only the modulus of elasticity and Poisson's ratio is required to be explicitly defined for static analysis. For dynamic analysis, the material density must also be defined.

Bone is considered to behave in an anisotropic manner with material properties dependent on direction. However, research has demonstrated that when modeling long bones such as the femur, transversely isotropic properties of cortical bone and effective

isotropic properties of cancellous bone can be assumed [74,75]. The material properties applied to the following two case studies are listed below in Table 1.

Table 1. Material properties for femur and implant materials

	Modulus of Elasticity (GPa)	Poisson's Ratio	Shear Modulus (GPa)
Cortical Bone	*E1* = 20, *E2* = *E3* = 18.2	*v12* = *v13* = 0.22, *v23* = 0.38	*G12* = *G13* = 5.6, *G23* = 4.5
Cancellous Bone	0.4	0.25	0.16
Ti6Al7Nb	110	0.342	41.0
316L Stainless Steel	193	0.29	74.8
CFR-PEEK	18	0.36	6.6

Loading/Boundary Conditions

In addition to realistic material properties, loading and boundary conditions representing the expected physiological conditions of the patient must also be defined. Given the complexity of the human musculo-skeletal system and the current computational capabilities, it is not feasible to simulate an individual entire system. Since only the local fracture site is of interest for implant design, the simulation system should only consist of the necessary members. This requires a thorough understanding of musculo-skeletal biomechanics and Newton's 3rd law: for every action there is an equal and opposite reaction.

Many types of physiological loading conditions, as functions of percent weight, have been quantified using accelerometers attached to the applied loading region of the local fracture system [74]. Not only is force magnitude – sometimes a function of time (*e.g.* impacts) – of interest, but also relative direction and surface area of force transfer to the local system (*e.g.* joint contact). Newton's 3rd law comes into play when defining the location of the reaction force. Particularly when dealing with static and pseudo-

static analyses, the system must have zero degrees of freedom on the macro scale. This is accomplished by constraining the nodal degrees of freedom within a defined region. For instance, when modeling the femur, if loading is applied at the hip joint, the knee joint interface on the distal condyles must be constrained. However, identical results could be attained by applying the load at the knee joint – equal in magnitude but opposite in direction – and constraining the hip joint.

Mesh Quality

Tetrahedral elements are the most versatile of all 3D element types and are ideal for meshing models with high complexity such as skeletal tissue. However, they are also the most susceptible to inaccurate results due to poor mesh quality. Therefore, to achieve rapid meshing with minimal quality-related inaccuracies, strict mesh quality controls must be met. Mesh quality standards adopted by Dassault Systémes, the makers of Abaqus finite element software, were applied to the present study. These tetrahedral element failure criteria include:

1. Minimum shape factor (*i.e.* ratio of the element's volume to the spherical volume circumscribing the element) < 0.0001
2. Minimum face corner angle < 5°
3. Maximum face corner angle > 170°
4. Maximum aspect ratio (*i.e.* ratio between largest edge length and smallest edge length) > 10

Mesh Independence

Because of the linear relationship in the displacement between each adjacent node within the system, the strain – calculated by taking the derivative of the displacement function – becomes constant throughout each element. Therefore, the stress is also constant due to Hooke's law. Mesh independence can be obtained through adaptive meshing: either by decreasing the element size (h-adaptivity) or by increasing the order of each element's interpolation function (p-adaptivity). Adaptive meshing can be done manually or automatically by performing multiple simulations while successively decreasing element size or increasing element order until the response converges within an acceptable percent difference.

9. Structural Optimization

Parametric Analysis

The Taguchi method for design of experiments was adopted in order to quantify how various implant design parameters, such as dimensions, materials, fixation techniques, etc., affect the mechanical performance of the implant. The method uses an orthogonal array of experiments – or, in the present case, simulations – to statistically represent all possible combinations of design parameter values. As applied to orthopaedic implant design, the Taguchi design of experiments is performed in three steps: response analysis, analysis of variance, and superposition model for optimum response.

1. Response Analysis

The responses obtained from different simulated design scenarios can be analyzed using response tables and graphical representation of the mean effects of each parameter on design performance. The response analysis helps in identifying those design parameters that have the greatest impact on performance. In determining this, the signal-to-noise (S/N) ratio analysis is implemented. It uses the transformation method to convert the measured response into an S/N ratio by

$$S/N = -10\log(MSD), \tag{XV}$$

where *MSD* is the mean square deviation. The mean square deviation can be calculated using

$$MSD = \frac{1}{n}\sum_{i=1}^{n}\frac{1}{{y_i}^2}, \tag{XVI}$$

where y_i is the measured response and n is the number of simulations/experiments. Proposed by Taguchi, S/N ratios are performance measures that optimize a design. The optimum design given the specified parameters is achieved when the S/N ratio is maximized.

2. Analysis of Variance

The analysis of variance (ANOVA) technique predicts the relative significance of the design parameters. It gives the percentage of contribution of each factor, thus, providing a quantitative measure of various factors on design performance.

3. Superposition Model for Optimum Response

A superposition model for optimum response approximates the relationship between the performance measures and its factor levels. The total effect of each design factors is equal to the sum of the individual factor effects, and interactions among the design factors are considered errors in this model [84]. In the superposition model, optimum performance can be predicted by using the optimum conditions of the controlled parameters using the equation

$$\eta_{opt} = m + a_i + b_j + c_k + \cdots + e \,, \tag{XVII}$$

where *m* is the overall mean of the simulation responses,

$$a_i = A_{opt} - m, \quad b_j = B_{opt} - m, \quad c_k = C_{opt} - m, \ldots \tag{XVIII}$$

and *e* is the error in the repeatability of η_{opt}. $X_{opt.}$ in Eq. (XVIII) denotes the optimal condition for parameter *X*.

FEM-Integrated Optimization

While Taguchi's superposition model for optimum response can be used to determine the design parameter values that give the best overall performance and even predict the response, it does not consider objective functions such as mass minimization. Mass minimization is important in orthopaedic implant design as increased weight and size have adverse effects on surrounding tissue [85].

For design parameters associated with geometric dimensions and material properties, a finite element-based structural optimization technique should be implemented. For these dimensional parameters, the Taguchi method is best applicable

for determining which parameters should be optimized for mass minimization – those that have the greatest effect on performance as determined by ANOVA.

However, constraints associated with material yielding must be considered during structural optimization. Implant dimensions cannot be so small as to give rise to stresses that result in mechanical failure under normal and extreme physiological loading conditions.

The general workflow of simulation-based structural optimization is depicted in fig. 9. Several current computer-aided engineering software packages, such as SolidWorks, Pro/Mechanica, and NX, have the ability to integrate optimization techniques with structural analysis. The built-in algorithms iteratively update user-specified CAD model parameters until the objective function is met and constraints are satisfied. With each optimization pass, the structural analysis is performed followed by a design sensitivity analysis that determines the correlation between each design parameter and the objective function. After calculating the improved parameter values and updating the CAD model parameters, the optimization process is reiterated until convergence is achieved (usually 2%).

Typically, sequential quadratic programming (SQP) is the optimization algorithm implemented for this type of design study. With SQP, a global minimum is guaranteed if the initial conditions of the system meet the specified design constraints. Therefore, the initial concept should be overdesigned and checked via static analysis prior to optimization. Once optimization is achieved, the new design should be analyzed using

the techniques described in the “simulation-based comparative performance analysis” section.

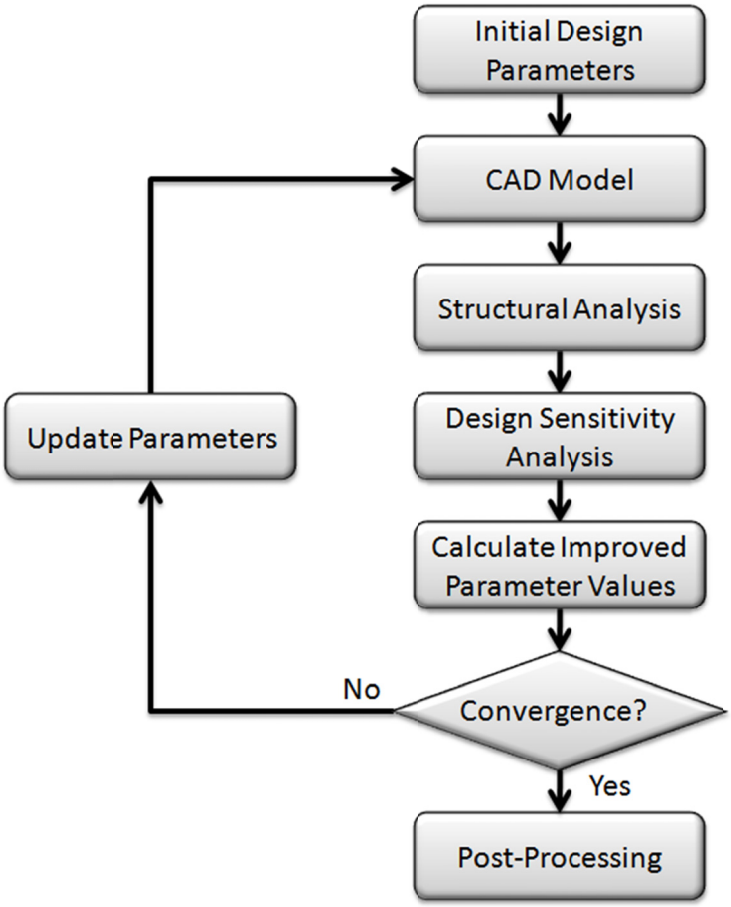

Fig. 9. Structural optimization flowchart

10. Experimental Verification

Experimental testing is a necessary validation technique for implant design. However, costs and equipment limitations make extensive testing as part of the design and optimization process infeasible in many cases. By verifying simulation results with those found experimentally for simple load cases, complex loading conditions applied to the simulation model are also verified. Loading conditions that are impractical or

impossible to experimentally reproduce – as well as internal stress/strain measurements – can be efficiently and reliably achieved using finite element methods.

In vitro testing using cadaveric specimen is difficult to reproduce due to the significant geometry variation associated with the human population. Using Sawbones fourth-generation artificial composite bones alleviates this problem by providing a test specimen control. Numerous independent studies have validated the use of Sawbones composite bones as an acceptable alternative to cadaveric specimen [76-82].

For the following case studies, a femur fixation device was developed in order to apply *in vitro* compression loads to femur specimen for the purpose of validating finite element-based simulations (fig. 10-Fig. 12). The fixture was designed to fit an MTS Universal Testing Machine. The distal fixture allowed for two degrees of freedom (translation) in the axial plane; however, it could be locked in place removing all degrees of freedom. The axial plane degrees of freedom allowed for proper alignment between the hip and knee joints in both the sagittal and coronal planes as well as freedom for femoral bending due to axial loading. Proximal fixation devices were developed in order to provide two degrees of freedom (rotation about axes normal to the sagittal and coronal planes) for both the hip joint and the proximal end of an intramedullary nail being inserted into the femur specimen.

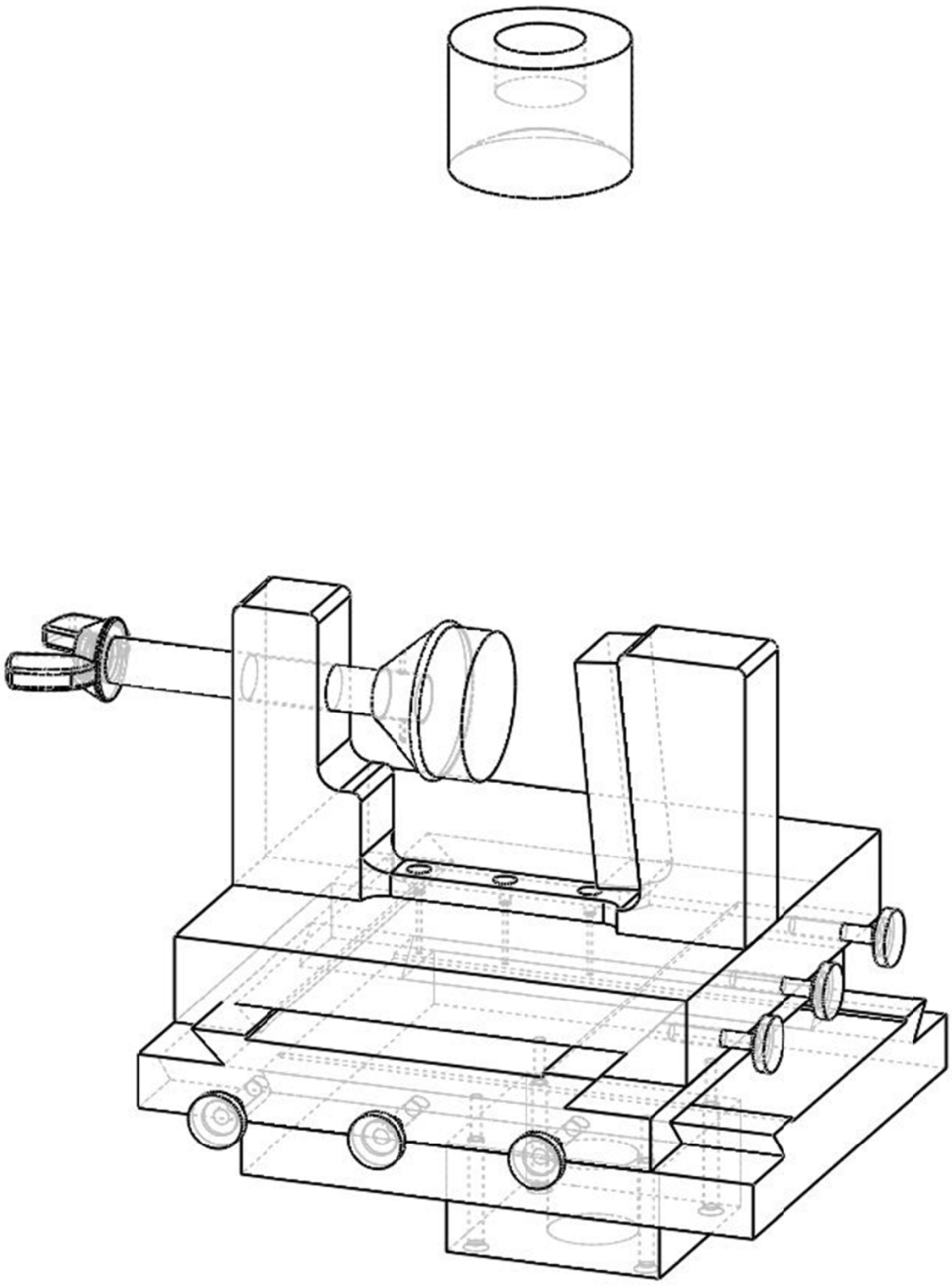

Fig. 10. Wireframe CAD model of the femur fixture assembly

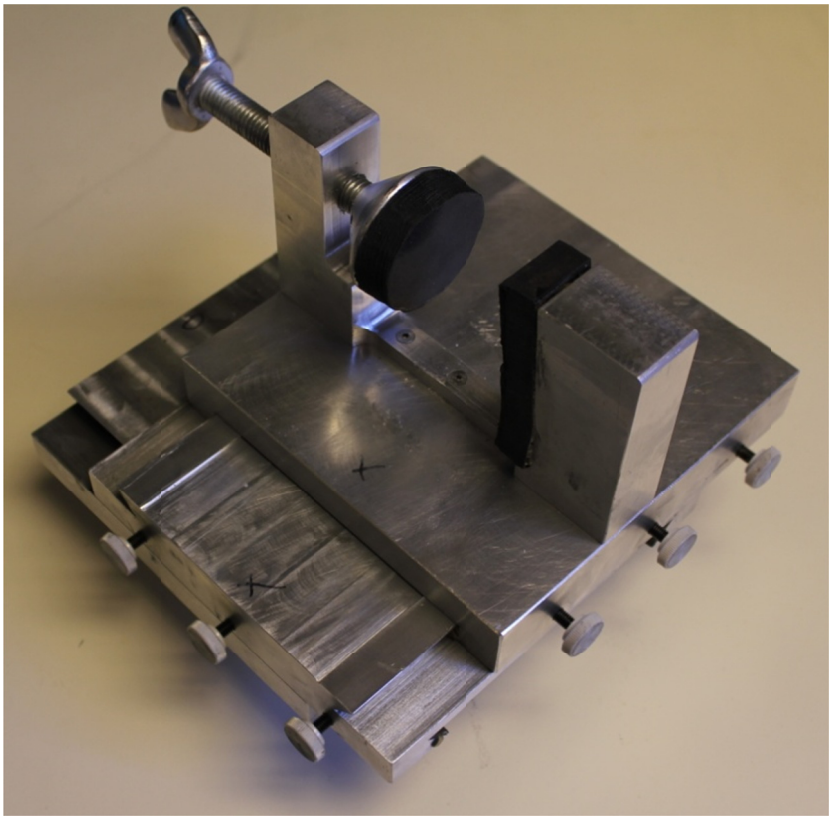

Fig. 11. Distal femur fixture for MTS universal testing machine

Fig. 12. Proximal femur fixture for MTS universal testing machine (*Left*: hip joint fixture, *Right*: IM nail fixture)

CHAPTER IV. CASE STUDIES

Femoral Intramedullary Nail

Fractures of long bones, particularly the femur, can be debilitating for patients, adversely affecting quality of life and potentially leading to long term complications. Intramedullary (IM) nailing involves creating an opening in one end of a long bone and inserting a rod through the medullary cavity of the bone. This technique allows earlier return to weight bearing on the injured extremity and shorter recovery times than other methods. It not only stabilizes the fracture, but decreases risk of infection since no incisions are made near the fracture site. It has revolutionized the ability to care for patients with fracture of the femoral shaft [86].

However, this procedure also has significant shortcomings that lead to adverse consequences for patients because current nail designs do not match the curvature of the medullary canal, particularly for the femur [87-92]. The femur is curved, and this curvature varies among individuals, but current nail designs are much straighter than human femora [87,89,92,93]. This results in problems inserting nails, including distal perforation of the anterior femoral cortical bone by the tip of the nail [87,88,92,94], iatrogenic fractures [93,95], angular defects causing inadequate contact between fracture ends resulting in union problems [89,95], and the nail rubbing against the canal wall [87,89,92,93] sometimes leading to fracture of the proximal femur [93]. Extraction of dysfunctional nails may eventually become difficult or even impossible due to friction

[87,89,92,93]. Furthermore, mismatch between nail and femur geometries can significantly affect the biomechanics of the proximal femur [87, 93].

A strong clinical need exists for an IM nail that is geometrically optimized for anatomical fit. Several studies have examined the curvature radius of the human femur as well as the correlates of curvature [87-90,92,96-101]. According to these studies, radius of curvature varies between 109 cm and 158 cm [89,90], but it is not correlated with femoral width, length, or age [87]. The predominant factors affecting femur curvature were determined to be race and sex [87,97-101]. In each study, the radius of curvature was calculated using a three-point arc fit with the assumption that the curvature is constant throughout the length of the femur. However, close examination of the femur reveals that its curvature is not constant. Thus, it may not be sufficient to assume a constant radius of curvature for intramedullary nail design.

Although it is generally recognized that medullary canals are curved and that individuals vary in femoral size and shape, femoral geometry variation has never been quantified, leading to instrumentation that fits poorly in the majority of individuals. The design and optimization method discussed in the previous chapter was therefore implemented in order to overcome these limitations in knowledge and improve IM nail design. The technique was used to optimize IM nail geometry with respect to patient fit while taking into consideration the large variation in femoral curvature. A successful match between nail and femur geometry will allow development of new instrumentation that will avoid generation of stresses that could lead to other fractures, or altered femoral biomechanics that can impede the healing process.

Methods & Materials

1. Femur Specimens

Forty intact femora were selected from the Hamann Todd Osteological Collection housed at the Cleveland Museum of Natural History (fig. 13). This is a cadaver sample of urban populations from Cleveland from the early 20th century and consists of 3,000 skeletons of known sex, race, age, and health history. The relatively small sample size was chosen to conduct a pilot study to determine the approach's feasibility with the intent of later expanding the study with a larger sample size to better represent the American population as well as populations of other nationalities.

All included specimens were from individuals with no developmental or skeletal pathologies. The sample was chosen to represent a range of age, sex, and race variation in femoral geometry. Due to both the collection's specimen availability and the predominant races/ages representing the American population, the selected sample was racially differentiated into Caucasians and African Americans differentiated in into age groups in the ranges of 30-40 years and 70-80 years. Within the age groups, individual ages were roughly evenly distributed.

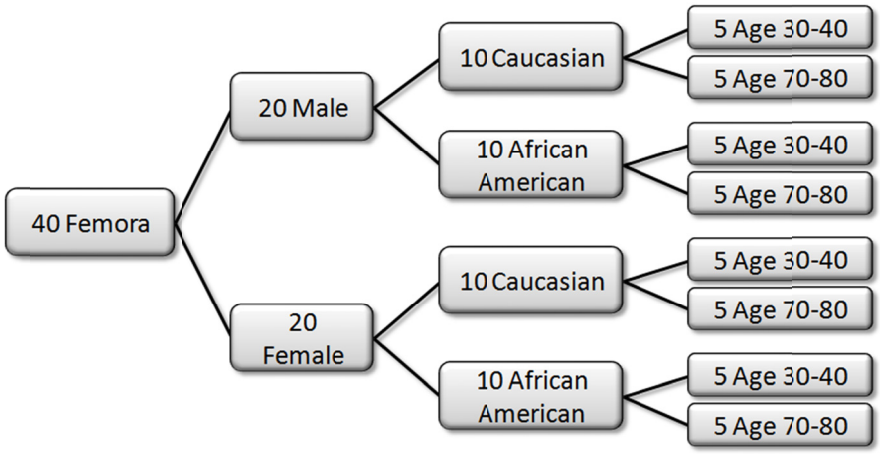

Fig. 13. Femur sample population

2. Medical Imaging & 3. Specimen CAD Models

Femora were scanned on a Philips AcQSimCT scanner at Case Western University Hospital in Cleveland with 1 mm resolution and 2 mm slice thickness. The scan data were saved in DICOM format - the industry standard for viewing and distributing medical images - and imported into Amira software (Visage Imaging).

Two stereolithography (STL) models were generated for each femur (see *Methodology*): one representing the exterior geometry of the intact femur only (fig. 14), and the other representing the exterior plus internal surfaces of the diaphysis (fig. 15). Internal geometries of cortical bone within the proximal and distal ends of the femur were not included because of the complications of surface-averaging given the thin cortical shell, and because the internal geometry of these regions are not crucial for characterizing femoral geometry for the purpose of femoral IM nail design. However, internal medullary canal geometry within the diaphysis is of great significance; for the

diaphyseal models, the diaphysis was selected between the distal margin of the lesser trochanter and immediately proximal to the patellar surface (fig. 16).

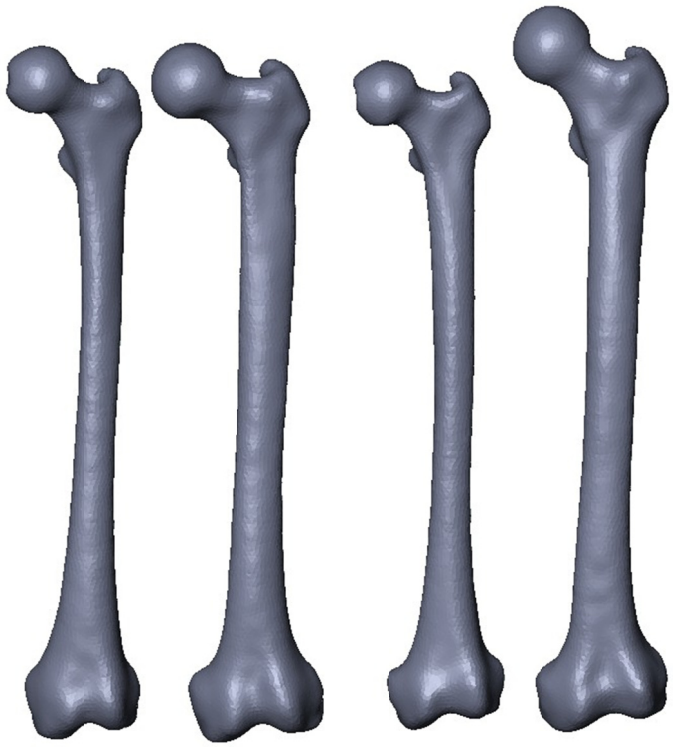

Fig. 14. Exterior surface STL models (4 of 5 in subgroup: Caucasian, female, age 70-80)

Fig. 15. Exterior/interior surface STL model of femoral shaft

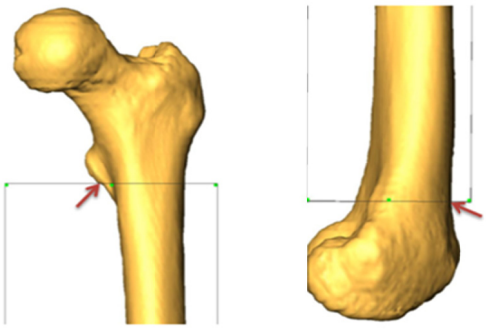

Fig. 16. Cropping locations for creating diaphyseal model

To demonstrate the effect of an optimized nail design, the femur having the highest curvature was chosen for the finite element study (see part 8, *Simulation Performance Analysis*). This required that both cortical and cancellous bone geometries be segmented separately. For this specimen, the bone was first segmented using the automated technique. Manual segmentation followed to ensure that no holes were present between cortical and cancellous bone tissue as well as within the material's volume (fig. 17) (*Note*: the fully-automated segmentation code discussed in the previous chapter was developed after the surface generation phase of this case study was carried out). The medullary canal void was ignored for both cortical and cancellous bone because the canal was to be later reamed to a larger diameter during "virtual surgery", simulating the actual clinical procedure. The reamed canal was later cut into the canal-less femur using CAD Boolean operations given the actual canal geometry derived from the CT scan and the desired reamed diameter.

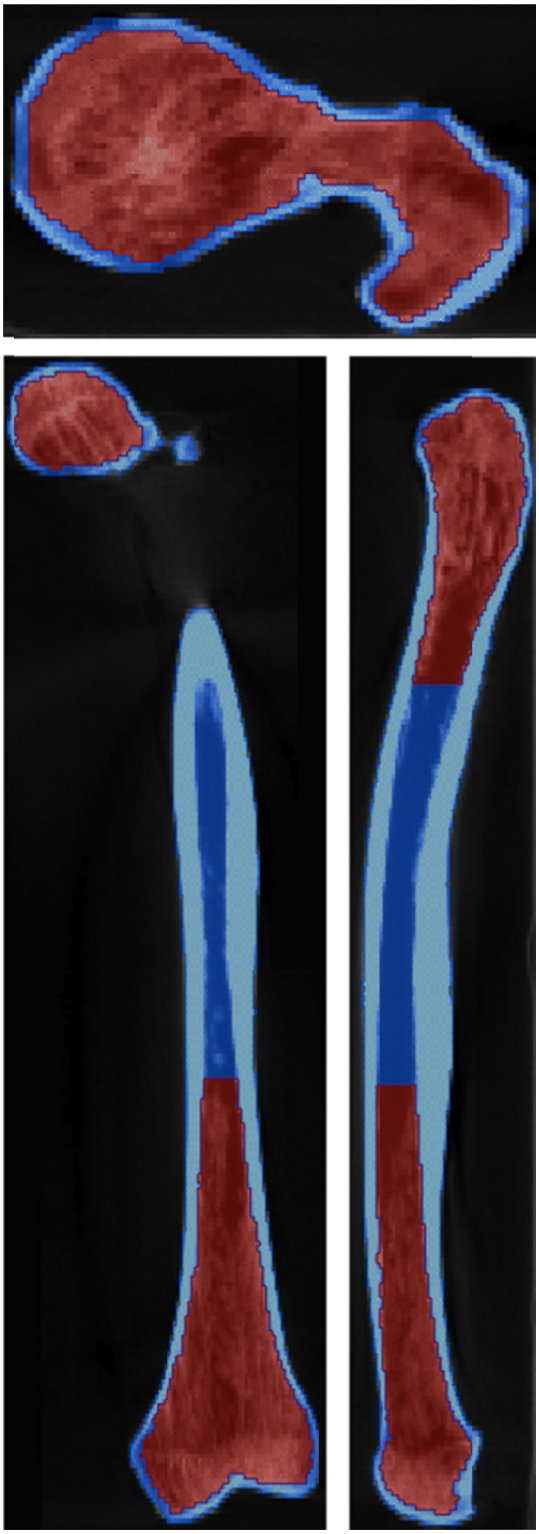

Fig. 17. Axial (top), coronal (left) and sagittal (right) CT slices showing segmentation boundaries for cortical (blue) and cancellous (red) bone (ignoring medullary canal)

4. Femoral Geometry Measurements

The CT scans and STL models were used in combination to measure geometric features of each specimen. An oblique sagittal CT slice coplanar with the medullary canal centerline was generated from each CT scan and orientated with respect to the corresponding diaphyseal STL model (fig. 18). These were used to measure total bone length, diaphyseal length, periosteal and medullary diameters at mid-shaft, cortical wall thickness, and the location of the most anterior point of the anterior surface as a function of percent length from the proximal end. Additionally, radius of curvature of the medullary canal's centerline was calculated using three equidistant points on the centerline within the diaphyseal length. The ratio of the shaft length to the outer diameter at mid-shaft was also calculated. These measurements were selected because of their potential contribution towards IM nail design: by aiding in determining the range of sizes/shapes required to accommodate the sample's variation.

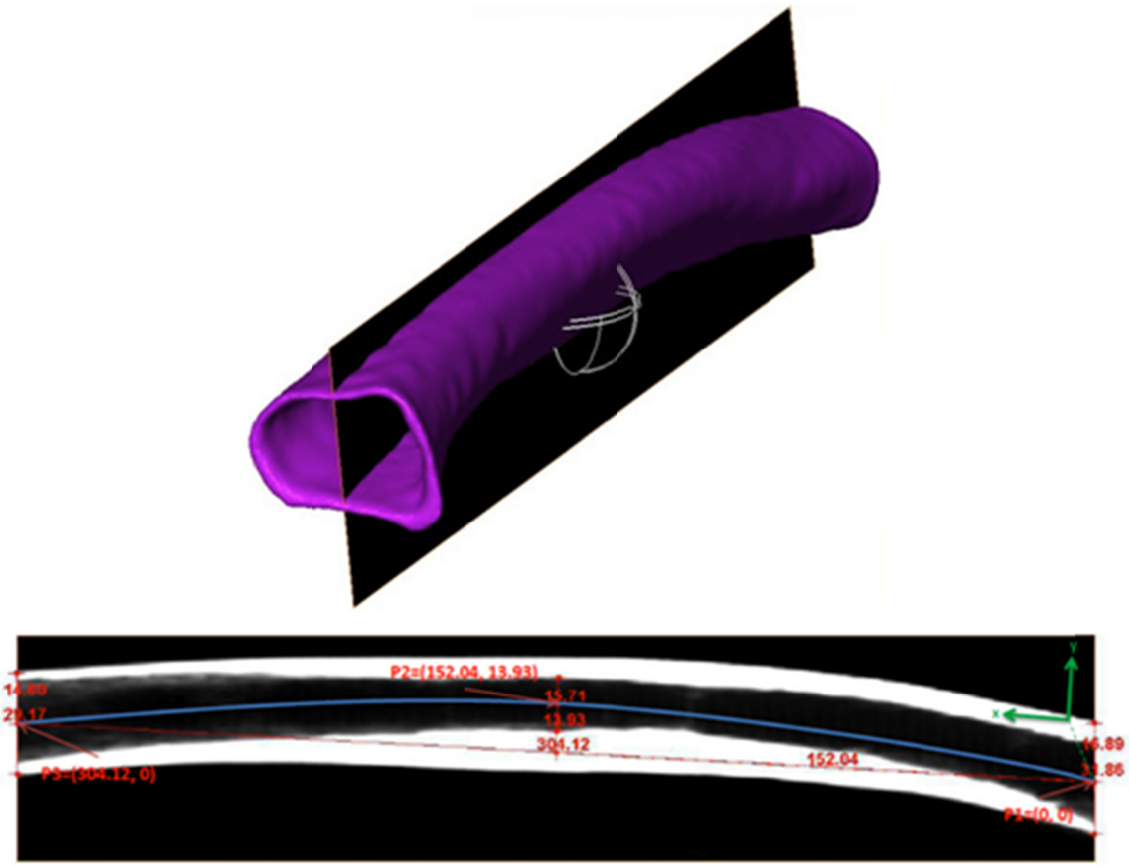

Fig. 18. Geometric measurement method showing generated oblique slice through the diaphysis (above), and measurement of curvature (below)

5. Statistical Analysis

To determine which populations varied in relevant femoral dimensions, measurement data was compared between sex, age, and race groups, as well as within individual subgroups (e.g. female + African American + 30-40 years of age) using analysis of variance (ANOVA).

6. Specimen Mean Form Models

N-point and best-fit alignment techniques were performed for each subgroup of femur STL models as illustrated in fig. 19 and Fig. 20, respectively. Once the mean form

models were generated for each subgroup, mean form models of each sub-population and the total population were generated (fig. 21).

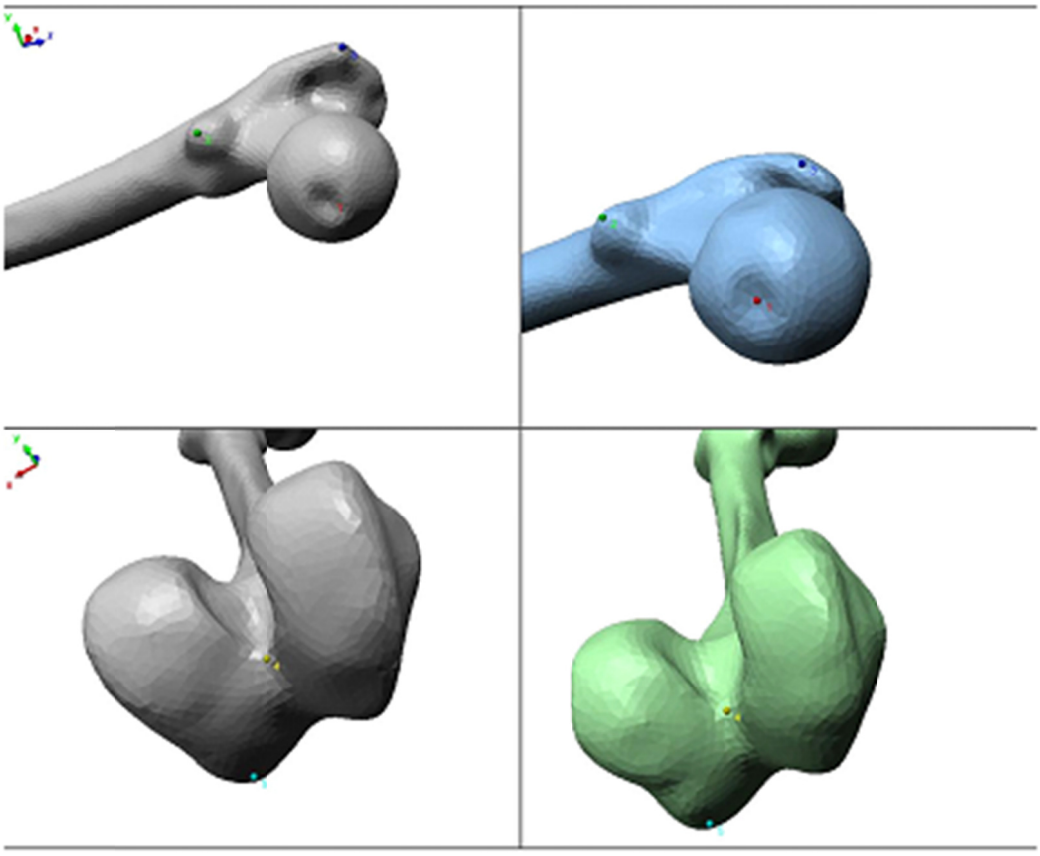

Fig. 19. N-point alignment technique showing corresponding alignment points selected for a pair of femora within a subgroup

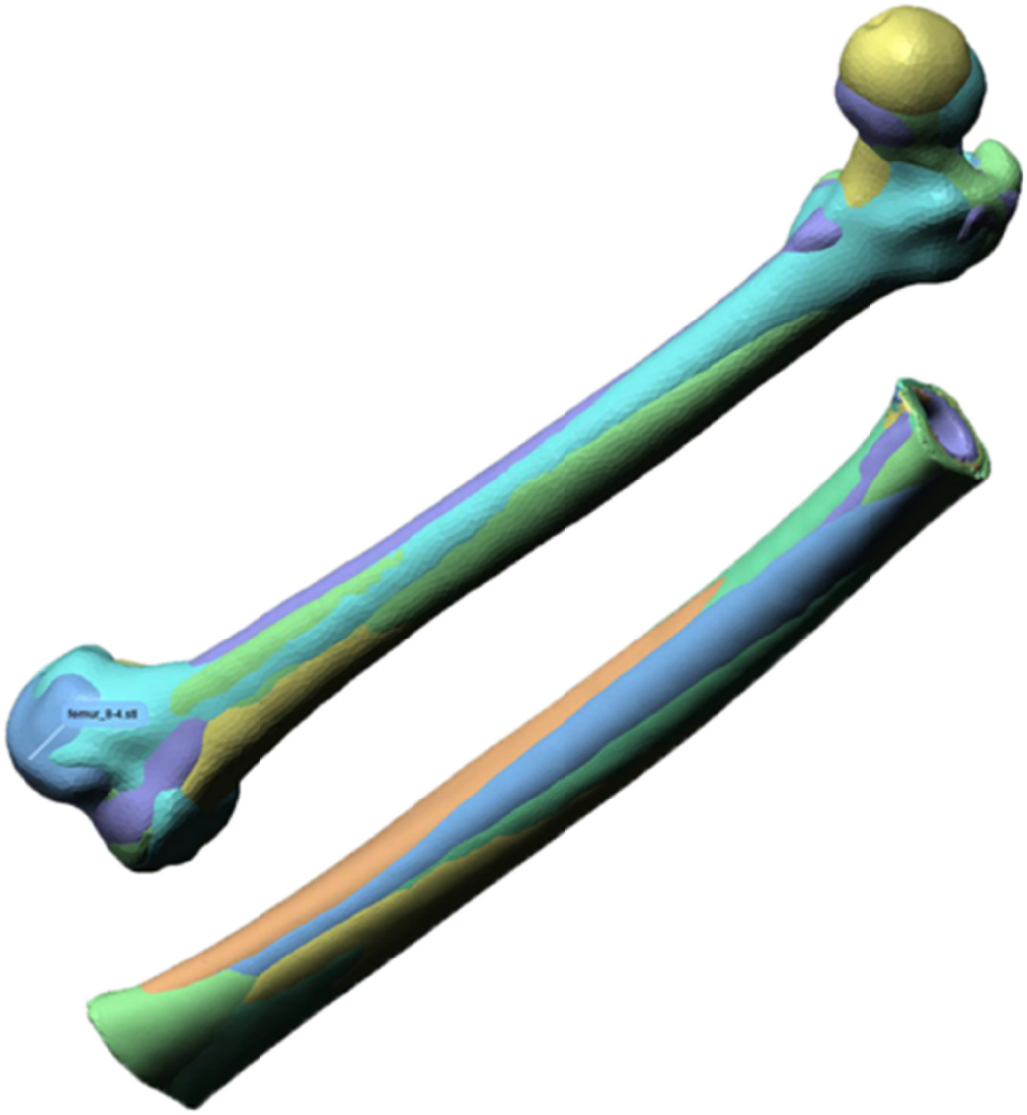

Fig. 20. Best-fit alignment technique for intact (above) and diaphyseal (below) STL models

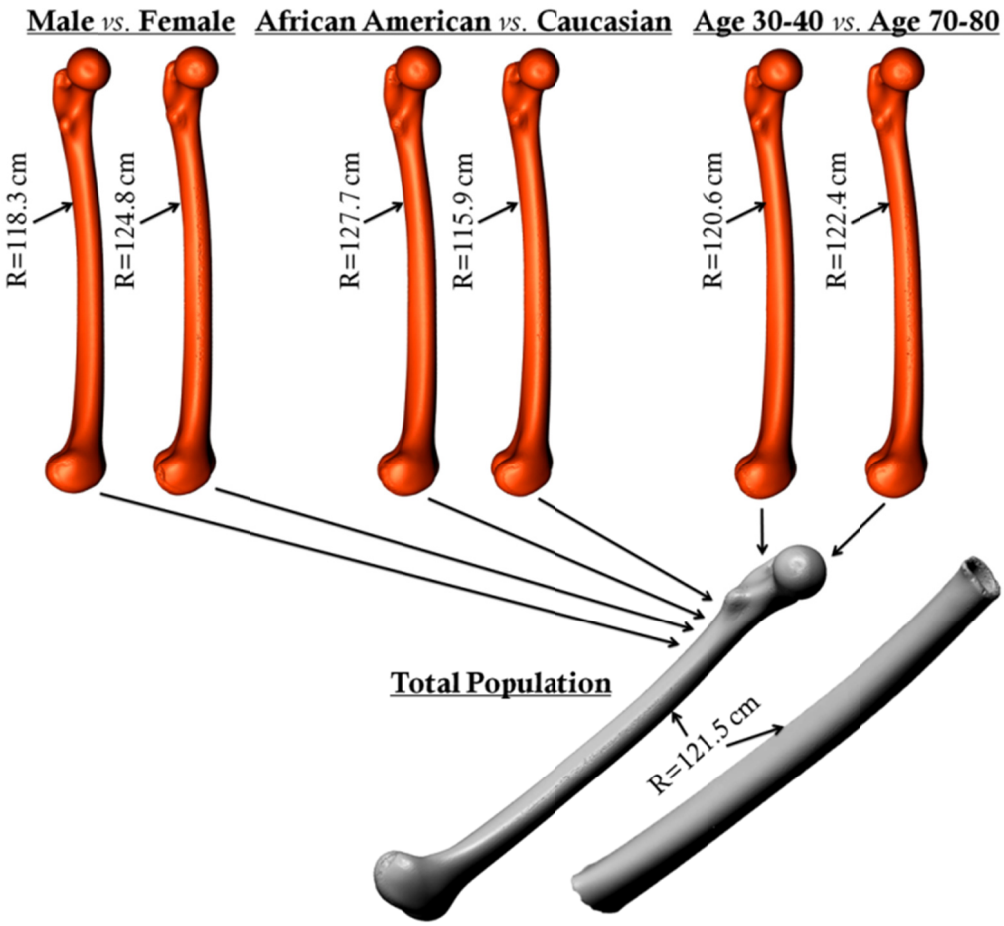

Fig. 21. Average femur models for sex, race, and age groups, and for entire population, with radius of curvature indicated for each

7. Contour Optimization

With the intent to create one curvature profile that can accommodate the entire sample population, using CAD techniques, the diaphyseal model representing the total population average was superimposed onto the total population average intact femur model. The assembly was then cut to form a cross-section coplanar with the medullary canal centerline. A spline curve was fitted along the optimum nail path starting at the proximal entry point. After establishing the coordinate system, the spline curve was

divided into 16 equidistant segments (fig. 22). The off-axis distance of each point was measured to obtain data points for the optimum nail curve (Table 2). Each off-axis distance was then divided by the total length so that the optimum curvature function can be scaled for any given nail length while retaining the same shape. Finally, the function was used to create an IM nail having the appropriate length to fit the femur model having the highest curvature in the sample (fig. 23). For comparison, two additional nails were created to represent current nails with constant radii: one with a 200 cm radius and another with 300 cm – both common for nails currently on the market [86-88].

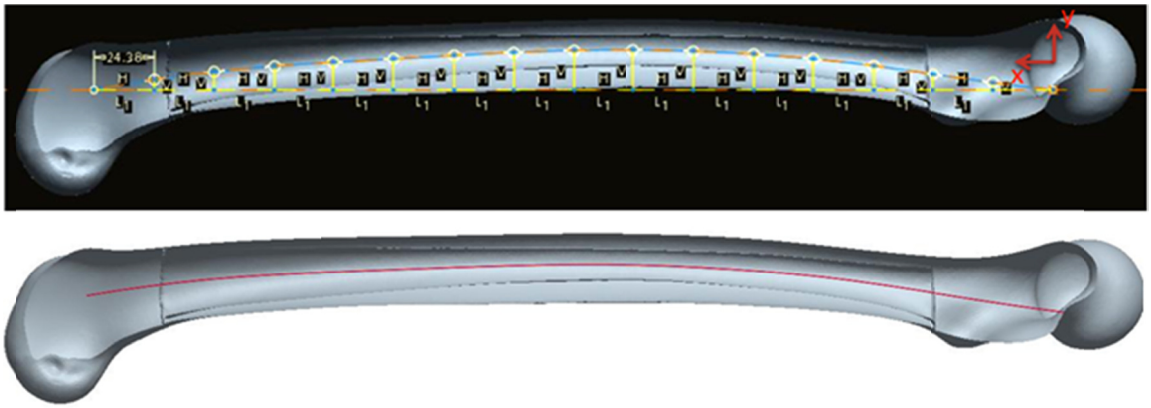

Fig. 22. Method for determining optimal nail design (see text for discussion)

Table 2. Length-standardized data points

(*l* = nail length)

X	Y
0	0.00000 *L
L/16	0.00774 *L
2*L/16	0.01669 *L
3*L/16	0.02549 *L
4*L/16	0.03233 *L
5*L/16	0.03785 *L
6*L/16	0.04090 *L
7*L/16	0.04236 *L
8*L/16	0.04174 *L
9*L/16	0.03956 *L
10*L/16	0.03651 *L
11*L/16	0.03295 *L
12*L/16	0.02928 *L
13*L/16	0.02510 *L
14*L/16	0.01915 *L
15*L/16	0.01090 *L
16*L/16	0.00000 *L

Fig. 23. Optimized intramedullary nail

8. Simulation-Based Performance Analysis

In order to assess the effectiveness of the geometrically optimized nail compared to current nails, a combination of digital solid modeling and finite element methods were used to perform virtual surgery: first by reaming the medullary canal and then simulating the insertion process of the nails into a highly curved femur.

Reaming the Medullary Canal Using CT scan measurements and the CAD assembly model of the femur having the highest curvature in the sample, a spline curve

representing the curvature of the medullary canal's centerline was created. The proximal end of the curve was extended to the nail entry point located on the greater trochanter. According to the CT scan, the average diameter of the canal was approximately 11 cm. A standard diameter available for current IM nails is 12 mm; therefore, a reamed canal diameter of 13 mm was chosen. Surgical technique requires a reamed canal to be approximately 1 mm larger than the nail diameter [102]. Over-reaming the canal by 1 mm is generally recommended to ease nail insertion, regardless of nail curvature [102,103]. A solid reamed canal cross-section was then extruded along the spline curve. The canal geometry was then superimposed onto the femur assembly model (fig. 24). Using Boolean operations, the intersecting solid volume of the reamed canal geometry and the femur model was removed from the femur model (fig. 24). The reaming path follows the medullary canal centerline throughout the diaphysis; however, the drilled and reamed path through the proximal cancellous bone region must have a path that’s tangent to the proximal medullary canal and normal to the proximal insertion hole in the greater trochanter as described in current IM nail technique guides [86]. This was taken into consideration when determining the reaming geometry.

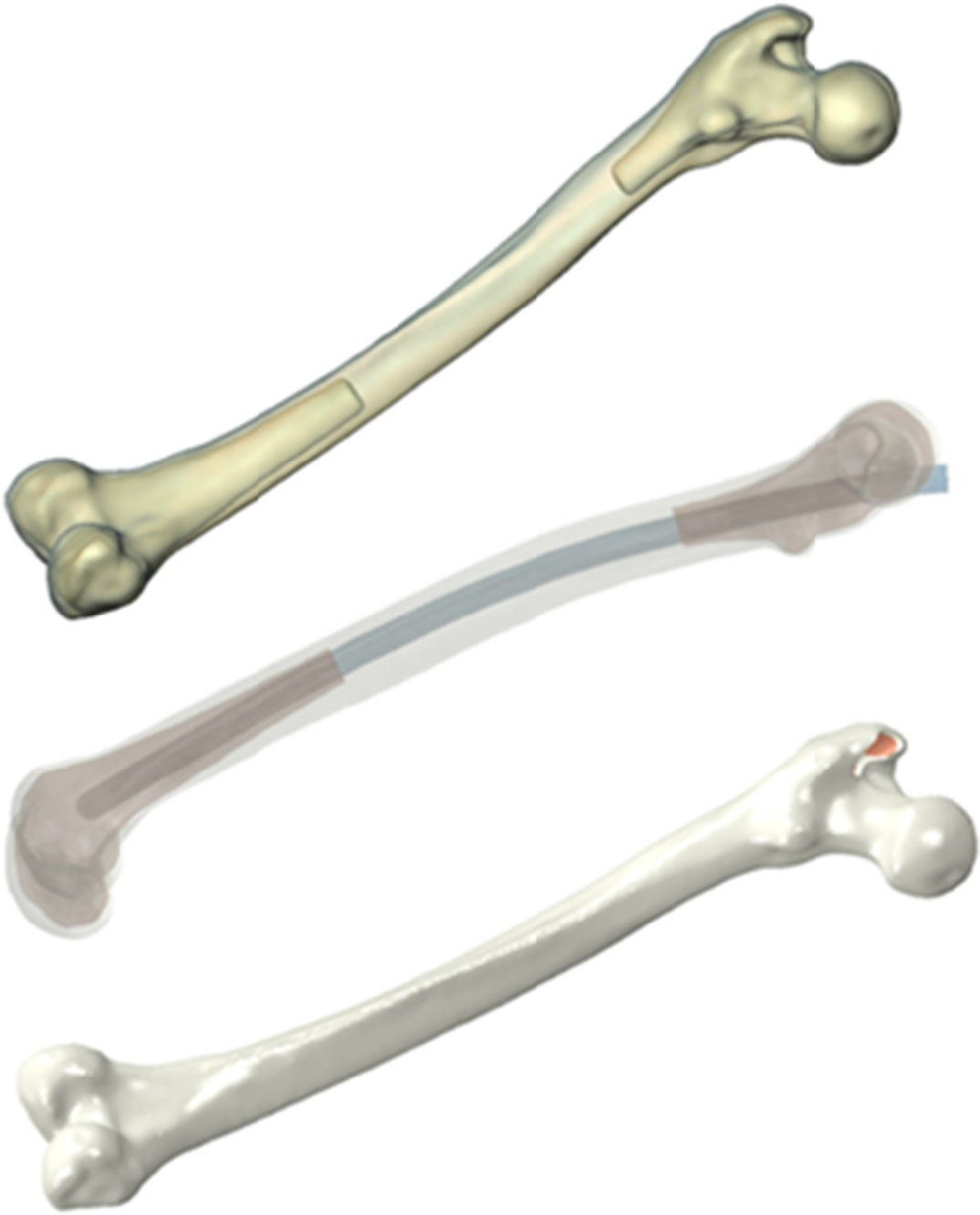

Fig. 24. Digital model of femur before reaming showing cortical and cancellous regions before reaming (top), the superimposed reaming geometry within the femur (bottom), a reamed femur (middle).

IM Nail Insertion A finite element technique based on the Abaqus/Standard (Dassault Systèmes) platform was developed in order to simulate the insertion procedure of IM nails. Because of the extraordinarily high computational costs of using dynamic FE techniques to drive a curved nail through a reamed canal with a dissimilar curvature, an approach using multiple static steps was adopted. In the present case study, only stresses induced by curvature mismatch were of interest for comparing the two IM nails.

Material properties assigned to cortical and cancellous bone were based upon experimentally verified material constants [74,75] as described in the previous chapter. Surface tie constraints were defined at the cortical/cancellous bone interfaces in order to prevent relative motion between all mated surfaces within the femur model.

The three IM nails were given isotropic material properties of the titanium alloy Ti6Al7Nb [104]. Additionally, it was also desirable to examine how a biocompatible polymer composite material with similar mechanical properties as cortical bone affected the interference-induced stress as well as the biomechanics of a healed femur treated with IM nailing. Therefore, an additional isotropic material was created to mimic CFR-PEEK as described in the previous chapter. Each nail was then assembled with the femur model having initial positions as illustrated in fig. 25.

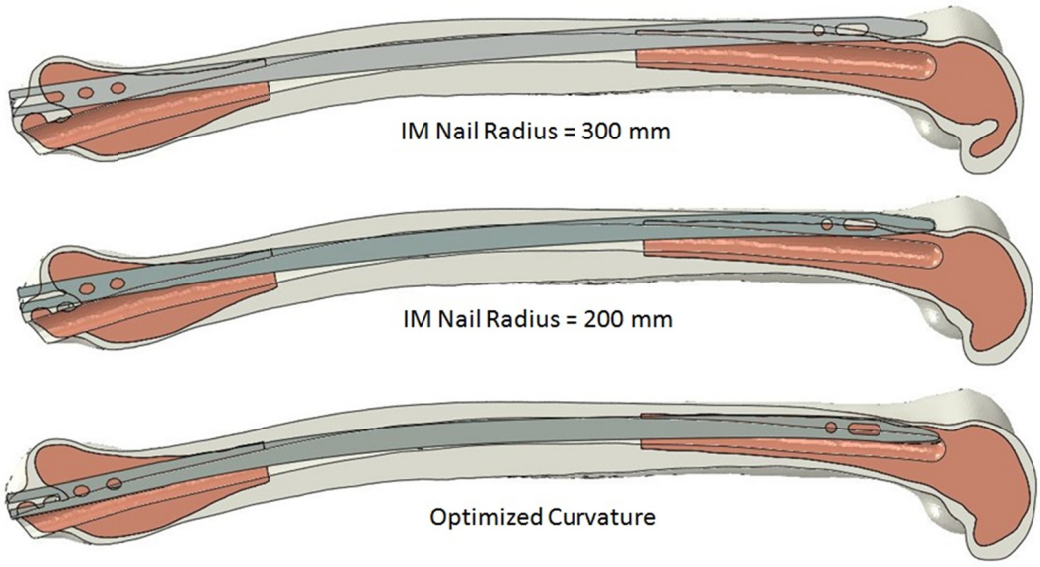

Fig. 25. Sagittal cross-sectional view of position of current and optimized nails within the femoral medullary cavity

Three static steps were defined for the analysis. Loads and boundary conditions were activated, deactivated, or modified at the beginning of each step to collectively achieve the desired result – an interference fit of the IM nail within the medullary canal. A fourth static loading step was added to simulation the impact of a sliding hammer on the proximal end of the nail.

In the initial step, a displacement constraint (DC1) is activated at a pair of nodes mid-length on the nail which allows zero degrees of freedom. A similar displacement constraint (DC2) is applied at the hip joint. The displacement constraints are propagated throughout all analysis steps until modified.

During the first step, bending loads of approximately 1,200 N (270 lbf.) were activated. No contact constraints were activated between the nail and the anterior half

of the canal; however, contact constraints between the nail and the posterior half of the canal were activated. As the bending loads brought the nail into contact with the posterior canal wall, the contact constraints caused the femur to bend with the nail (fig. 26). Frictionless tangential interface and "hard" normal interface properties with separation allowed were assumed.

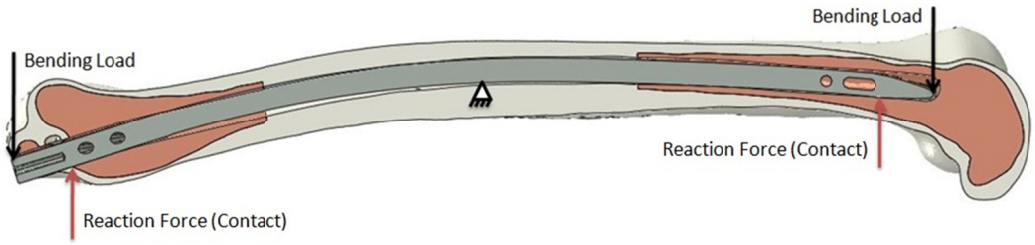

Fig. 26. Analysis step 1: bending

In the second step, the bending loads were deactivated. This allowed the nail to elastically spring back to its original position. However, contact constraints between the nail and the anterior half of the canal wall were activated at this point in time. As the nail sprung back, it came into contact with the anterior half of the canal wall causing the femur to bend against its natural curve (fig. 27).

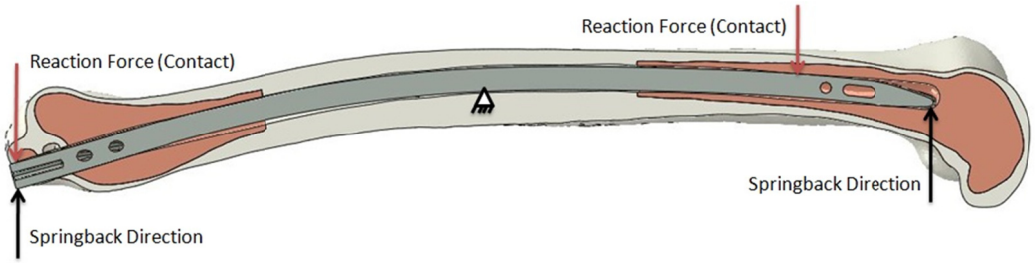

Fig. 27. Analysis step 2: proximal/distal springback

During the third step, the displacement constraint DC1 was modified so that the constrained nodes could translate in the direction normal to the coronal plane. This allowed the middle section of the nail to spring back towards the posterior half of the canal - where the initial contact constraints remained activated (fig. 28). During this step, the displacement constraints at the knee joint are deactivated so that only the femur's hip joint is constrained. This allows the femur to bend in response to the springback force of the nail.

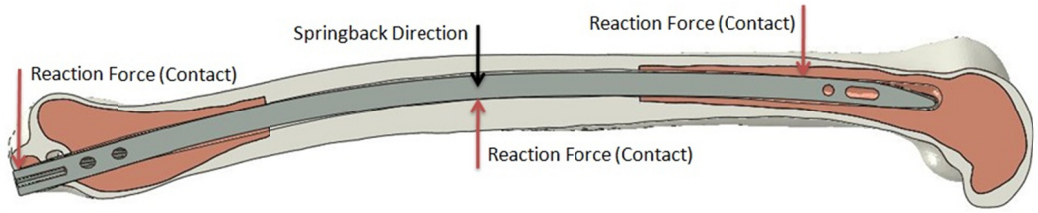

Fig. 28. Analysis step 3: mid-point springback

In the fourth step, a force load of 800 N (180 lbf) was applied at the distal end of the nail to simulate the impact of a sliding hammer during insertion. The force magnitude was calculated with Newton's second law

$$F = ma = m\frac{\partial v}{\partial t} F = ma = m\frac{\partial v}{\partial t} \ , \qquad \text{(XIV)}$$

where m is mass, ∂v is the change in velocity, and ∂t is the impact time duration. The values for m, ∂v, and ∂t were assumed to be 20 ounces (0.567 kg) , 15 m/s, and 0.01 s, respectively. The fixed hip joint constraint remains activated to simulate the reaction force at the joint during impact. Beginning in the fourth step and throughout the rest of the analysis, where the actual response values were of interest, nonlinear large deformations were accounted for in the finite element solver.

Finally, in the fifth step, a static load of 250 lbs. was applied at the hip joint to simulate the effect of an individual standing with all weight on the treated leg. Transverse screws were not used to secure the nail - which is typically done to provide rotational stability. Since prior to analysis it is unknown where the nail's transverse screw holes will be positioned with respect to the femur when fully inserted, the following approach was taken to secure the nail. Tangential contact constraints between the nail and reamed canal wall were redefined at this step so that no relative sliding between contact surfaces was allowed. Additionally, normal contact constraints were redefined so that surfaces in contact were not permitted to separate.

The loading and boundary conditions described above were also applied to a model featuring the straightest femur (highest radius of curvature) in the sample and the optimum nail (fig. 29). However, this time the contact constraints at the anterior canal surface were activated first as the nail was bent in the opposite direction. The reasoning behind choosing the maximum and minimum radius femora in the sample is that if it can be shown that an IM nail with an “average” curvature can be fit into the two extreme femora, then it can be inferred that the nail can accommodate the entire sample population.

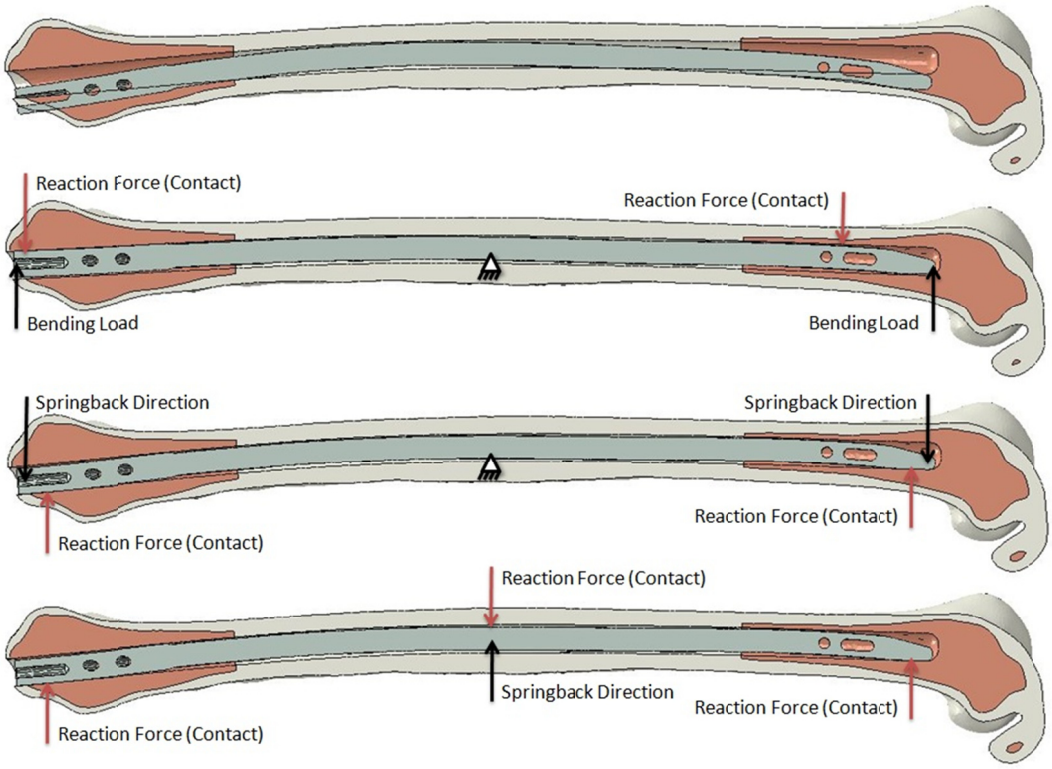

Fig. 29. Progression of static analysis steps taken to achieve interference fit (in order from top to bottom) 1.) initial assembly, 2.) bending, 3.) springback 1: proximal and distal ends, and 4.) springback 2: mid-section

Solid meshing for each model was achieved using approximately 524,000 linear tetrahedral elements with an average edge size of 2 mm (fig. 30-Fig. 32). All mesh quality specifications discussed in the previous chapter were met.

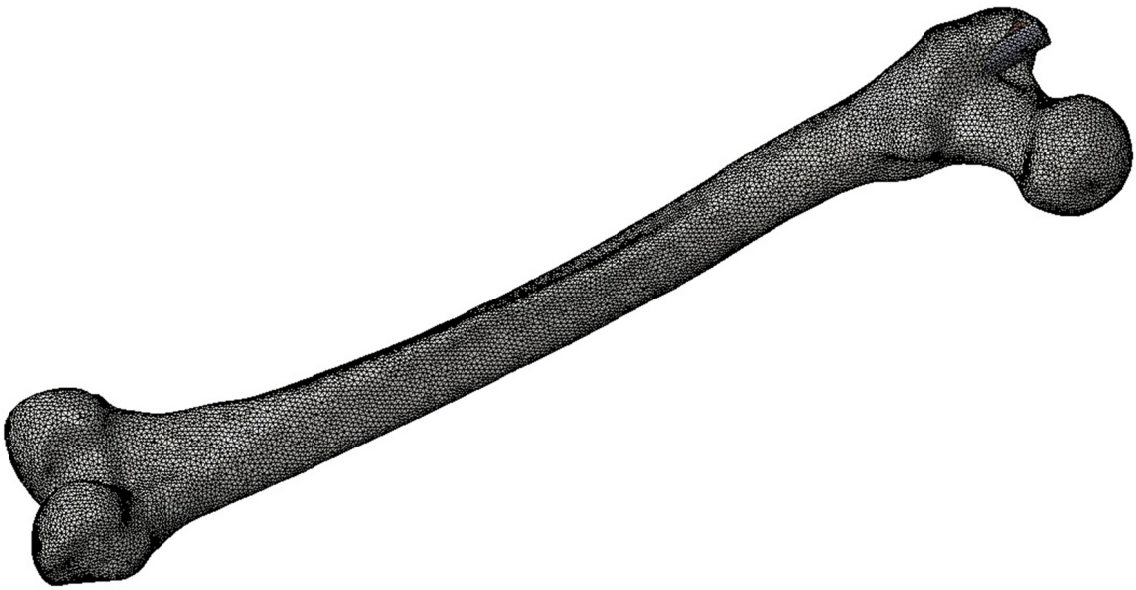

Fig. 30. Meshed finite element model

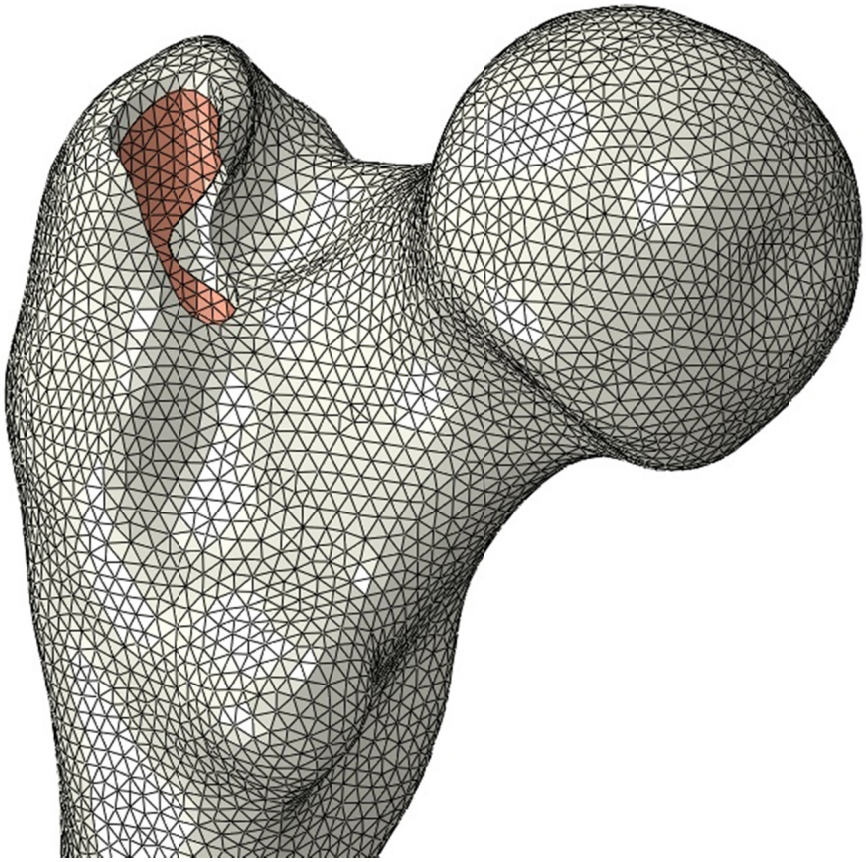

Fig. 31. Proximal end of meshed femur

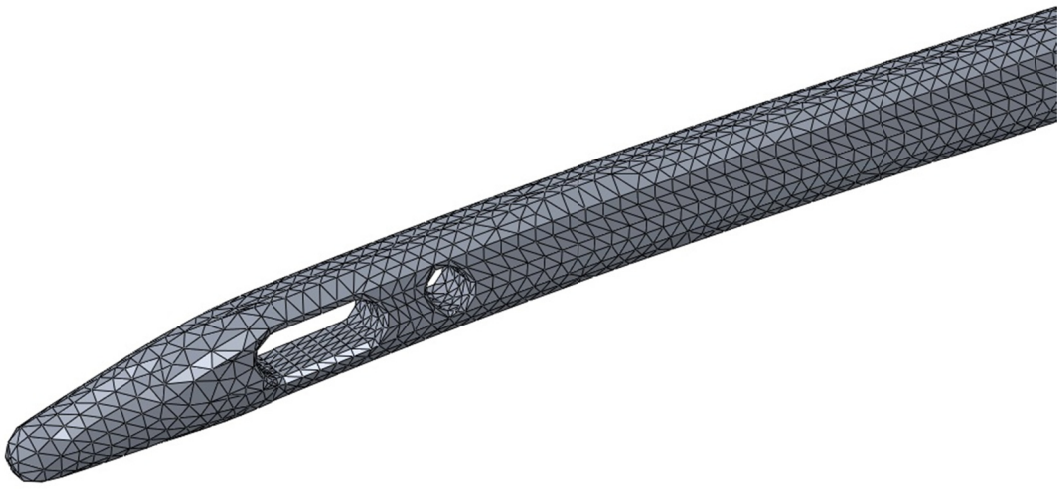

Fig. 32. Distal tip of meshed IM nail model with optimized curvature

9. Structural Optimization

Assessing the effect of various design parameters on performance was not essential for solving the problem regarding current IM nail designs. Therefore, this case study does not include a parametric analysis. However, building off the results of this case study regarding nail curvature and material, a comprehensive design process for a new IM nail system could be carried out. Design parameters would include those pertaining to transverse screws (quantity, size, orientation, etc.), longitudinal grooves, fabrication materials, surface finish, treatment processes (annealing, quenching, etc.), among others.

IM nail length and diameter, the major geometric parameters affecting the structural performance of the nail, are determined by the individual patient's geometry. The appropriate nail size is selected by the physician after examining the patient's leg via X-ray or CT imaging. Additionally, the scope of the present case study is concerned

with the integrity of the femur during IM nail insertion and the effect the nail has on the femur's biomechanics post-operation. Therefore, structural optimization is not applied to this case study.

10. Experimental Testing

The MTS universal testing machine and femur fixture were used to measure the force necessary to insert the current and optimal IM nails at a constant velocity of 0.01 in/s – as was well as to verify the finite element models. Prototypes of the optimal IM nail and a nail with a 200 cm radius were fabricated from mild steel rods – each with a 0.5" diameter (fig. 33, see Appendix A for technical drawings). The desired curvature was obtained using a CNC bending machine where the nails were bent at one-inch increments (fig. 34). The appropriate bend angle at each increment was calculated to achieve the desired curvature. Springback was taken into consideration by multiplying the bend angles by a springback factor; this was determined by bending a rod 1° and measuring the actual bend angle. The final curvature profile of each nail was measured with a quality control device and verified with the technical drawings (fig. 35). A Sawbones composite femur with an intramedullary canal diameter of 13 mm was used as the test specimen. A 13 mm diameter hole was drilled and reamed into the greater trochanter – tangentially meeting the canal. Because a local maximum in the strain field at the anterior mid-diaphysis was calculated for each of the finite element analyses simulating nail insertion (see following *Results* section), a strain gauge rosette was

fixated to this location on the Sawbones specimen. Fig. 36 shows the experimental set-up using an MTS Universal Testing Machine.

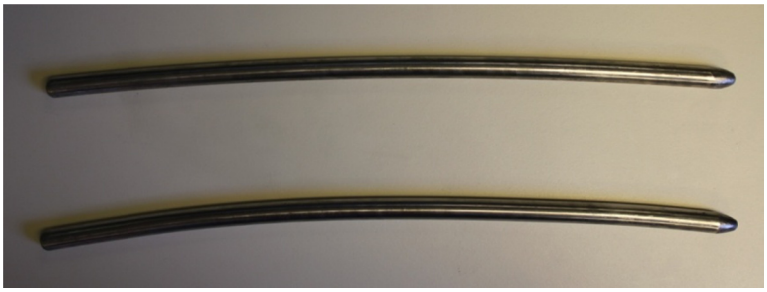

Fig. 33. Prototype IM nails (*top*: R = 200 cm, *bottom*: optimized curvature)

Fig. 34. CNC bending machine at Hubbell Power Systems, Centralia, MO

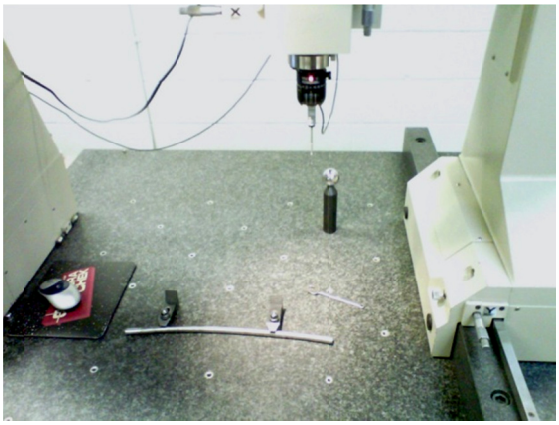

Fig. 35. Optical quality control device used to insure prototype IM nail geometry matches design specifications (courtesy of Hubbell Power Systems, Centralia, MO)

Fig. 36. Experimental setup: MTS universal testing machine with femur fixture, Sawbones composite femur, and prototype IM nail

Results

Femoral Geometry Statistics

Sex was found to have the greatest influence on femoral size; in general, males tend to have larger bone geometry features than females. Regarding femoral shape (*i.e.* radius of curvature and location of the most anterior point along the diaphysis), race was the highest contributing factor; however, even race did not show significant correlation ($p \geq 0.05$) in this pilot study.

The radius of curvature (*R*) of the medullary canal ranged from 77.6 cm to 210.1 cm with an average of 121.5 cm and a standard deviation of 33.2 cm. Although the average curvature radius for African Americans was higher than Caucasians (127.5 cm and 115.3 cm, respectively), no significant correlation was found between curvature and race (see Table 3). In fact, none of the population factors had a significant correlation with curvature.

Table 3. ANOVA *p*-values (statistical significant: $p < 0.05$)

	R	*L*	*SL*	*OD*	*ID*	*T*	L/OD	*LMAP*
Race	0.258	0.046	0.009	0.019	0.672	0.117	0.795	0.064
Sex	0.552	0.000	0.003	0.000	0.007	0.001	0.000	0.346
Age	0.872	0.611	0.290	0.581	0.151	0.451	0.137	0.759

***R* = radius of curvature, *L* = length, *D* = diaphyseal length, *PD* = periosteal length, *MD* = medullary length, *L/PD* = *L* to *PD* ratio, *LMAP* = location of most anterior point**

The location of the most anterior point on the shaft as a function of percent length from the proximal end (*LMAP*) ranged from 27.2% to 50.1% with an average of 38.1% and standard deviation of 5.4%. Race was found to have the greatest impact on

this measurement. However, the *p*-value was slightly greater than 0.05 ($p = 0.064$); therefore, no significant correlating factor was found.

The total femur length (*L*) ranged from 41.3 cm to 52.9 cm with an average of 45.9 cm and standard deviation of 2.7 cm. Diaphyseal length (*DL*) ranged from 27.4 cm to 36.7 cm with an average of 31.1 cm and standard deviation of 1.9 cm. Sex had the most significant correlation pertaining to both *L* and *DL*. Race also showed significant correlation for both measurements. In general, males and African Americans had longer femora compared to their counter sub-population groups.

The periosteal diameter (*PD*) at mid-shaft ranged from 2.37 cm to 3.56 cm with an average of 2.80 cm and a standard deviation of 0.29 cm. Sex had the most significant correlation on *PD* with an average of 3.02 cm for males and 2.59 cm for females. Race also showed significance in correlation with *PD*, where African Americans and Caucasians averaged 2.87 cm and 2.74 cm, respectively. The medullary diameter (*MD*) ranged from 1.06 cm to 2.00 cm with an average of 1.51 cm and a standard deviation of 0.22 cm. Only sex showed strong correlation with *MD* where the averages for males and females were 1.59 cm and 1.42 cm, respectively.

Sex was the only factor that showed strong correlation with cortical wall thickness (*T*) where the average thickness was measured to be 0.71 cm for males and 0.58 cm for females (total range: 0.28-0.91 cm, average: 0.65 cm, standard deviation: 0.28 cm,). The ratio of femoral shaft length to periosteal diameter (*L/PD*) ranged from 9.3 to 12.9 with an average of 11.2 and a standard deviation of 0.9. Again, only sex had a significant correlation on this ratio (male average: 11.8, female average: 10.6).

All geometry measures and statistics are found in Table 13 in Appendix A. These are beneficial for determining the number of sizes (*e.g.* IM nail diameter and length) required in order to accommodate the sample population. Although the inner diameter of a patient's intramedullary canal is reamed prior to insertion of the implant, the initial inner diameter and wall thickness determine the final reaming and nail diameters. Although the present statistical analysis shows a significant variation in femoral curvature, the necessity for multiple IM nail shapes is determined through finite element analysis as follows. As previously stated, no significant correlation between curvature and the three population factors (*i.e.* race, sex, and age) was found in the pilot study; therefore, evidence was not found that showed a need for developing different nails for different sub-populations.

Virtual Surgery

Fig. 37-Fig. 42 depict the von Mises stress fields resulting from the interference fit of each nail with the femur. Local maximum stresses at regions of stress concentration are also labeled. The FEA results from the hammer impact simulations are illustrated in Fig. 43. Finally, the simulation results comparing femur biomechanics due to standing with different IM nails are shown in fig. 45–fig. 47.

The tangential compressive strength of cortical bone is approximately 130 MPa with a yield strength of 114 MPa [74]. The allowable stress was calculated to be 60.8 MPa by taking into consideration that the yield strength of cortical bone decreases with age by approximately 20% [75] and by implementing a safety factor of 1.5. In the

following figures showing the FEA results, regions in red denote stresses predicted to exceed this allowable maximum. This pertains to the femur only, as the titanium IM nail is much stiffer but also has a significantly greater yield strength (approximately 800 MPa for Ti6Al7Nb).

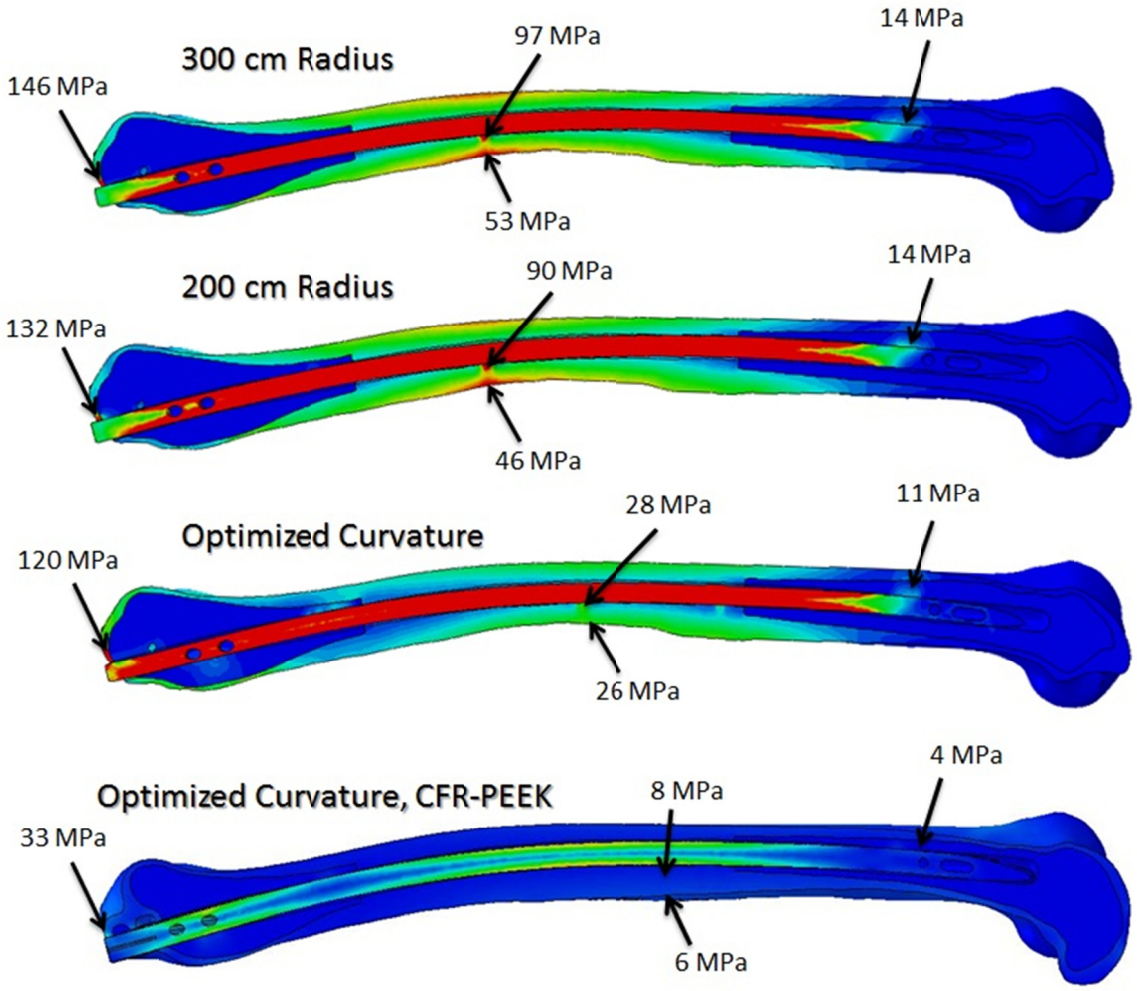

Fig. 37. FEA results: nail/femur interference fit - minimum radius femur

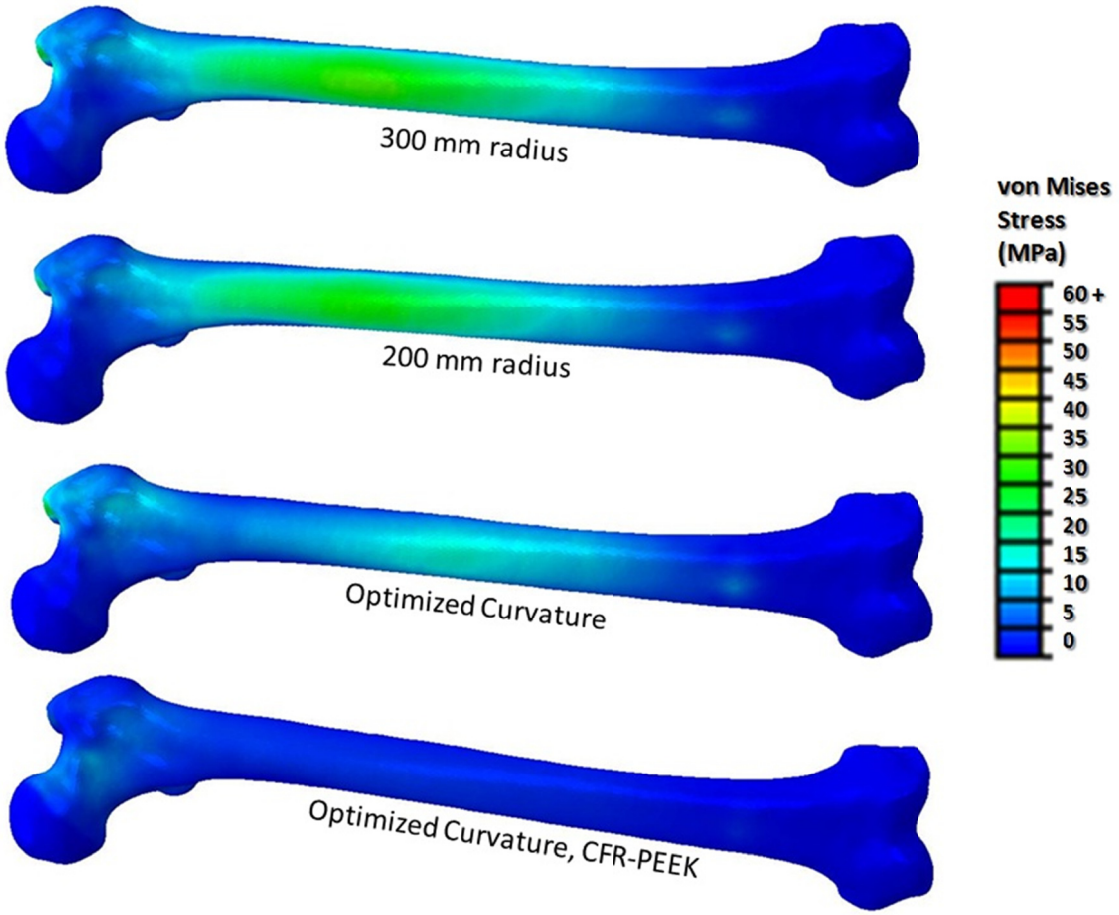

Fig. 38. FEA results: nail/femur interference fit - minimum radius femur (anterior view)

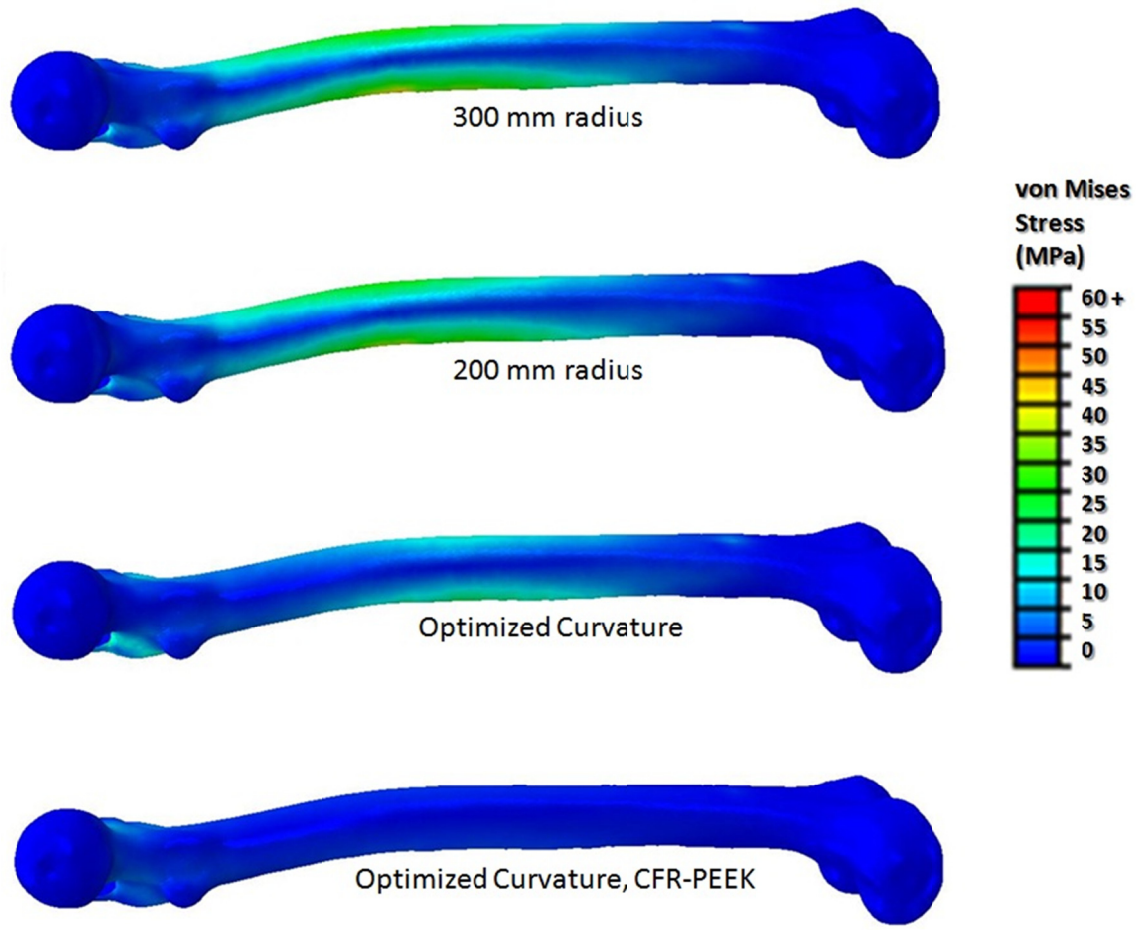

Fig. 39. FEA results: nail/femur interference fit - minimum radius femur (medial view)

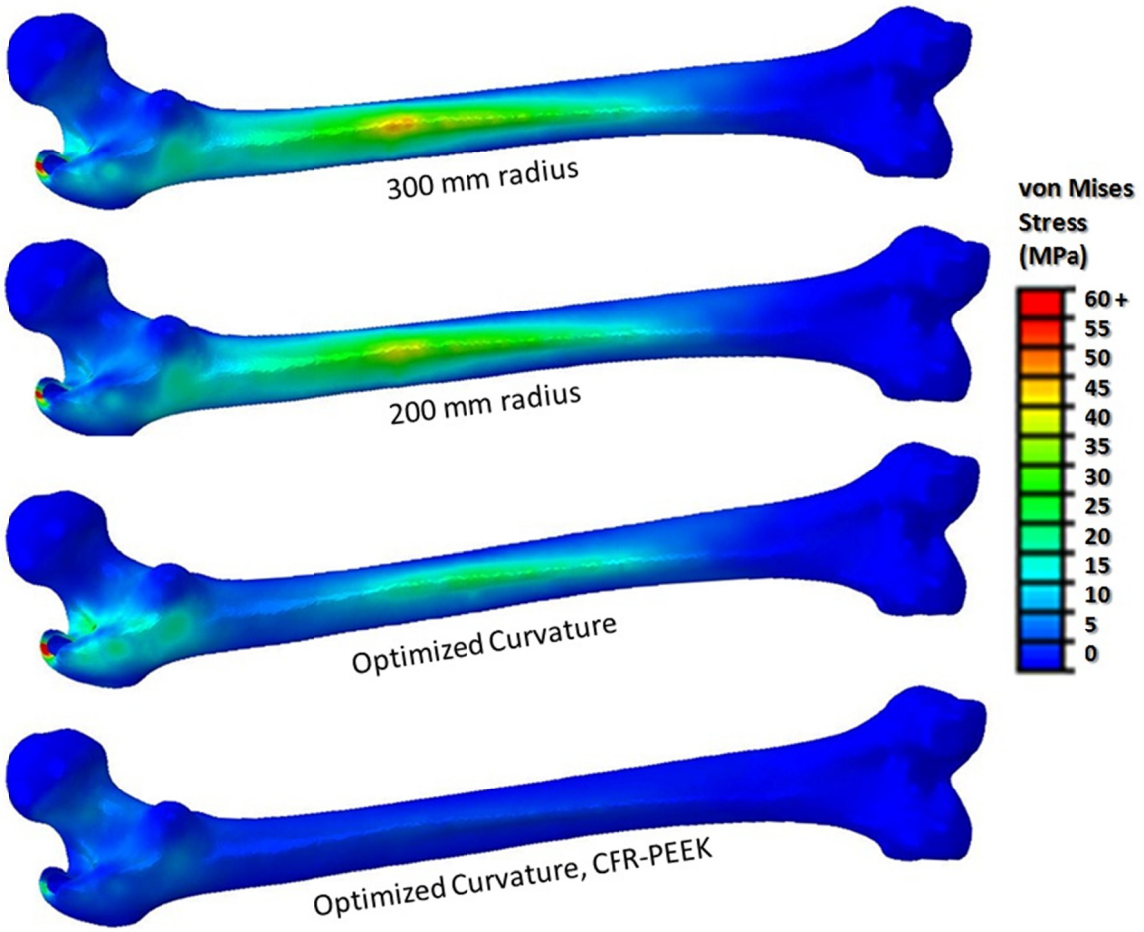

Fig. 40. FEA results: nail/femur interference fit - minimum radius femur (posterior view)

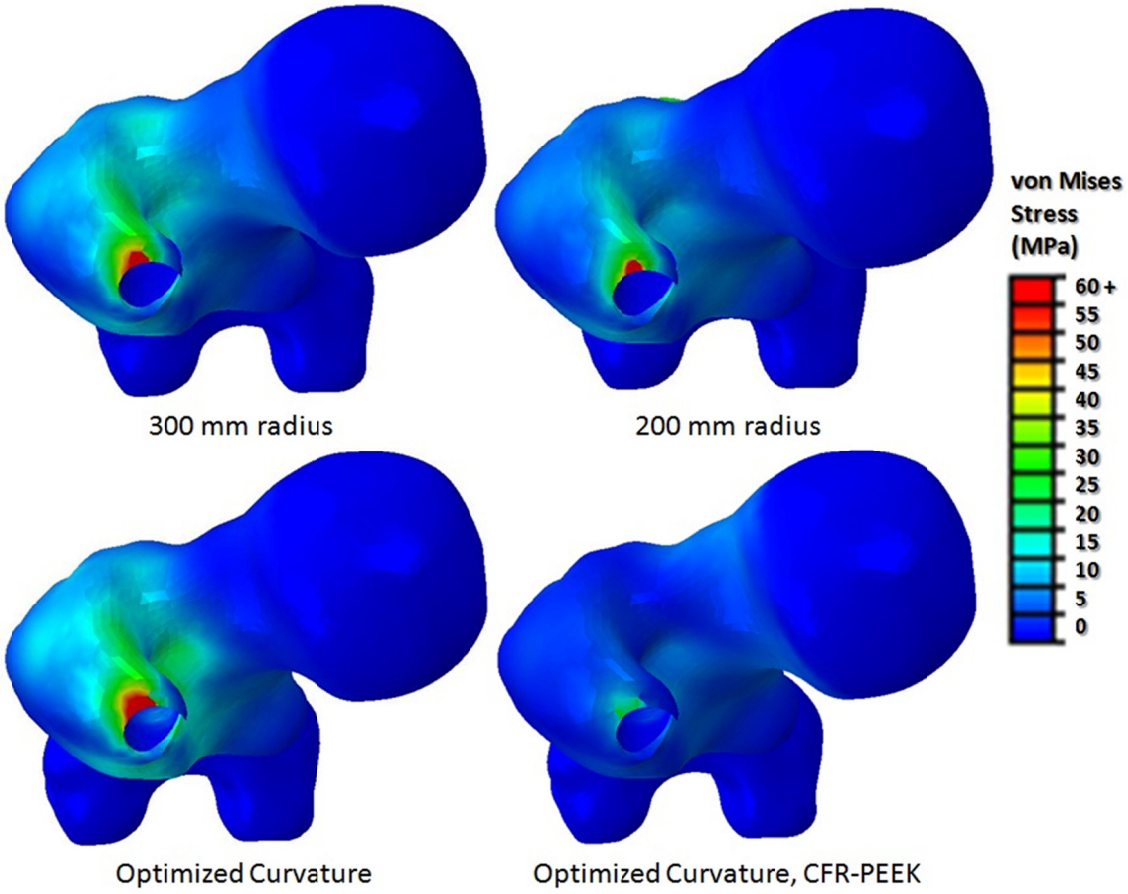

Fig. 41. FEA results: nail/femur interference fit - minimum radius femur (proximal view)

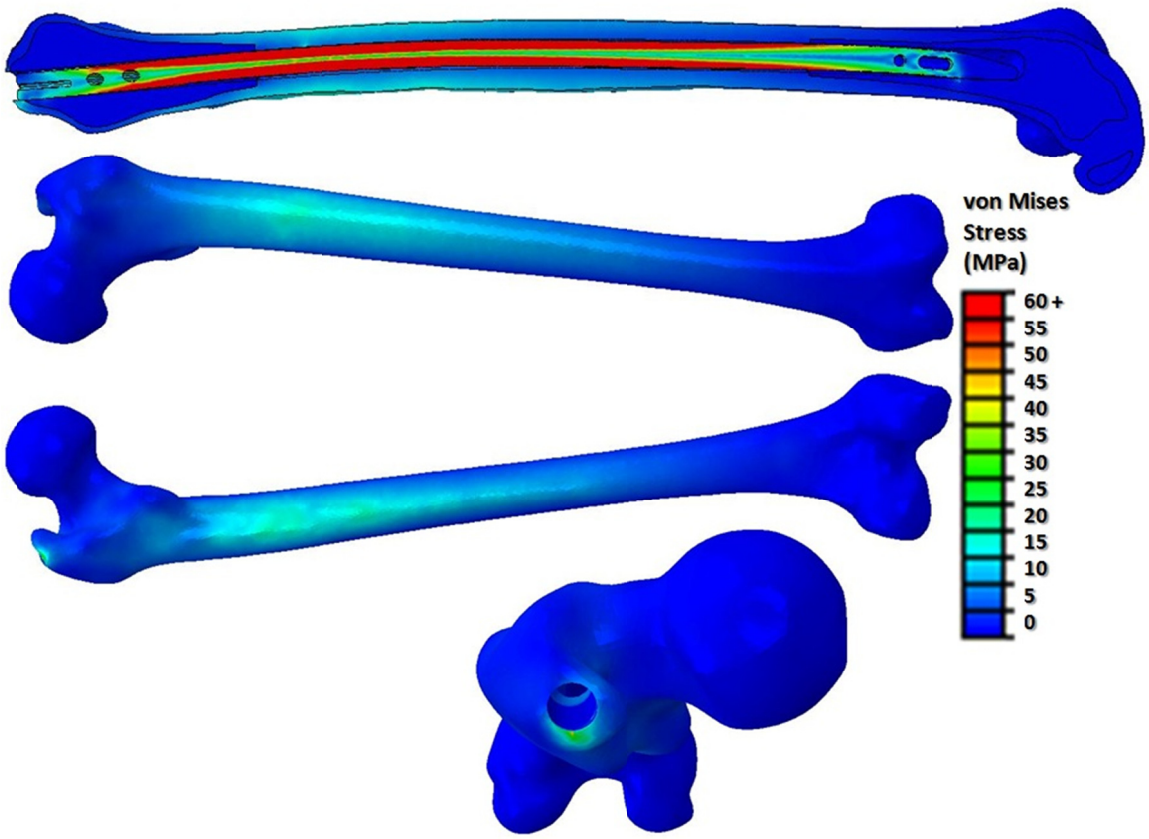

Fig. 42. FEA results: interference fit with optimized IM nail and maximum radius femur

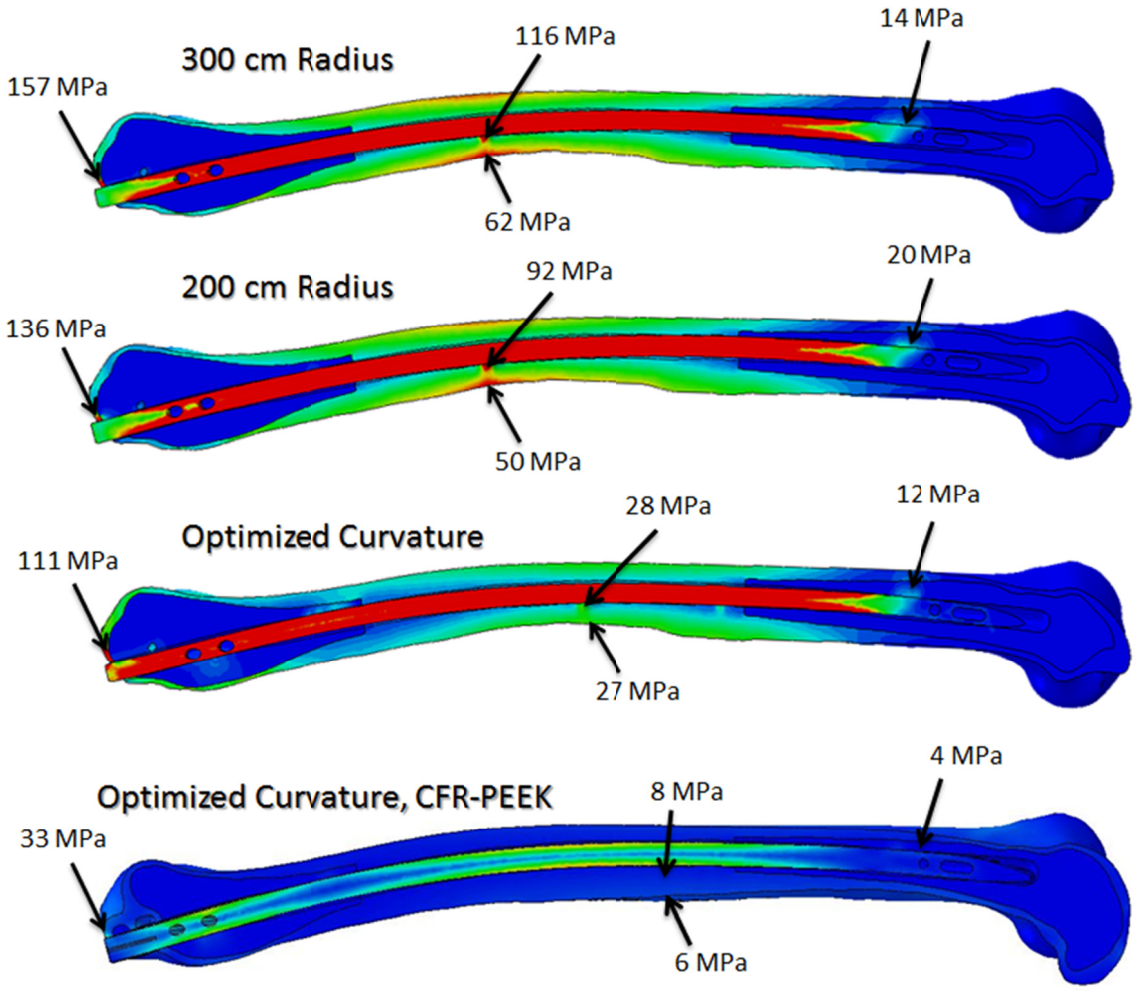

Fig. 43. FEA results: hammer impact - minimum radius femur

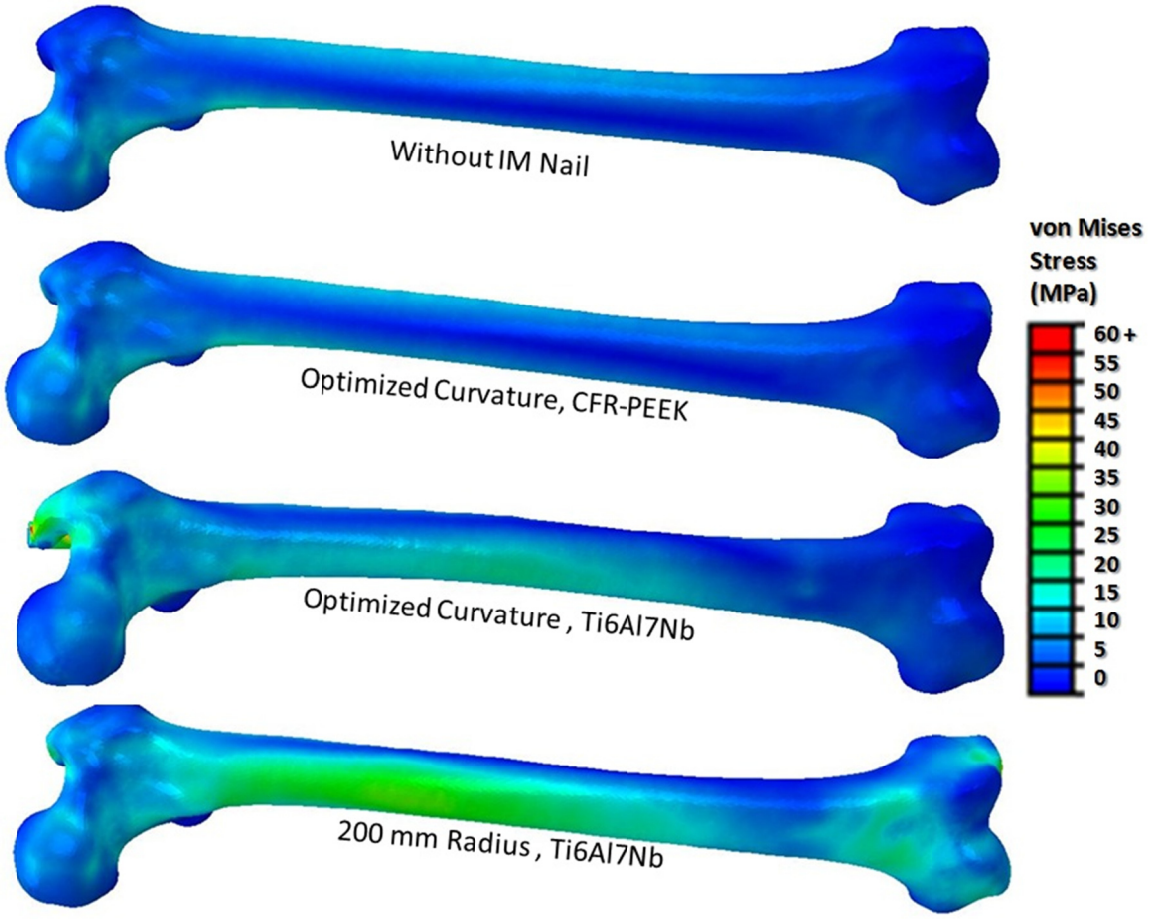

Fig. 44. FEA results: standing - minimum radius femur (anterior view)

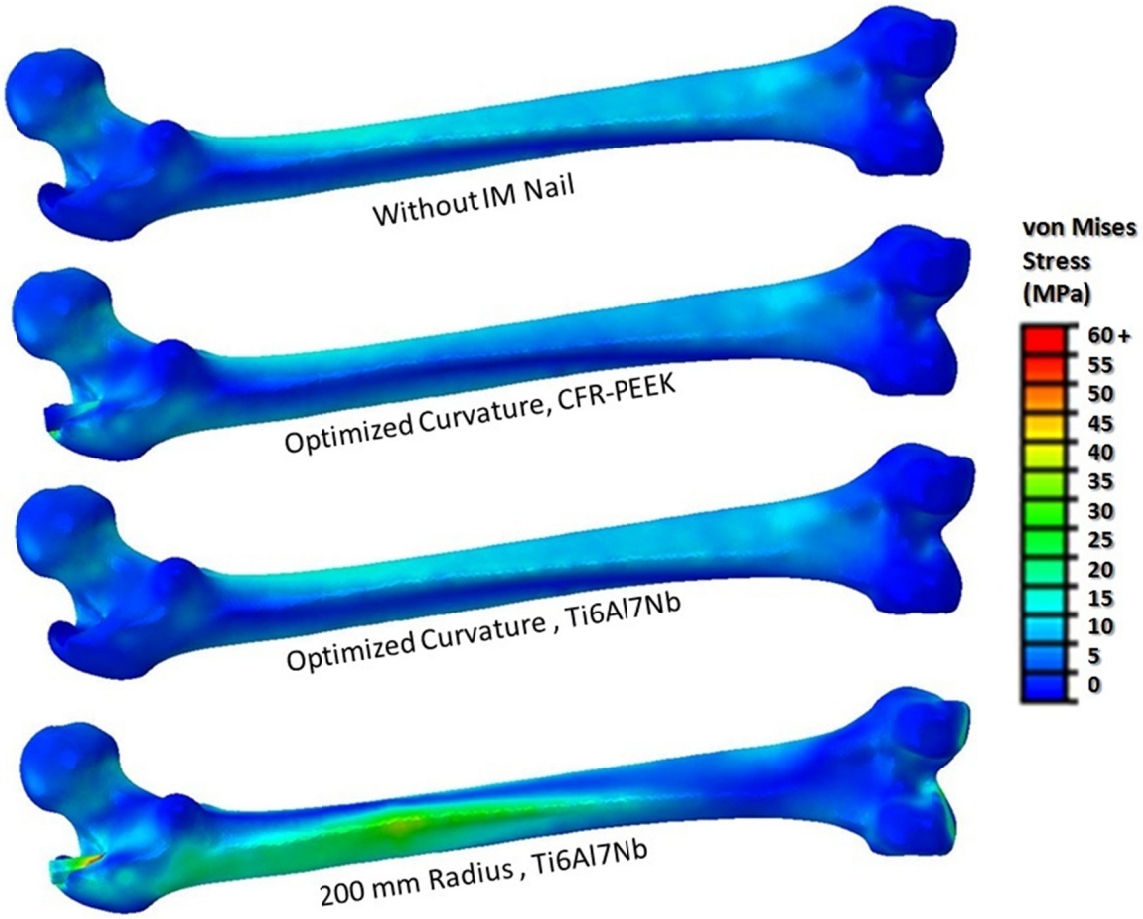

Fig. 45. FEA results: standing - minimum radius femur (posterior view)

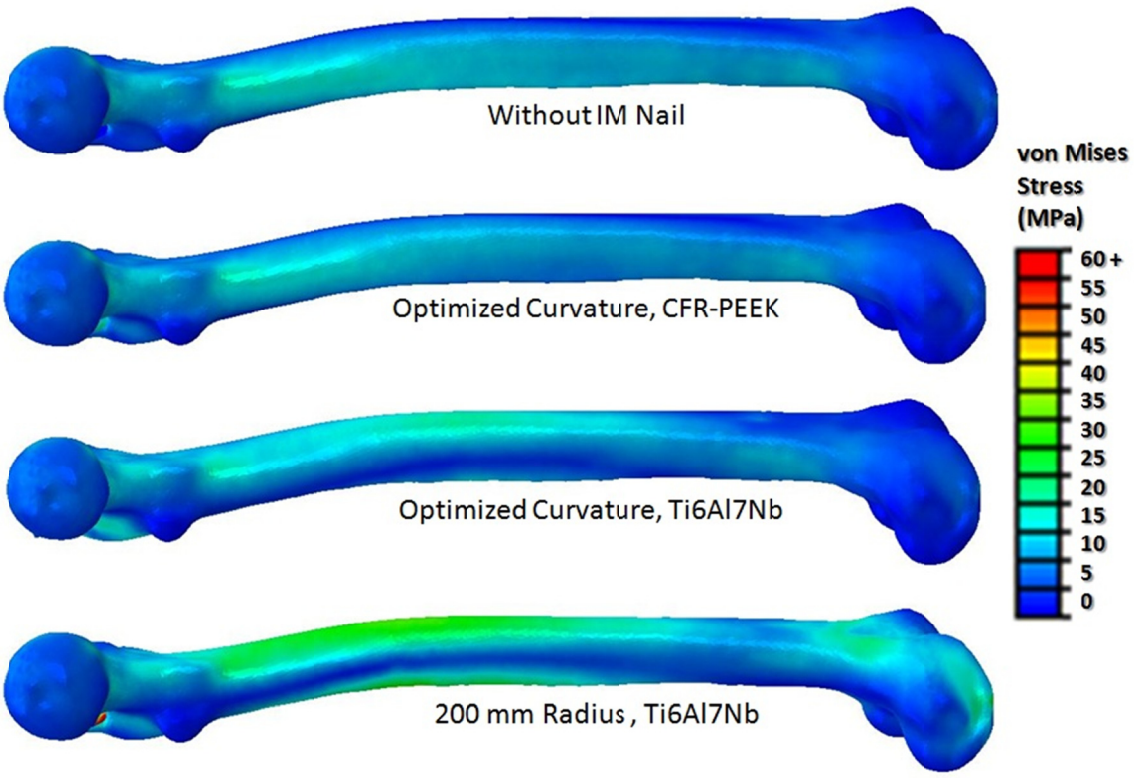

Fig. 46. FEA results: standing - minimum radius femur (medial view)

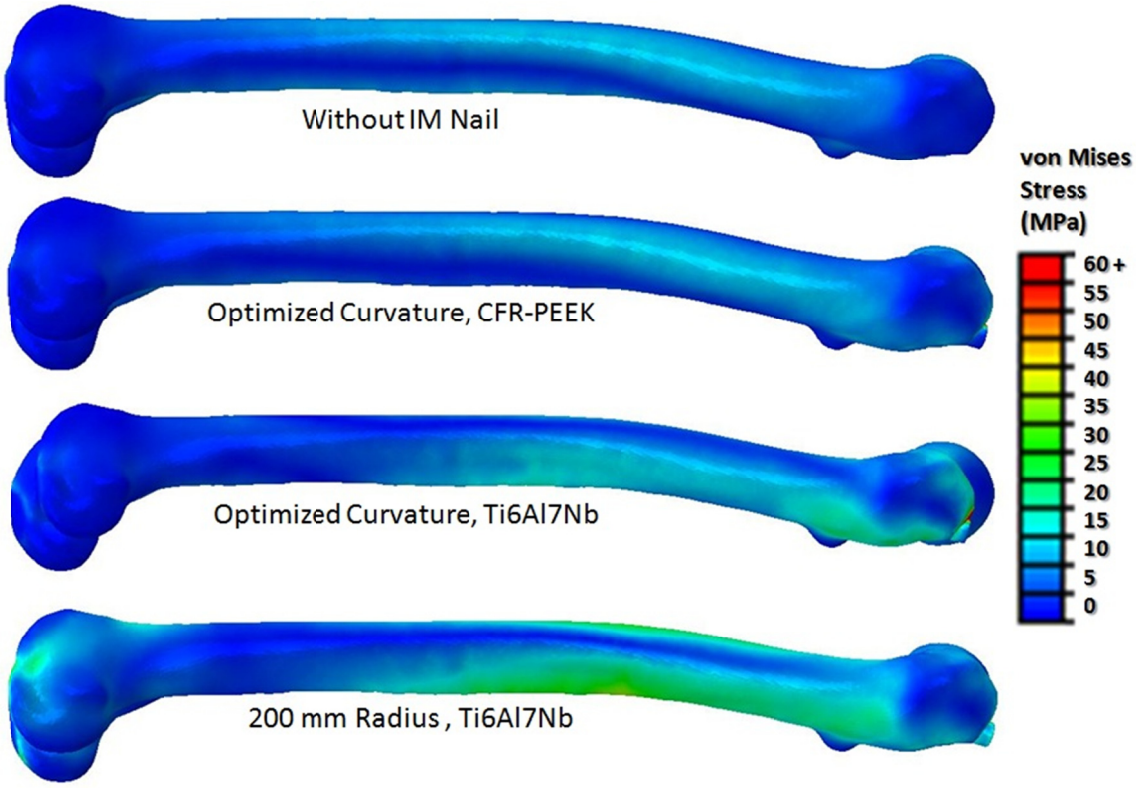

Fig. 47. FEA results: - minimum radius femur standing (medial view)

For the minimum radius femur with IM nail interference fit, a general decrease in femoral von Mises stress was observed using the geometrically optimized nail as opposed to the 200 and 300 cm radius nails. The stress within the posterior canal wall generated after the 200 cm radius and 300 cm radius nails were inserted exceeded the allowable stress. With titanium as the nail material, all three nail models yielded stresses around the proximal entry point that exceeded not only the allowable stress but also the yield stress. However, this problematic area of stress concentration was reduced below the allowable maximum limit with the optimized IM nail fabricated from CFR-PEEK.

For the maximum radius femur fitted with the optimized IM nail, the maximum von Mises stress remained well below the allowable stress.

The simulated hammer impact had very little effect on the stress generated where the distal tip of the nail comes into contact with the canal wall. A greater curvature mismatch between the nail and femur seemed to result in a larger percent difference between stresses induced only by interference fit and corresponding impact-induced stresses. The mid-diaphyseal and proximal regions of the femur were the most affected by the hammer impact. However, even in these regions the stress increase was only between two and twenty percent.

The stress distribution in the femur during simulated standing varied significantly when the femur was fixated with a titanium IM nail compared to an untreated intact femur. The closer the nail geometry matched the canal curvature (*i.e.* optimized nail verses 200 cm radius nail), the more closely the stress in the treated femur matched that of the untreated femur. However, nail material had the greatest impact on femoral stress during standing as the stress distribution with a CFR-PEEK nail was virtually identical to that without IM nail fixation.

Experimental Testing

The experimental results of IM nail insertion comparing the optimized nail with the 200 mm radius nail are illustrated in fig. 48–fig. 50.

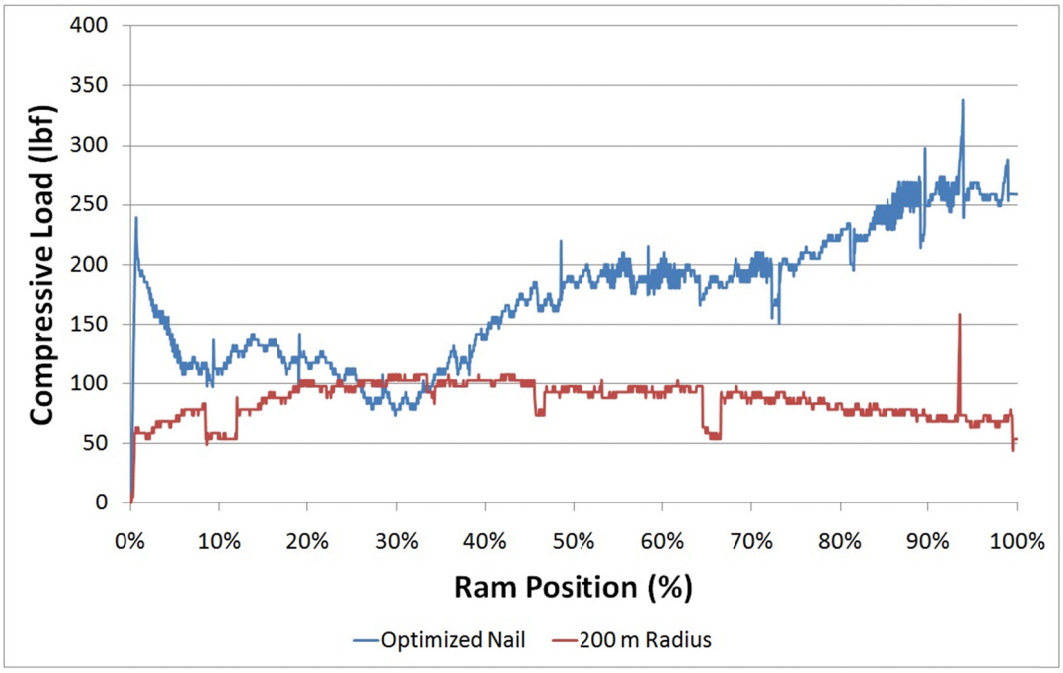

Fig. 48. Load measured during IM nail insertion at a constant velocity of 0.01 in/s

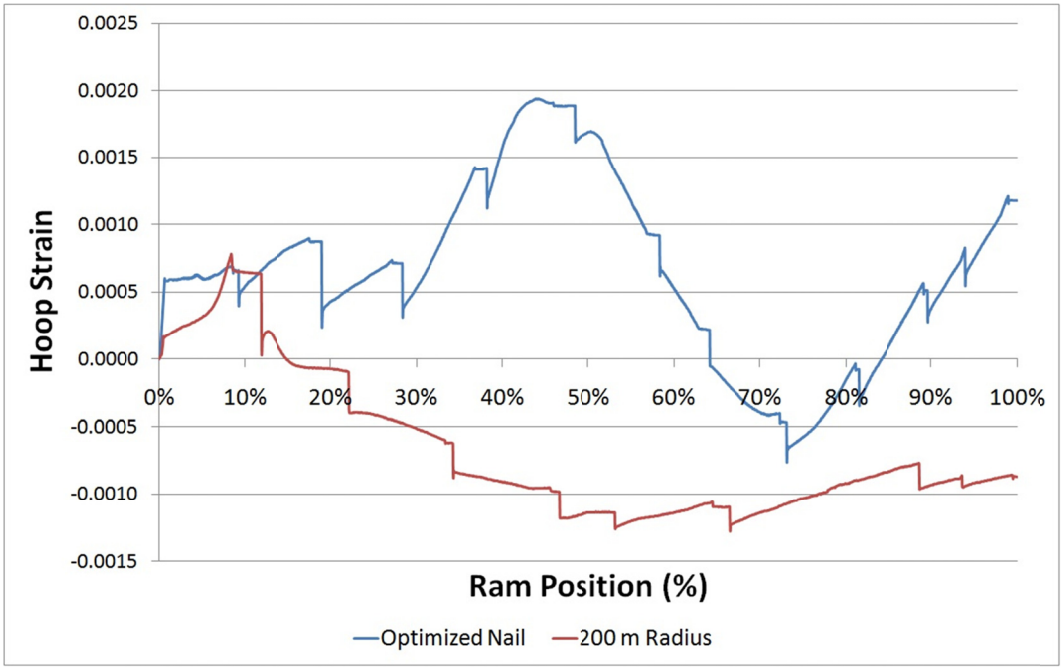

Fig. 49. Hoop strain measured by strain gage during IM nail insertion at a constant velocity of 0.01 in/s

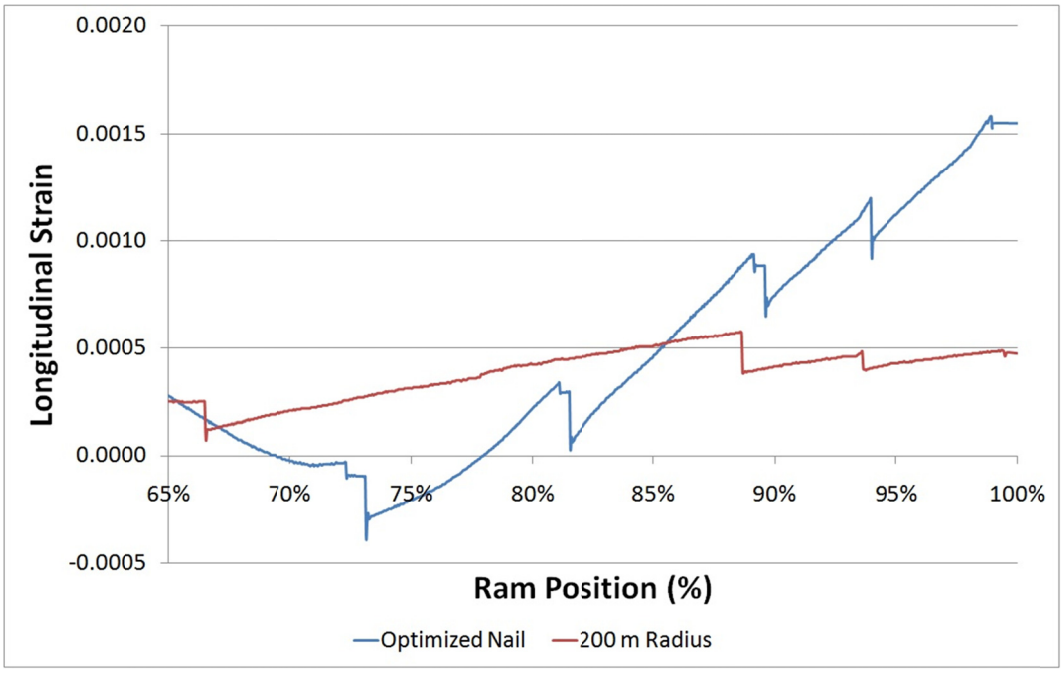

Fig. 50. Longitudinal strain measured by strain gage during IM nail insertion at a constant velocity of 0.01 in/s

Discussion

Femoral Geometry Statistics

The relatively small samples used in this study need to be expanded to ascertain the optimum number of geometries and metric variation in humans from which to determine how many nail shapes would be economically or clinically feasible or appropriate. However, this initial study supports the hypothesis that sub-groups of adults vary in different ways in aspects of femoral geometry, and that considering human variation when designing IM nails will be important.

Results from this study suggest that patients of different sex and race tend to vary in femoral size, but not in curvature as the radius of curvature range for both African Americans and Caucasians overlapped significantly. Femoral size or curvature

does not appear to change throughout adult life, or at least does not vary between the younger and older groups of adults (30's and 70's) in this study. However, a previous study with a larger sample did find significant correlation [87] between race and femoral curvature. Both the present and cited studies found that the average radius of curvature for African Americans was larger than that of Caucasians.

Because the location of the most anterior point was found to be fairly consistent among the sample femora, it can be inferred that the same general shape is found within the sample population. In other words, the locations along the length of the femoral shaft where maximum and minimum curvatures occur are relatively consistent.

Virtual Surgery & Experimental Testing

Results of the finite element analysis simulating the insertion of the geometrically optimized IM nail showed that the stresses induced in the femoral shaft were within the allowable range. Since the femora having the highest and lowest curvature in the sample were used for analysis, it is probable that the average curvature function is sufficient for the entire population. Therefore, no additional curvature "sizes" would be necessary. With titanium alloy as the nail material, stresses adjacent to the proximal entry hole which exceeded the allowable stress could be reduced by moving the hole towards the anterior margin.

Whereas failure was predicted at mid-shaft with both the 200 and 300 cm radius nails inserted into the minimum radius femur, the stresses induced in the distal shaft were relatively low and nearly identical for all three nails. Here, contact was made

between the nails and the porous cancellous bone which has a much lower effective modulus than cortical bone. Yielding and microfractures within cancellous bone along the canal are expected during the reaming process; however, cortical bone is a much greater contributing factor towards the overall mechanical integrity of the femur. In the distal region of the femur, the stresses within cortical bone remain well below the allowable stress - even when considering age degradation.

While stresses within the minimum-radius femur were significantly lower with the optimized nail verses the two commercial nails *when the nails were in their final position of insertion*, the experimental tests showed that for some femora, such as the Sawbones composite femur, the forces required for insertion may be greater for the optimized nail. Additionally, the strain – and therefore stress – could also be greater with the optimized nail. This is largely due to the fact that the optimized nail has a lower curvature in the distal region, so as it passes through regions of the canal where the curvature is high, a greater amount of bending in the femur – as well as the nail – occurs to accommodate the curvature mismatch. The more bending required, the greater force necessary to insert the nail.

However, the objective of the shape optimization technique applied to IM nail geometry is to determine a curvature function that best fits the *entire* population, not just certain cases. In other words, one curvature function that is sufficient for the wide variation in human femoral curvature would be used as a "one shape fits all" - while still allowing for the selection of various sizes (*e.g.* length and diameter). According to the

present study, an optimized nail fabricated from titanium alloy seems to be a possible solution to the current problem with IM nailing.

An even more effective solution would be to fabricate IM nails from a biocompatible, high-strength composite with a similar elastic modulus as cortical bone – such as CFR-PEEK. The current study has shown that not only does this significantly reduce stresses induced by curvature mismatch, but – compared to metal alloys – it also has negligible effects on the femur's biomechanics.

Femoral Locking Plate

Locking plate technology is commonly used in orthopedic trauma surgery to stabilize fractures in long bones such as the femur and humerus. This screw-plate system offers the possibility of using conventional screws – oriented at oblique angles (not perpendicular to the plate) if necessary – as well as locking head screws. Locking screws provide fixed angle stability and alleviate the need for plate-bone interface friction [105,106]. The locking plate technique can be used to treat numerous fracture patterns as it offers the surgeon many possible screw configurations. However, as the use of locking plates have increased due to much clinical success, clinical failures due to plate yielding and fracture have been observed [105,107,108]. These failures are not limited to any particular plate model [109]. The vast majority of failures are contributed to improper placement and fixation techniques, plate selection, and pre-mature weight-bearing by the patient [105,107,108]. While the mechanical function of locking plates is well-understood, the optimum parameters that lead to efficient stability and fracture healing, such as plate geometry and material properties, as well as the optimum fixation techniques, such as screw configuration and the use of hole plugs, are unknown [110-115].

Therefore, the simulation-based implant design and optimization techniques will be used to determine the optimum design parameters for the purpose of damage management. Proper engineering design practice requires the application of a factor of safety when structural stability is a necessity. Particularly when dealing with the safety

of an individual, the factor of safety should be sufficiently high to prevent failure even under extreme or un-recommended environmental conditions, such as premature weight-bearing. A factor of safety can also compensate for fatigue failure – a common failure mechanism in many implants. It is therefore desirable and necessary to analyze the biomechanics of current femoral fixation systems under both typical and extreme physiological loading conditions in order to improve reliability of a new design.

A large number of experiments are required to adequately compare the various parameters of interest under these conditions, making traditional mechanical testing methods inefficient. Additionally, the complicated time-dependent static and dynamic loads are difficult and expensive to replicate by machine. Therefore, simulation-based techniques will be used to simulate the behavior of current plate models under various loads and predict failure. A successful study would provide surgeons with crucial information regarding the improvement of fixation techniques and plate selection and well as provide manufactures with data that would improve overall plating system designs. This in turn would improve the overall quality that orthopaedic trauma patients receive.

Methods & Materials

Steps 1–6: Digital Reconstruction and Analysis of Specimen Samples

Since locking plate systems and IM nailing are both standard treatment techniques for femoral fractures, the present and previous case studies share the same initial six steps - beginning with acquiring femoral specimen samples and ending with the generation of average femoral models.

7. Contour Optimization

Current distal femoral plating systems are designed for fixation at the lateral side of the femur. This is based on the assumption that typical physiological loading causes medial bending of the femur – resulting in compression at the fracture interface (as opposed to lateral bending which would lead to the fracture gap expanding). Compression at the fracture gap is imperative due to the nature of bone remodeling: bone requires stress to heal.

On average, the loading direction at the hip joint in the coronal plane is approximately 5-10° medially with respect to the diaphyseal axis. In this case, the reaction force at the knee joint is distributed so that 60% is across the medial condyle and 40% is across the lateral condyle – leading to medial, or inward, mending. However, the significant variation in human skeletal geometry among the population could have a great impact on the loading angle, known as the *q* angle. For example, a patient with wider hips than the average individual would have a larger *q* angle. It is common knowledge among orthopaedic surgeons that approximately 10-15% of patients have a

q angle of 15° or more. As following simulation results will verify, a *q* angle of this magnitude will cause lateral bending – leading to expansion of the fracture gap if a laterally fixated plate is used. Therefore, the present case study focuses on the development of a plate that would improve the outcome for this minority of patients - otherwise known as a "medially locking plate" (MLP).

First, the average femur model was imported into Pro/Engineer (PTC, 2010), a CAD software package. Positioning of the plate relative to the femur was then defined by creating datum planes. The datum planes were positioned in such a way that the sagittal plane was parallel to a planar approximation of the medial epicondylar surface and approximately tangent to the diaphyseal surface. The coronal plane was then position 90° to the sagittal plane rotated about a linear approximation of the diaphyseal axis (fig. 51).

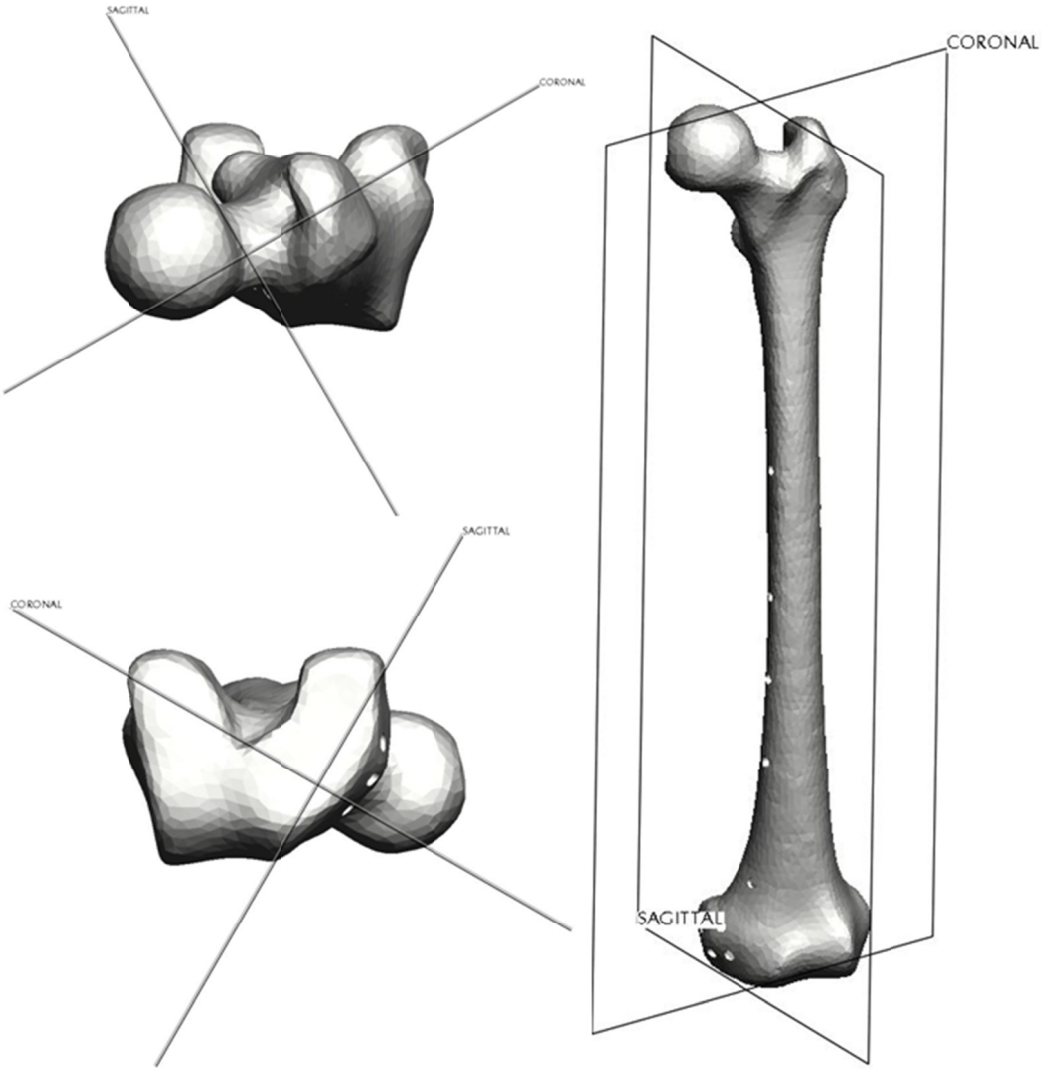

Fig. 51. Datum planes used for plate orientation

Next, a medial sketch of the MLP was created on the sagittal plane such that diaphyseal and condylar shape matched that of the average femur (fig. 52).

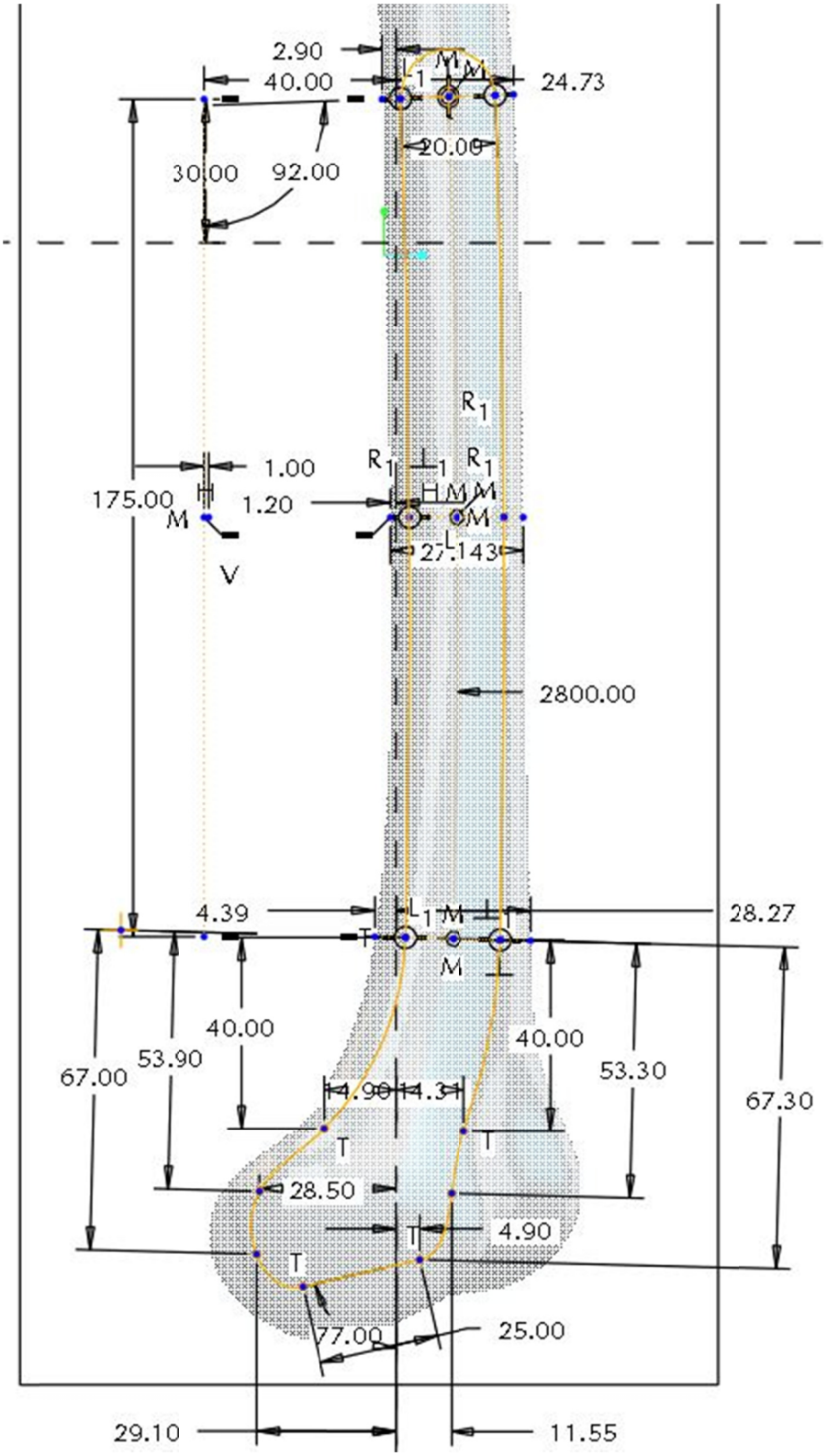

Fig. 52. Sketch of optimized medial profile over average femur

The medial sketch was then extruded in both normal directions so that the extrusion intersected the femur at all points within the cross-section and extended at least 1 cm beyond the most medial point on the medial epicondylar surface (Fig. 53).

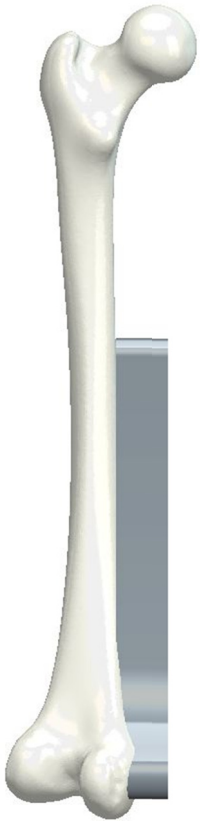

Fig. 53. Lateral profile extrusion

A sketch of the anterior profile – with an initial plate thickness of 5.0 mm – was then created on the coronal plane having a contour that matched the average femur (fig. 54). The sketch was then infinitely extruded in both directions, removing material where it intersected the initial medial/lateral extrusion (fig. 55).

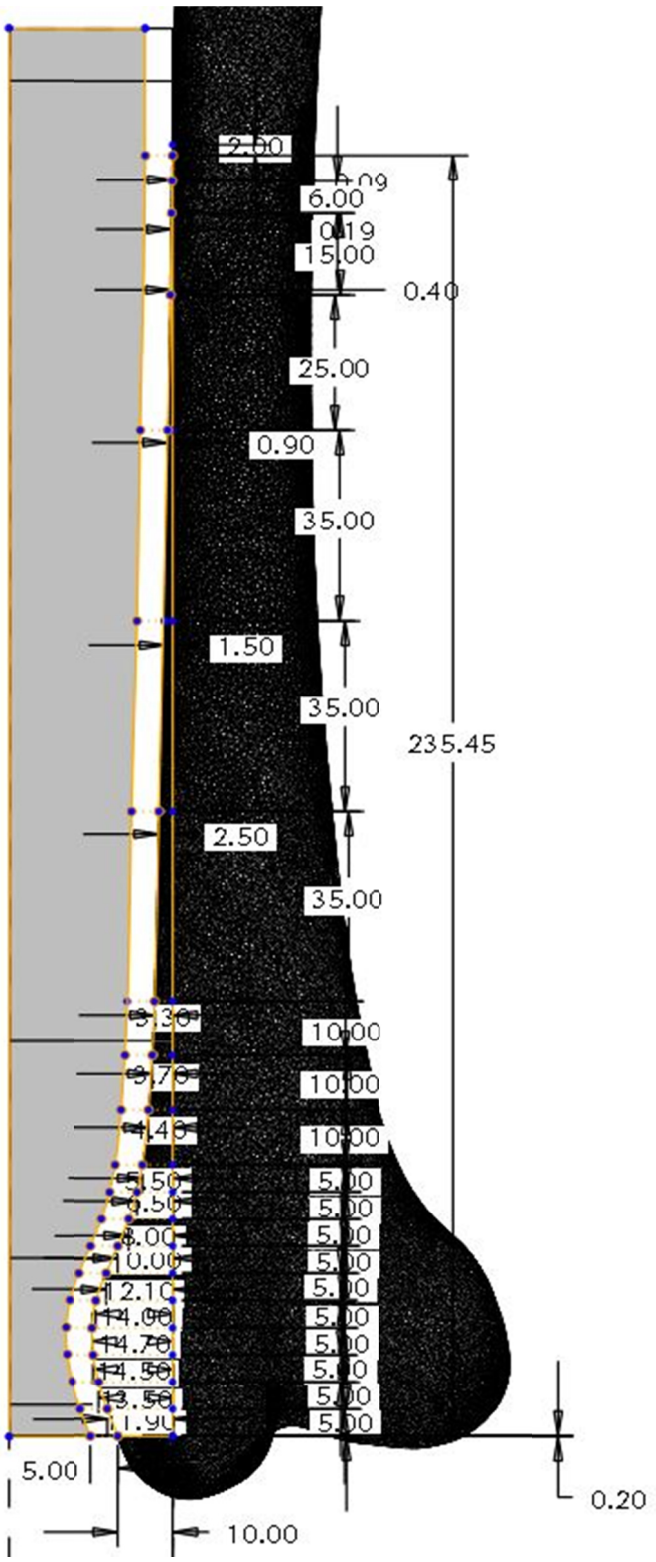

Fig. 54. Sketch of optimized anterior profile over average femur

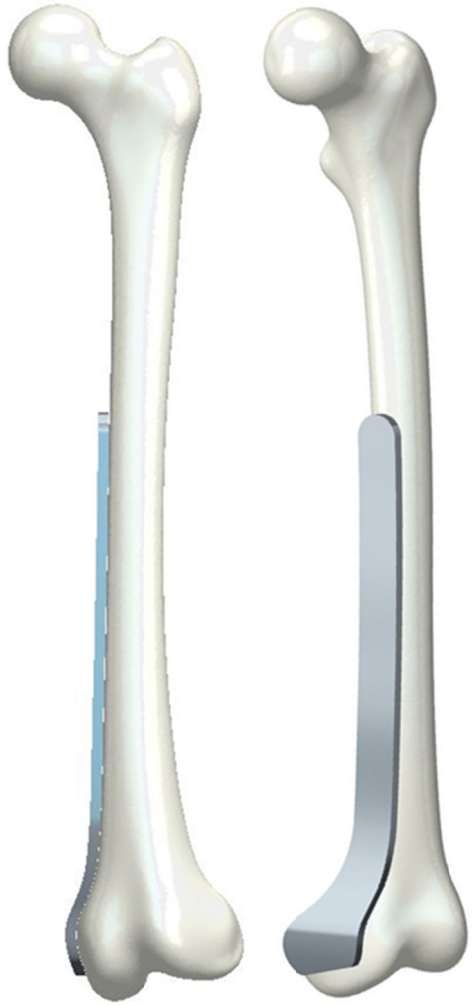

Fig. 55. Extruded cut of anterior profile

Finally, the initial locations of the threaded interlocking screw holes were sketched and extruded - removing material when intersecting the concept model - from the sagittal plane (fig. 56). A 5° draft along the plate/screw interface was also created. The initial plate geometry – optimized for fit and to be subsequently optimized for structural integrity – is shown in fig. 57.

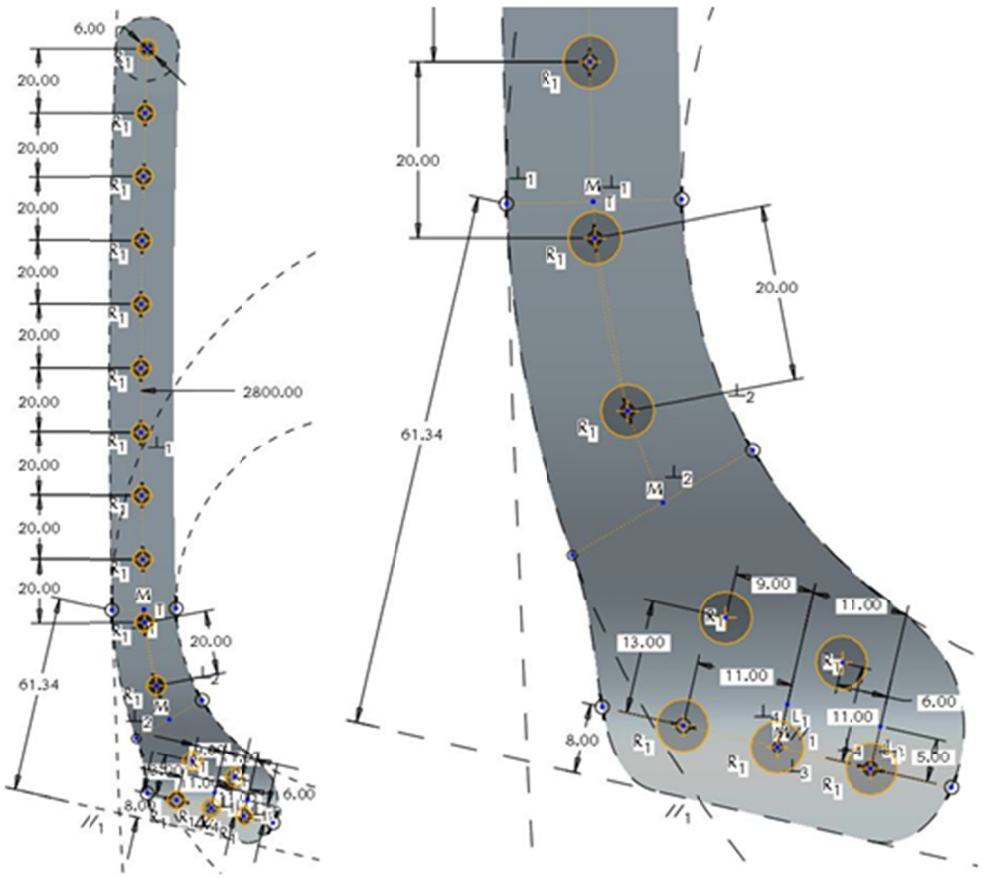

Fig. 56. Sketched hole placement for interlocking screws

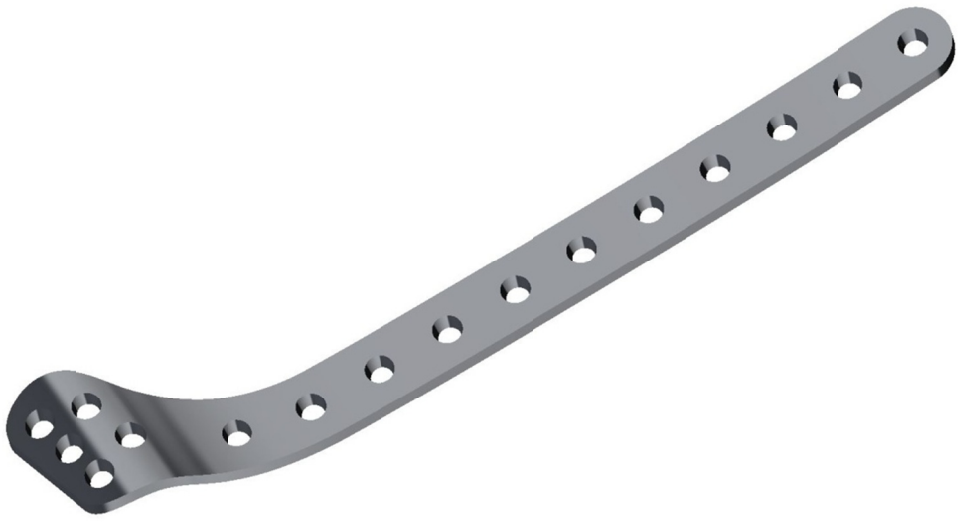

Fig. 57. Basic optimized shape to be used for simulation-based structural optimization

8. Simulation-Based Performance Analysis

Digital Reconstruction of Current Plates

The following distal femur locked plating systems, including locking screws of various lengths, were digitally reconstructed using Pro/Engineer. A 0.1 mm precision was maintained to ensure accurate geometric representation.

- DePuy POLYAX distal femur Plate (fig. 58)
- Smith & Nephew PERI-LOC distal femur locking plate (fig. 59)
- Synthes locking condylar plate (LCP) (fig. 60)
- Synthes less invasive stabilizing system (LISS) (fig. 61)
- Zimmer NCB distal femoral plating system (fig. 62)

Fig. 58. CAD model of DePuy POLYAX plate

Fig. 59. CAD model of Smith & Nephew PERI-LOC plate

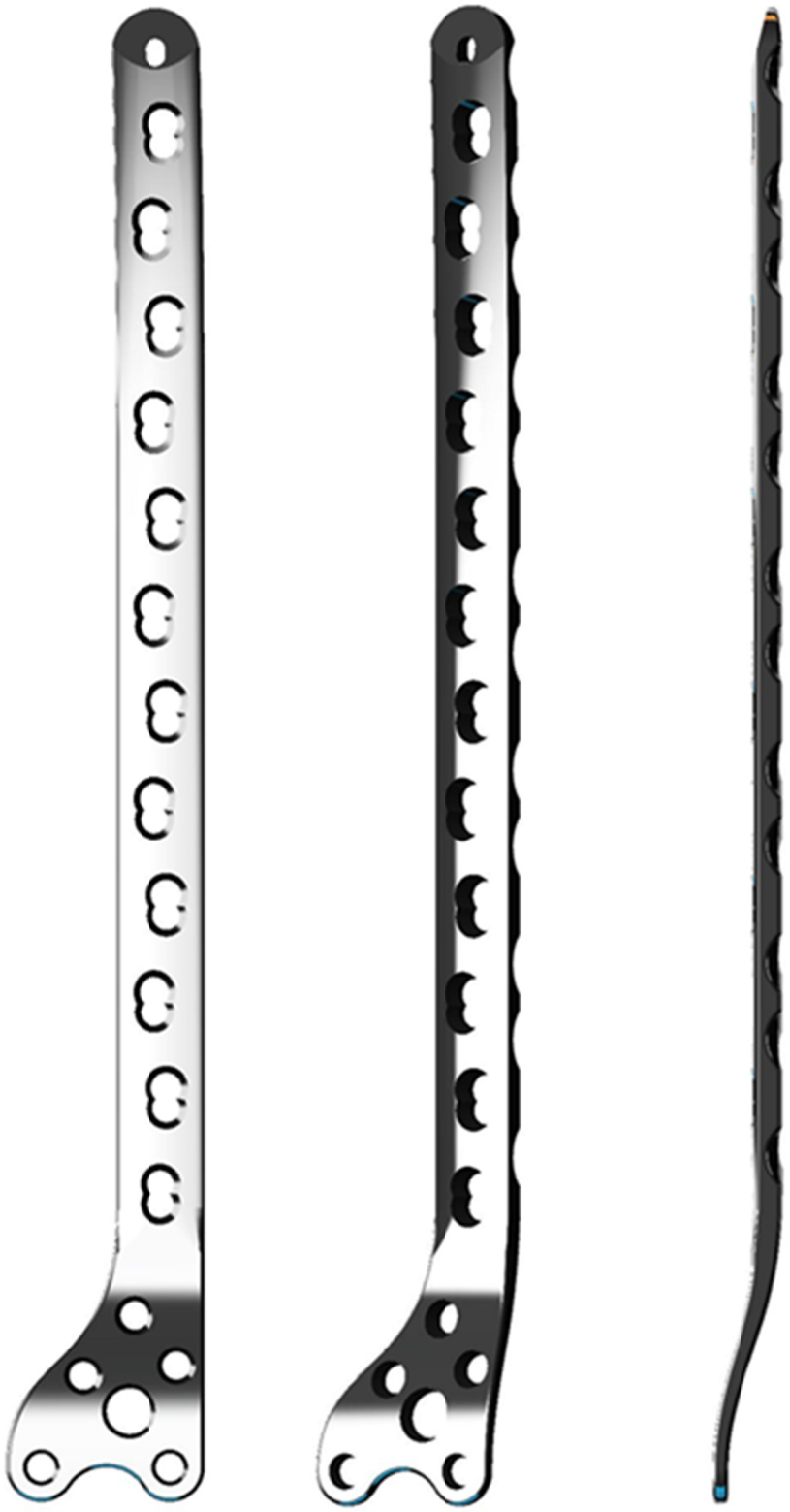

Fig. 60. CAD model of Synthes LCP

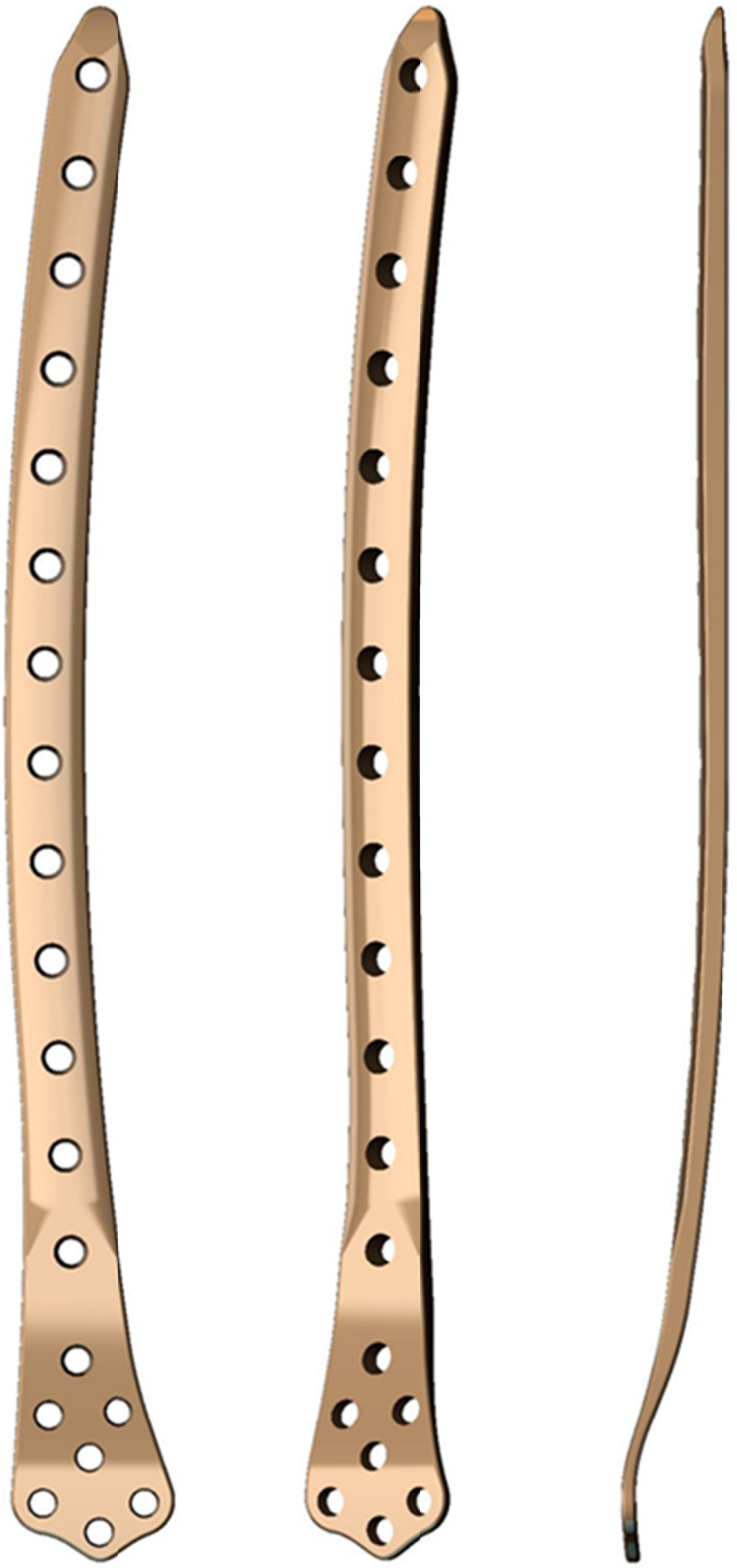

Fig. 61. CAD model of Synthes LISS

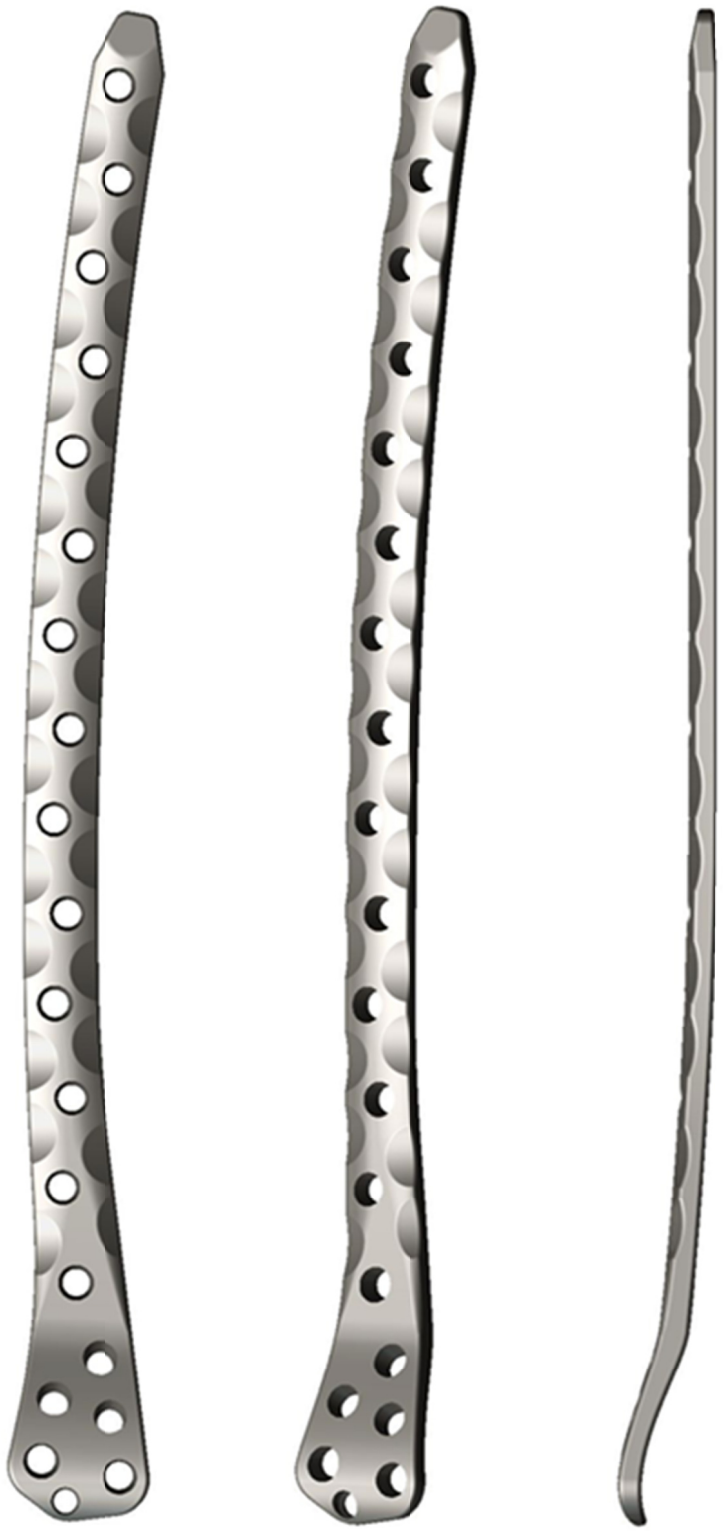

Fig. 62. CAD model of Zimmer NCB

Comparative Performance Analysis

A finite element femoral fracture model was created using Abaqus CAE (Dassault Systèmes, 2008). The flexibility of the fracture model allowed for the simulation of various fracture types, methods of fracture stabilization, and physiological loading conditions, as well as modifications to the plating systems. Cortical and cancellous bone geometry was generated from one of the femur specimen from the Cleveland Museum of Natural History. Each plate was fitted to the femur model as recommended by the corresponding technique guides provided by the manufacturers. Interlocking screws were then inserted at the appropriate locations. One to two holes adjacent to the fracture site – the number depending on the relative location of the hole – were left vacant. This allowed for an experimental control where the plate length between the nearest proximal and distal screws relative to the fracture was as close to being the same length as possible.

The screw placement elsewhere throughout the plates was not as critical to the present study. Therefore, the maximum number of course-threaded screws (used to anchor into cancellous bone) that was allowed by the femur's geometry was used in the distal condylar region. Bicortical screws were used to fixate the plate to the diaphysis; each going through the lateral side of the diaphysis with the tip anchoring in the medial side. Placement of the bicortical screws depended on whether the holes were staggered. If they weren't staggered, then every other screw hole was left vacant. If they were staggered, then screws were inserted into pairs of adjacent screw holes separated by pairs of vacant holes. This method of placement was chosen primarily to

maintain a control among the plating systems for comparative purposes, not as an optimum screw configuration technique. Once each screw was positioned, a subtractive Boolean operation was performed to "drill" the screw holes into the femur. This was accomplished by removing overlapping geometry among the femur and screws.

After inserting the screws into the desired locations, in order to simulate locking threads, tie constraints were assigned to prevent relative motion between screw/bone and screw/plate nodes in contact. The threaded interfaces were simplified as smooth cylindrical surfaces matching the inner diameters of the screw's shaft and head. The screw heads were also given a 5° draft.

Contact constraints mimicking the normal and tangential behavior of the bone/implant interface were assigned between the plate and femur. A coefficient of friction of 0.2 was chosen to mimic the behavior of tangential bone/metal sliding in a wet environment. The displacement was constrained in all three degrees of freedom for nodes located at the knee joint.

The fracture model geometry for each plating system – with two different fracture types (distal fractures with and without bone loss) – is illustrated in figures fig. 63-Fig. 67. The fractures were generated via Boolean operations by subtracting overlapping fracture geometry from the femur model. Wherever subtractive operations were performed – whether by fracture or drilling – virtual topology techniques were used to combine all faces that were modified in the process. As described in the *Methodology* section, this ensures a quality local tetrahedral mesh adjacent to the fracture/drill site.

Fig. 63. Fracture model using DePuy POLYAX plate (*far left:* fracture with bone loss, *right three:* distal transverse fracture)

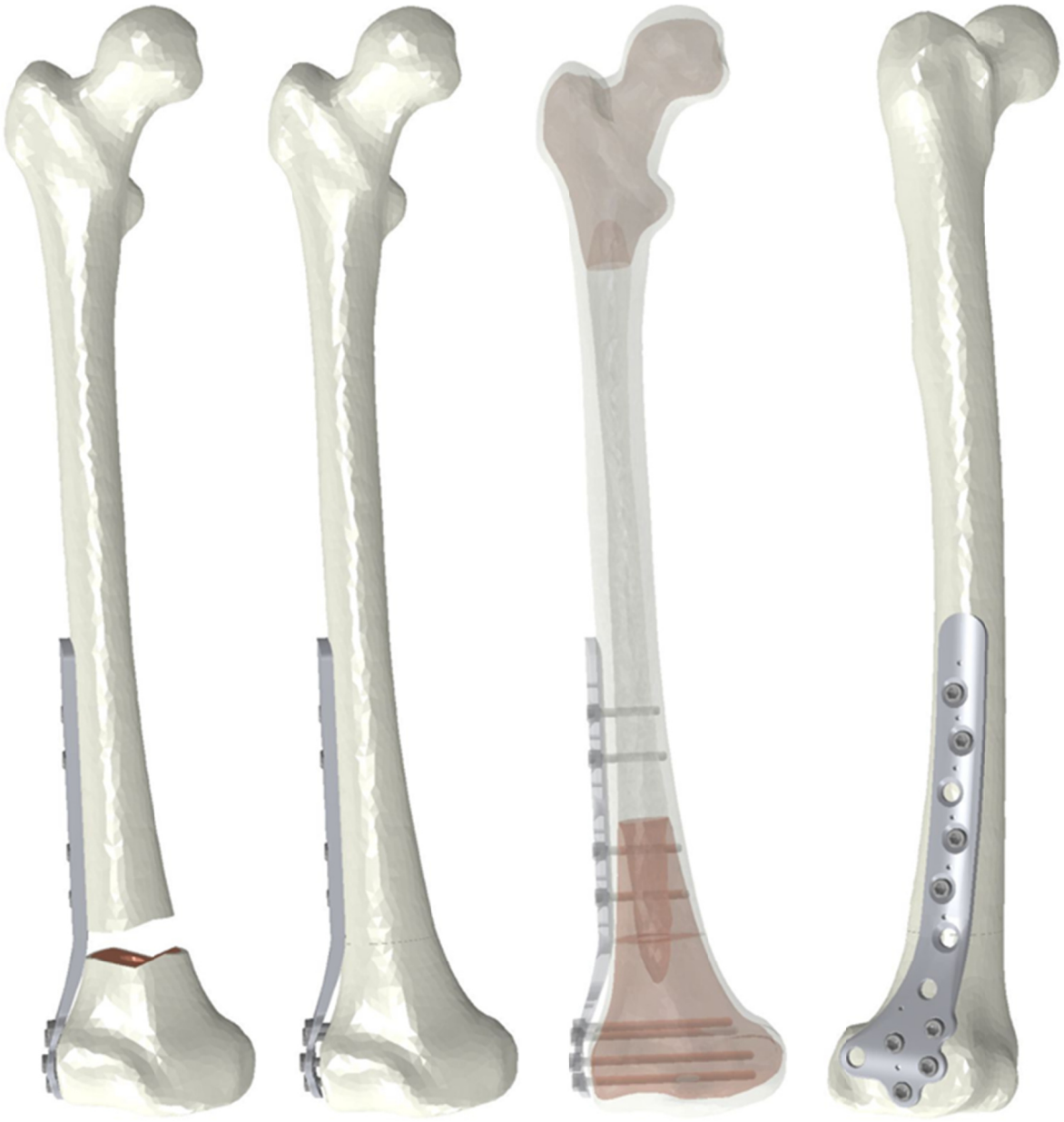

Fig. 64. Fracture model using Smith & Nephew PERI-LOC plate (*far left:* fracture with bone loss, *right three:* distal transverse fracture)

Fig. 65. Fracture model using Synthes LCP (*far left:* fracture with bone loss, *right three:* distal transverse fracture)

Fig. 66. Fracture model using Synthes LISS (*far left:* fracture with bone loss, *right three:* distal transverse fracture)

Fig. 67. Fracture model using Zimmer NCB (*far left:* fracture with bone loss, *right three:* distal transverse fracture)

A free-body diagram in fig. 68 illustrates the loading direction and the shear and normal reaction forces at the knee joint. A normal and high *q* angle, as previously discussed, were chosen for analysis. The magnitude of the hip load was determined

from the weight of an individual – in this case, 250 lbs – and whether time-dependent impulse loading was present (*i.e.* walking, jogging, stumbling, jumping, etc.).

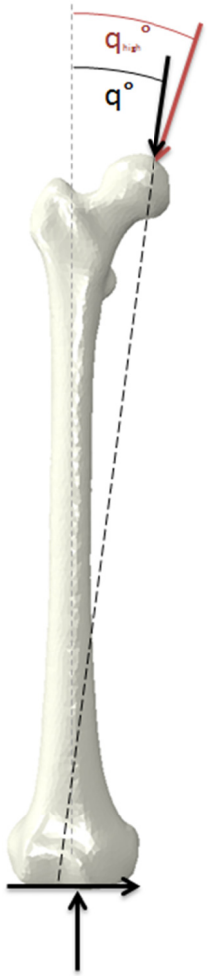

Fig. 68. Femur free body diagram showing direction of loading at hip joint as defined by *q* angle

In addition to standing with the entire weight of an individual on the treated leg, the dynamic physiological loading conditions examined in this study were experimentally measured by Bergmann, *et al.* (fig. 69-Fig. 71). These time-dependent loads represent the percent of body weight the hip joint actually experiences during walking, jogging, and stumbling. Although a patient is typically advised to keep all

weight off the injured leg during the initial weeks of recovery, it is not uncommon for the individual to attempt to stand or even walk during this time – whether intentionally or by accident. It is therefore desirable to determine the performance of the plating system under this extreme loading condition.

Nodes at the hip joint interface were selected for distributing the maximum load magnitude across the joint surface in the appropriate direction ($q°$ and $q_{high}°$). For the impulse loads, tabular amplitude functions were generated to simulate the change in hip load throughout the impact duration. During the load time step, the amplitude function, ranging from zero to one, was multiplied with the maximum load magnitude.

Muscular reaction forces were omitted for the present case studies. Various muscles act as stabilizers for the femur during hip joint loading and, therefore, have some effect on how the femur behaves structurally. However, for the present feasibility study demonstrating the effectiveness of the proposed design and optimization methodology, it is valid to ignore muscular reaction forces knowing that their presence will only reduce load-induced stresses in the femur/implant system. Experimental data will be necessary to include these elements in further analyses.

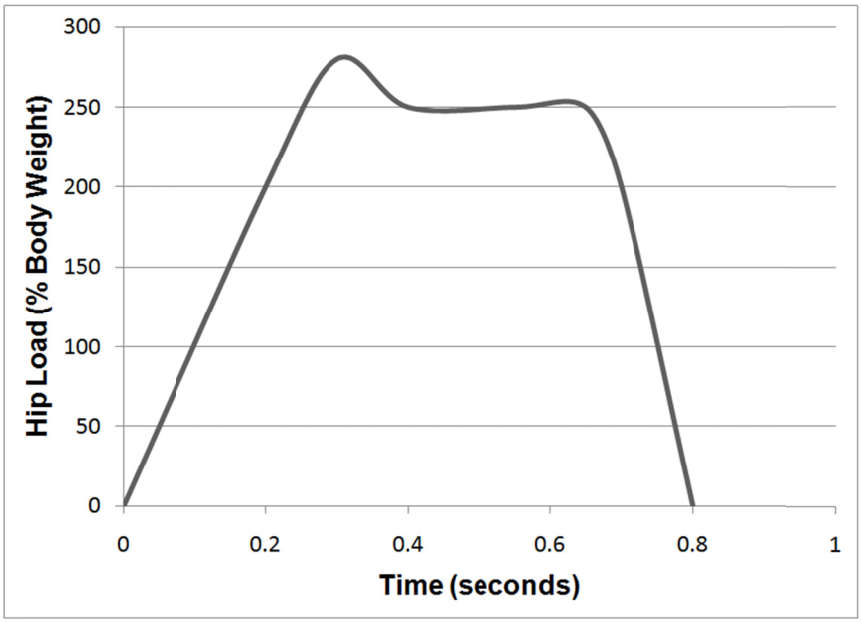

Fig. 69. Load amplitude function during walking [83]

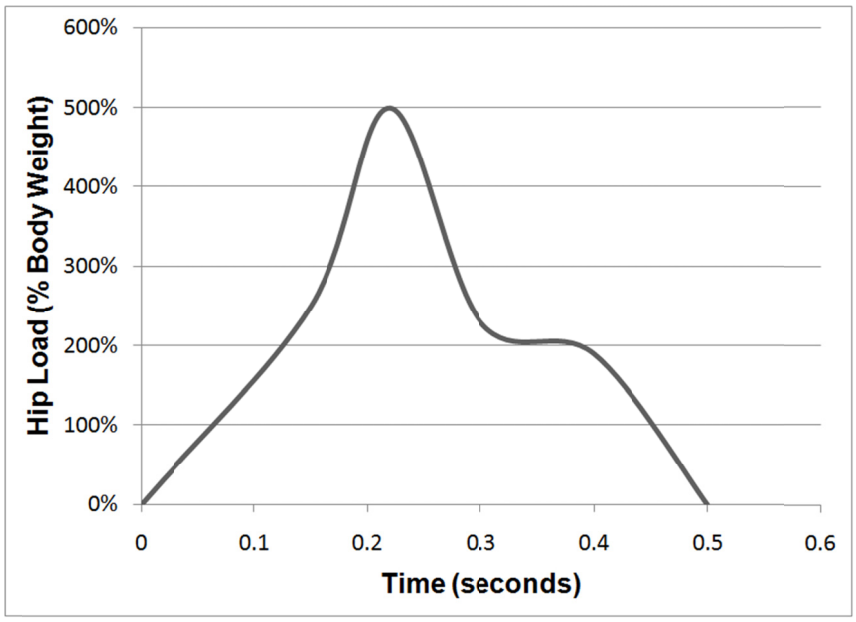

Fig. 70. Load amplitude function during jogging [83]

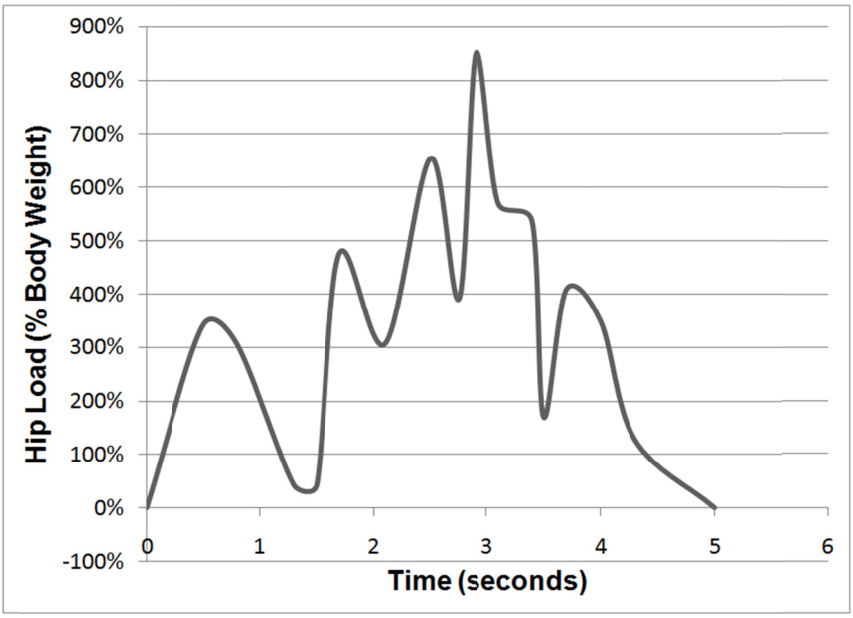

Fig. 71. Load amplitude function during stumbling [83]

A design of simulations was established in order to compare the performance of the five femoral plate systems under four physiological loading conditions and three fracture scenarios (including an intact femur representing the patient after full recovery). The four loading conditions were also simulated on an intact femur without plate fixation in order to determine the normal, or target, stress field in the femur. The design of simulations is presented in

Table 4. In addition, the 64 simulations found in the table were performed for each *q*-angle (°*q* and q_{high}°); therefore, a total of 128 scenarios were analyzed.

Table 4. Simulation scenarios

Distal Femur Locking Plate	Load Case	Fracture Type	Simul. #
None	Standing (250 lbs)	Intact	1
	Walking (700 lbs @ 0.3 s)	Intact	2
	Jogging (1,250 lbs @ 0.2 s)	Intact	3
	Stumbling (2,125 lbs @ 2.9 s)	Intact	4
Synthes LCP	Standing	Intact	5
		Distal transverse fracture	6
		" " with bone loss	7
	Walking	Intact	8
		Distal transverse fracture	9
		" " with bone loss	10
	Jogging	Intact	11
		Distal transverse fracture	12
		" " with bone loss	13
	Stumbling	Intact	14
		Distal transverse fracture	15
		" " with bone loss	16
Synthes LISS	Standing	Intact	17
		Distal transverse fracture	18
		" " with bone loss	19
	Walking	Intact	20
		Distal transverse fracture	21
		" " with bone loss	22
	Jogging	Intact	23
		Distal transverse fracture	24
		" " with bone loss	25
	Stumbling	Intact	26
		Distal transverse fracture	27
		" " with bone loss	28
Zimmer NCB	Standing	Intact	29
		Distal transverse fracture	30
		" " with bone loss	31
	Walking	Intact	32
		Distal transverse fracture	33
		" " with bone loss	34
	Jogging	Intact	35
		Distal transverse fracture	36
		" " with bone loss	37
	Stumbling	Intact	38
		Distal transverse fracture	39
		" " with bone loss	40
Smith & Nephew PERI-LOC	Standing	Intact	41
		Distal transverse fracture	42
		" " with bone loss	43
	Walking	Intact	44
		Distal transverse fracture	45
		" " with bone loss	46
	Jogging	Intact	47
		Distal transverse fracture	48
		" " with bone loss	49
	Stumbling	Intact	50
		Distal transverse fracture	51
		" " with bone loss	52
DePuy POLYAX	Standing	Intact	53
		Distal transverse fracture	54
		" " with bone loss	55
	Walking	Intact	56
		Distal transverse fracture	57
		" " with bone loss	58
	Jogging	Intact	59
		Distal transverse fracture	60
		" " with bone loss	61
	Stumbling	Intact	62
		Distal transverse fracture	63
		" " with bone loss	64

The analysis steps for each simulation were defined as static. For the impulsive "dynamic" loading conditions, the experimental data provided by Bergmann, *et al*, could be simulated as quasi-static – a change in hip load as a function of time. Non-linear large deformations were assumed.

Solid meshing was achieved using approximately two million linear tetrahedral elements for each fracture model. Through preliminary simulations using h-adaptivity convergence, the element size was reduced with an average edge length of 0.5 mm for the plate systems and 2.0 mm for the femur (fig. 72) in order to ensure that the solution was mesh independent. Once the input files for each simulation were generated, most of the processing was accomplished via remote access to a supercomputer at the National Center for Supercomputing Applications (NCSA), located at the University of Illinois. Eventually, a high-performance 64-bit personal computer with eight processing threads, 24 GB of memory, and a solid state scratch drive was built to alleviate the wait time required to run the analyses and download the large output files.

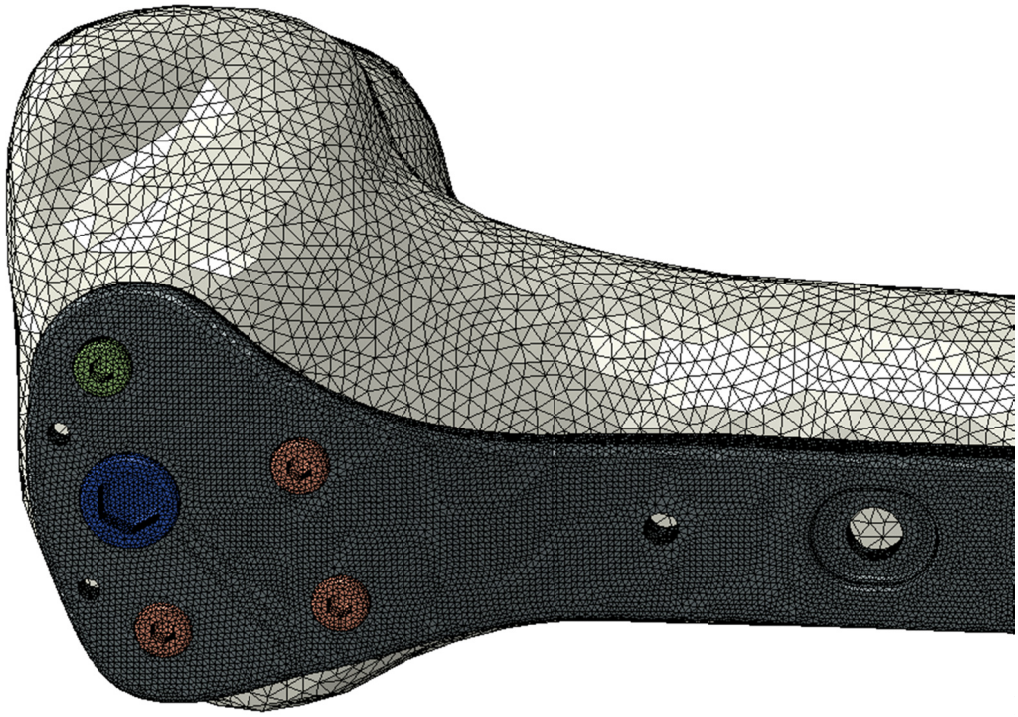

Fig. 72. Tetrahedral mesh of intact femur fixated with DePuy POLYAX plate system

One of the two results of interest in the comparative performance analysis is the factor of safety for each plate. The factor of safety is a performance measure found by dividing the material yield strength by the maximum stress. The Smith & Nephew PERI-LOC and Synthes LCP systems are manufactured from medical grade stainless steel. The remaining plate systems are of medical grade titanium alloy. The anisotropic material properties of the corresponding materials were assigned to the appropriate plate system as previously described.

The other result of interest is the stress distribution in the femur. Ideally, after full recovery the femur should behave as it would without the plating system present. The results are intended to quantify the effects each plate has on the overall biomechanics of the femur and on stress shielding.

9. Structural Optimization

Parametric Analysis

The Smith & Nephew PERI-LOC fracture model with a distal transverse fracture was chosen to perform the parametric analysis. Stress concentrations are found around empty screw holes in the plate, particularly near the fracture; therefore, screw hole inserts were also created for the fracture model. The use of inserts may reduce the stress in these locations. Additionally, using an interlocking oblique screw angled 45° distally through the fracture – in the coronal plane – may provide increased stability. Although current plates do not allow for such large angle oblique screws with interlocking capabilities, a screw model was modified to allow the technique to be simulated and quantify its potential. Fig. 73 illustrates the fracture model assembly configuration with screw hole inserts and oblique screw.

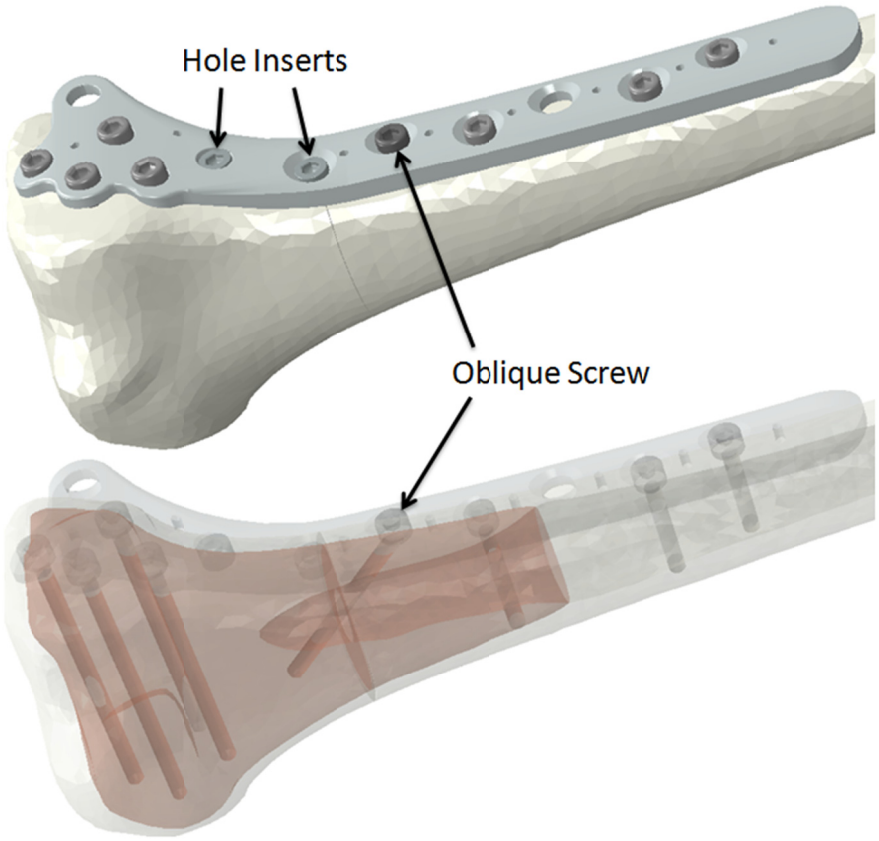

Fig. 73. Fracture model with screw hole inserts and oblique screw

The investigated factors and their alternate levels are presented in Table 5. Plate material, thickness, use of screw hole inserts, and use of oblique screws comprise an L_9, Taguchi orthogonal array [84]. The array defines the nine simulation conditions needed for a parametric analysis of the locked plating systems (see Table 6), in contrast to simulating every possible parameter combination. The factor of safety associated with each design was chosen as the design performance (response) in each of the planned simulations. Each of the simulations outlined in Table 6 were performed using a hip load equivalent in magnitude to the impact of a 250 lb individual taking one step during walking. Details concerning the loading and boundary conditions, interactions, material

properties, meshing, time step, and solver properties were identical to those of the comparative performance analysis.

Table 5. Factors and their alternate levels

Factors	Number of Levels		
	1	2	3
A. Material (Type)	Type 1	Type 2	Type 3
B. Thickness	3.5 mm	4.5 mm	5.5 mm
C. Use of screw hole inserts	With	Without	With (dummy)
D. Use of oblique screw (45°)	With	Without	With (dummy)

Table 6. Simulation log for parametric analysis

Simul. No.	Material	Thickness (mm)	Screw Hole Inserts	Oblique Screw (45°)
1	316L SS	3.5	Yes	Yes
2	316L SS	4.5	No	No
3	316L SS	5.5	Yes	Yes
4	Ti6Al7Nb	3.5	No	Yes
5	Ti6Al7Nb	4.5	Yes	Yes
6	Ti6Al7Nb	5.5	Yes	No
7	CFR-PEEK	3.5	Yes	No
8	CFR-PEEK	4.5	Yes	Yes
9	CFR-PEEK	5.5	No	Yes

Surgical grade metallic alloys such as 316L stainless steel and titanium Ti6Al7Nb are commonly used to fabricate orthopaedic implants, including locked plating systems. These alloys have traditionally been used because of their biologically inert properties and because of their high resistance to corrosion. The 316L SS and Ti6Al7Nb alloys were therefore both chosen as two of the materials in the parametric study.

Polymer composites are also of interest for fabricating plating systems due to their potential in having mechanical properties that more closely match cortical bone. This is important because a significant mismatch in implant/bone stiffness can cause local bone atrophy due to stress shielding, a phenomenon in which bone tissue remodels so that strains return to normal [73,116,117]. Carbon fiber-reinforced polyetheretherketone (CFR-PEEK) is a biocompatible, biologically inert composite designed for non-degradable implants that can be tailored to match the mechanical properties of cortical bone. CFR-PEEK also has good wear resistant properties [118] and is stable at high temperatures allowing it to endure repeated sterilization cycles [119]. Because of its potential, CFR-PEEK was chosen as the third material for the study.

FEM-Integrated Optimization

The objective of the FEM-integrated structural optimization phase was to minimize the mass of the initial plate geometry obtained through shape optimization. However, the major design constraint limiting mass minimization was the yield strength of the plate. The material properties of titanium alloy Ti6Al7Nb were used define the behavior of the plate resulting in a yield strength of 880 MPa. However, a factor of safety of 2.0 (because of long-term cyclic loading and the nature of the device) and a 20% strength degradation due to aging were assumed. Therefore, the maximum stress under normal physiological loading was set at 350 MPa.

The variable design parameters were the width and thickness of the plate. An additional design constraint was a minimum thickness of 2.5 mm. This was established

in order to insure that sufficient surface area was present at the screw/plate interfaces for interlocking to occur.

First, a pseudo-static analysis – simulating the impact at the hip joint due to a 250 lb individual stumbling – was pre-processed using an intact femur fixated with the plate obtained from the shape optimization phase. The thickness and width dimensions of the plate were overdesigned to insure that the results of the initial static analysis satisfied the allowable stress constraint ($\sigma_{max} \leq 350$ MPa). The structural analysis was then imbedded into an sequential quadratic programming (SQT) optimization algorithm where, based on the results of the preceding structural analysis, the design parameters were updated before repeating the simulation.

The static analysis and optimization algorithm were both developed in Pro/Mechanica because of it integrative capabilities. Because Pro/Mechanica uses an automated mesh generator with p-element convergence to insure mesh independence at each optimization pass, a simplified femur model was developed in order to decrease processing time. This allowed for larger element edge lengths as opposed to the femur models generated directly from the CT scans – when consisted of triangular-meshed surfaces with small edge lengths. The simplified femur model was developed using CAD sweeping techniques to match the geometry of the average femur model as illustrated in fig. 74. Because the femoral diaphysis is comprised almost entirely of cortical bone, and since the since the interaction between the plate in at femur is most significant within the diaphysis, the simplified femur model in its entirety was assumed to be

cortical bone (fig. 75). An illustration of the fracture model showing the initial dimensions of the plate is shown in fig. 76

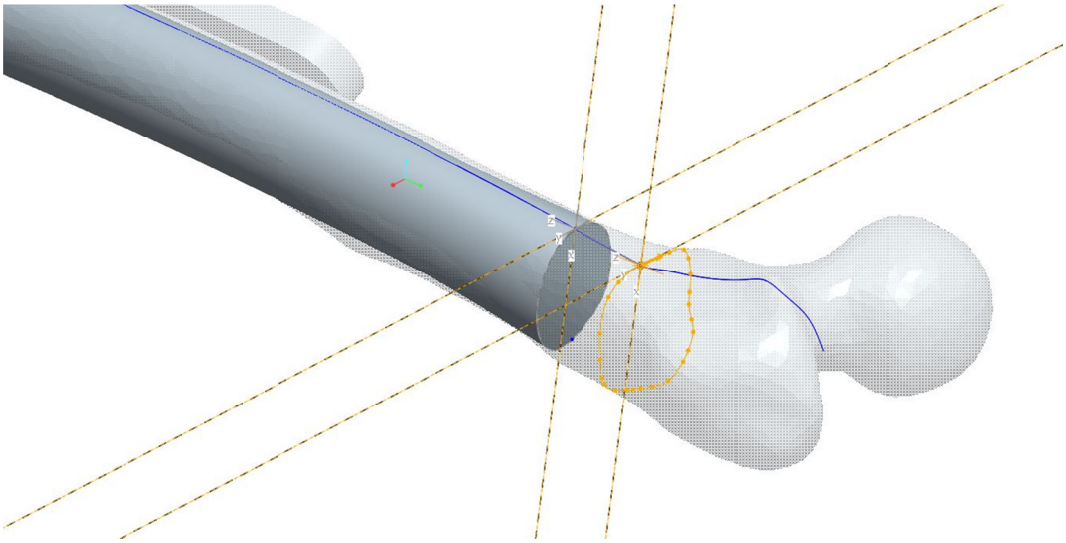

Fig. 74. Sketches of sweep path and cross sections used to construct CAD femur model for structural optimization

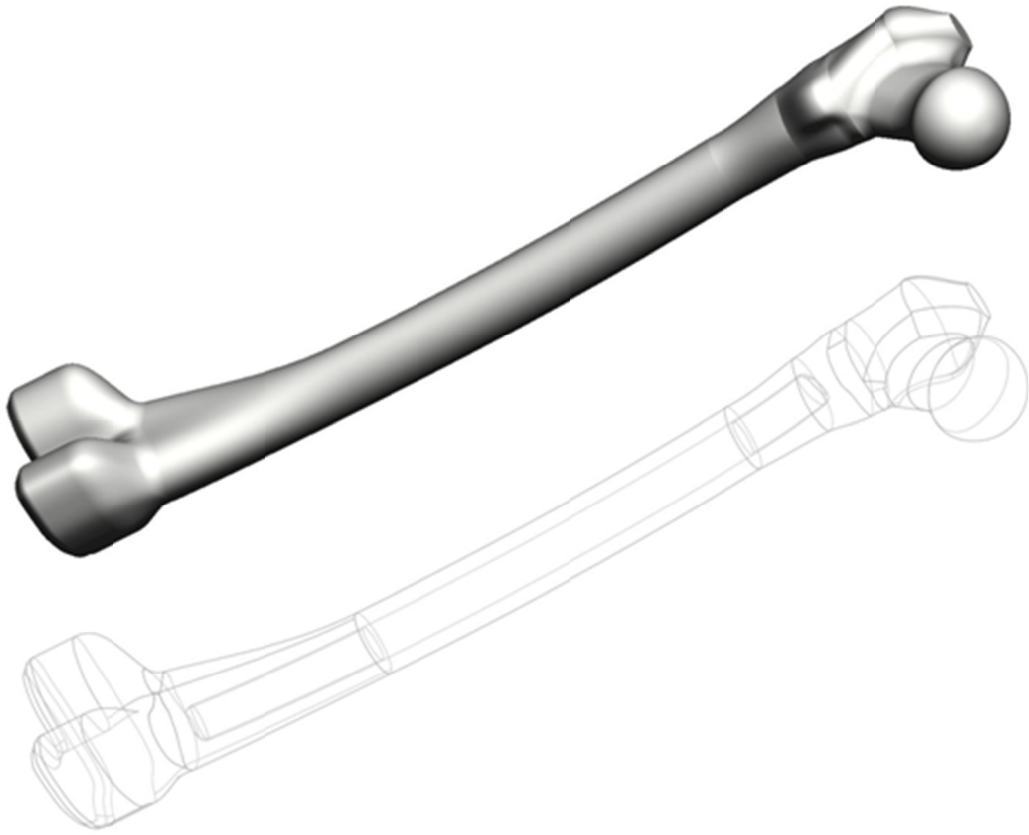

Fig. 75. Femur model used for structural optimization

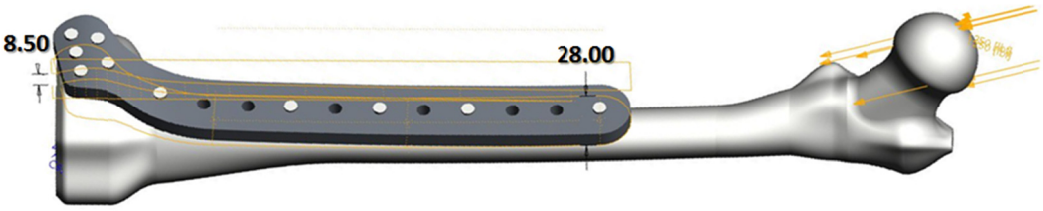

Fig. 76. Structural optimization fracture model with over-designed initial dimensions of medial locking plate

10. Experimental Verification

Experimental testing was carried out in order to verify that the results of the finite-element simulations represent what occurs in reality. Using a Sawbones composite femur and a Synthes LISS, the following for tests were performed on an MTS

universal testing machine (fig. 77 and fig. 78). The femur fixture described in the previous chapter was used to secure the femur in the testing machine. Lateral sliding of the knee joint, which would occur during loading because of lateral bending, was permitted by adjusting, the degrees of freedom of the distal fixture.

1. Intact femur without plate fixation (fig. 78-Fig. 80)
2. Intact femur with plate fixation (fig. 81 and Fig. 82)
3. Femur with distal transverse fracture and plate fixation (fig. 83)
4. Femur with distal fracture with bone loss and plate fixation (fig. 84)

For each test, compressive loading was applied to the hip joint – at a constant velocity of 0.01 in/s – while a 10,000 lb load cell recorded the axial force. Strain gauge rosettes were adhered to the lateral and medial distal diaphysis (fig. 79 and fig. 80) and on the plate (fig. 82) to measure strain in the longitudinal, tangential, and 45° directions.

Fig. 77. Experimental setup of MTS Universal Testing Machine

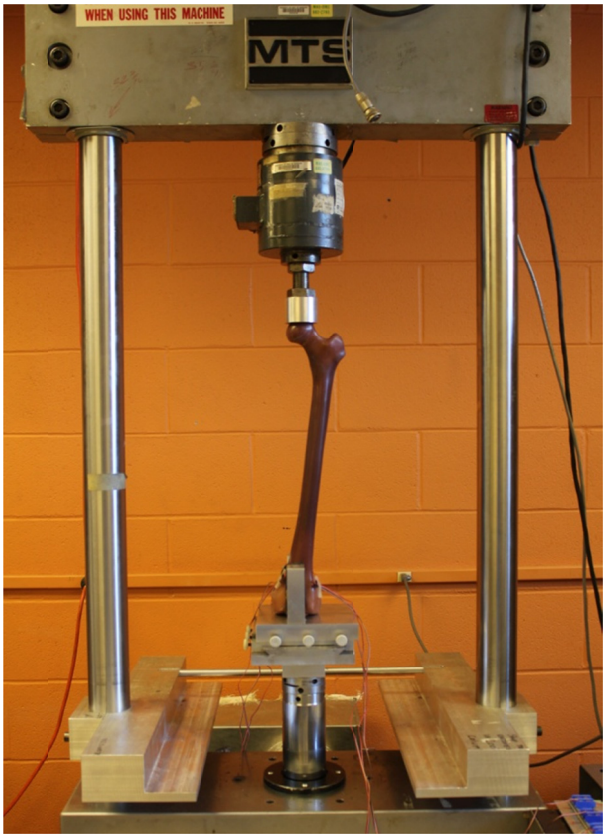

Fig. 78. Compression testing of intact femur using MTS Universal Testing Machine

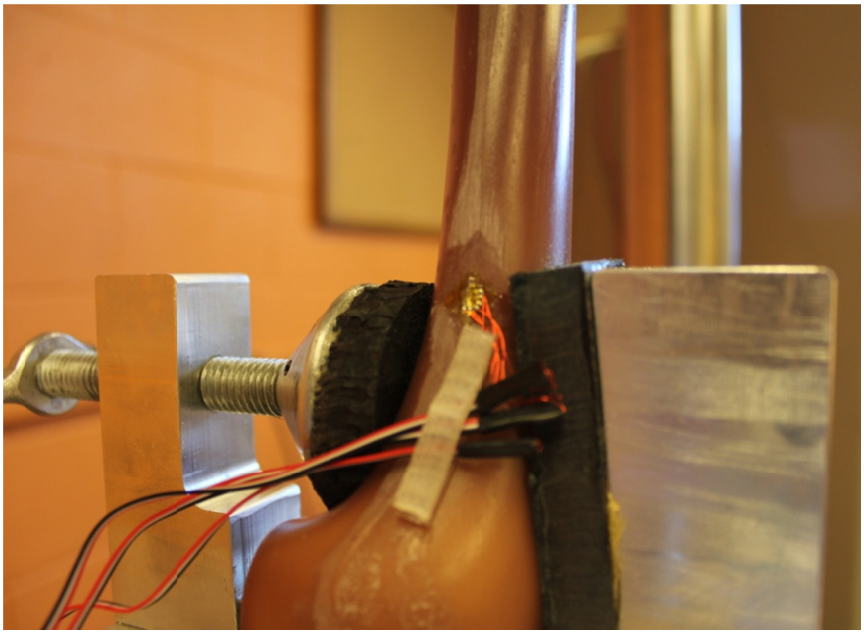

Fig. 79. Three-directional strain gauge rosette placed at medial/distal diaphysis of intact femur

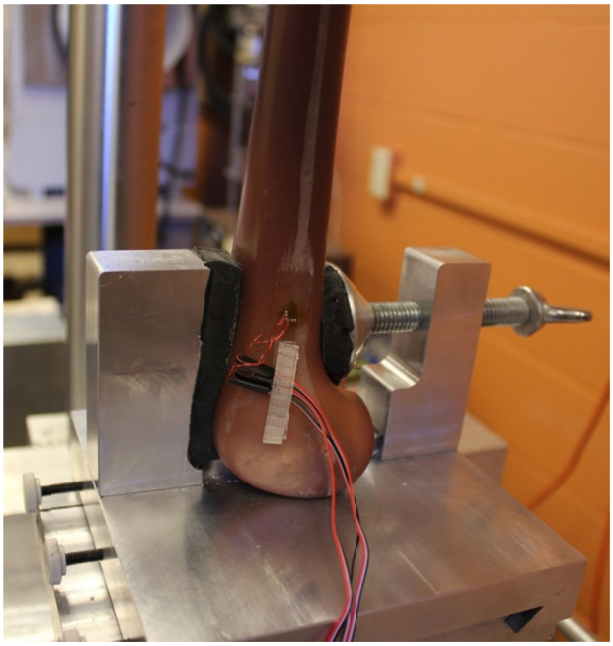

Fig. 80. Three-directional strain gauge rosette placed at lateral/distal diaphysis of intact femur

Fig. 81. Experimental testing of intact femur fixated with Synthes LISS

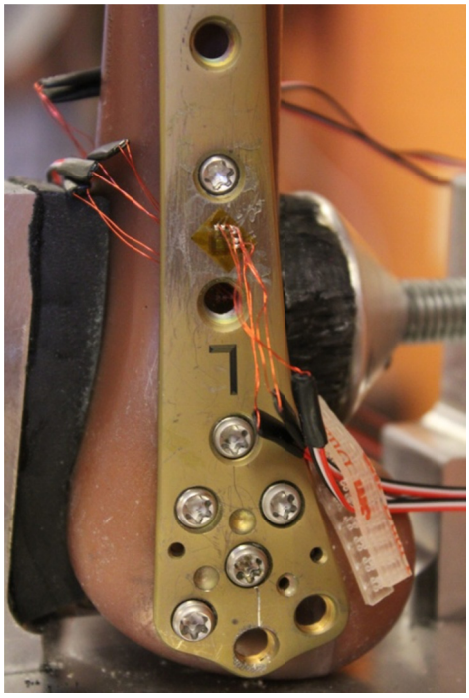

Fig. 82. Three-directional strain gauge rosette placed on distal end of Synthes LISS fixated to intact femur

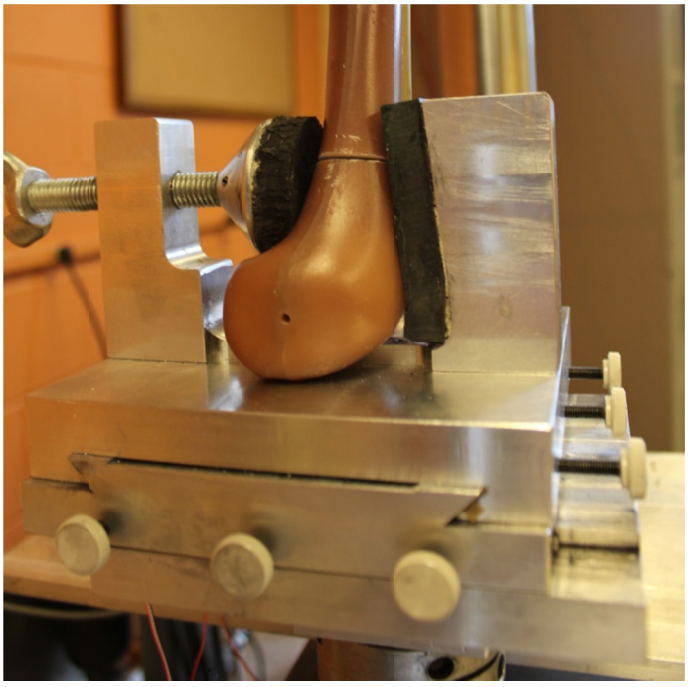

Fig. 83. Experimental testing of femur with distal transverse fracture fixated with Synthes LISS

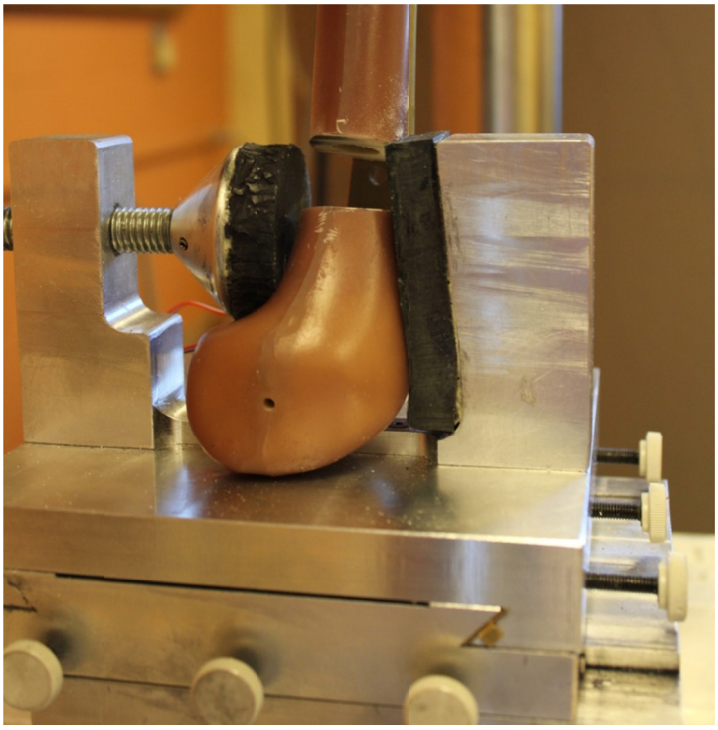

Fig. 84. Experimental testing of femur with distal fracture with bone loss fixated with Synthes LISS

Results

Comparative Performance Analysis

Simulation results from the comparative performance analysis are illustrated and compared in fig. 85-Fig. 90. These results represent normal *q*-angle loading only (where medial bending of the femur occurred); results for high *q*-angle loading – where lateral bending of the femur occurred – are presented and compared to the structurally optimized medial locking plate in the corresponding *Results* section.

The DePuy POLYAX plating system had the highest factor of safety when fixated to the intact femur for all load cases. For the femur with the distal transverse fracture, the Synthes LISS had the highest safety factor for all load cases. However, for the fractured femur with bone loss – where no bone void filler was present – mechanical

failure was predicted for all of the plating systems regardless of which loading condition was simulated. The two stainless steel plates – the Synthes LCP and Smith & Nephew PERI-LOC – had the lowest factor of safety for all loading and fracture scenarios.

Stress concentrations were present near vacant screw holes. For the intact femur, the highest stress was found in the proximal region fixated to the diaphysis. With femoral fractures introduced to the models, the maximum plate stress occurred along the fracture site. When bone loss was present, failure was predicted for all simulation cases. More details regarding the simulation results are found in Table 14 and Table 15 in Appendix A.

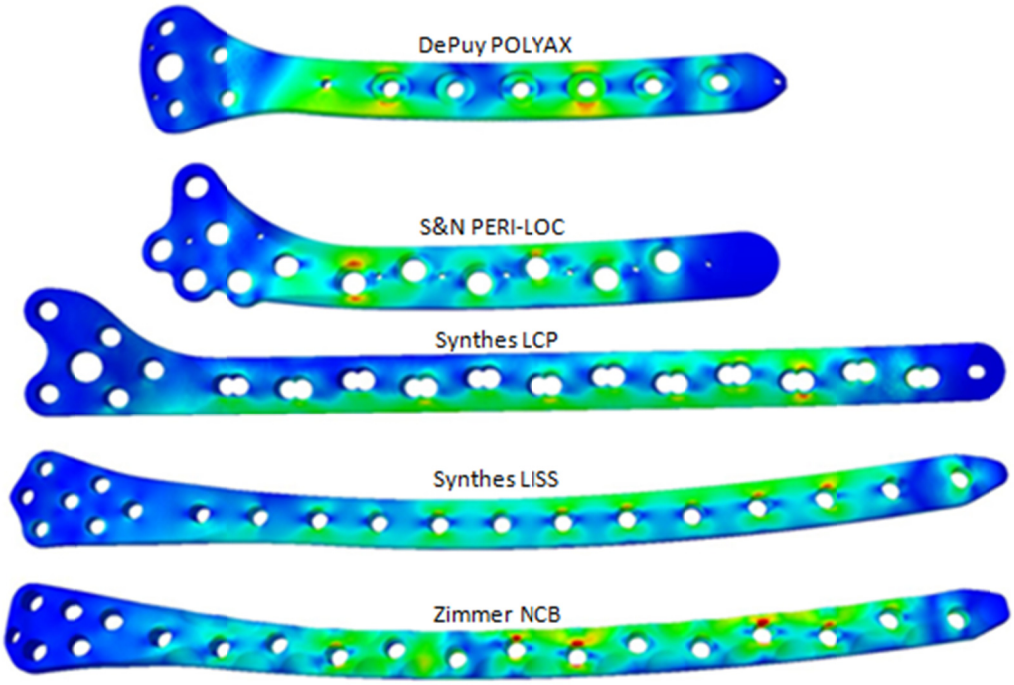

Fig. 85. Stress field for each plate fixated to loaded (normal *q*-angle) intact femur (not shown) showing areas of stress concentration in yellow/red (each plate having its own stress field scale)

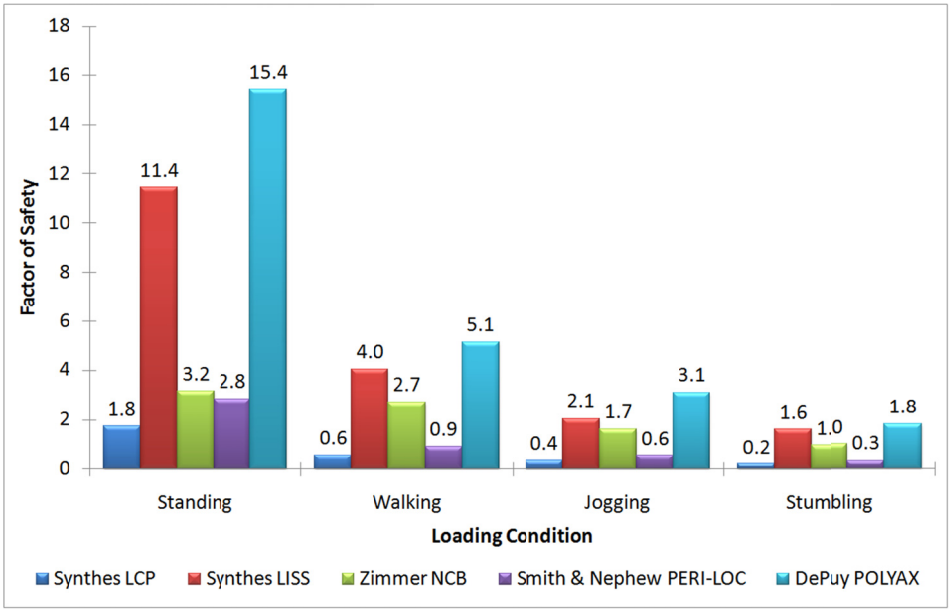

Fig. 86. FEA results of intact femur fixated with distal locking plates

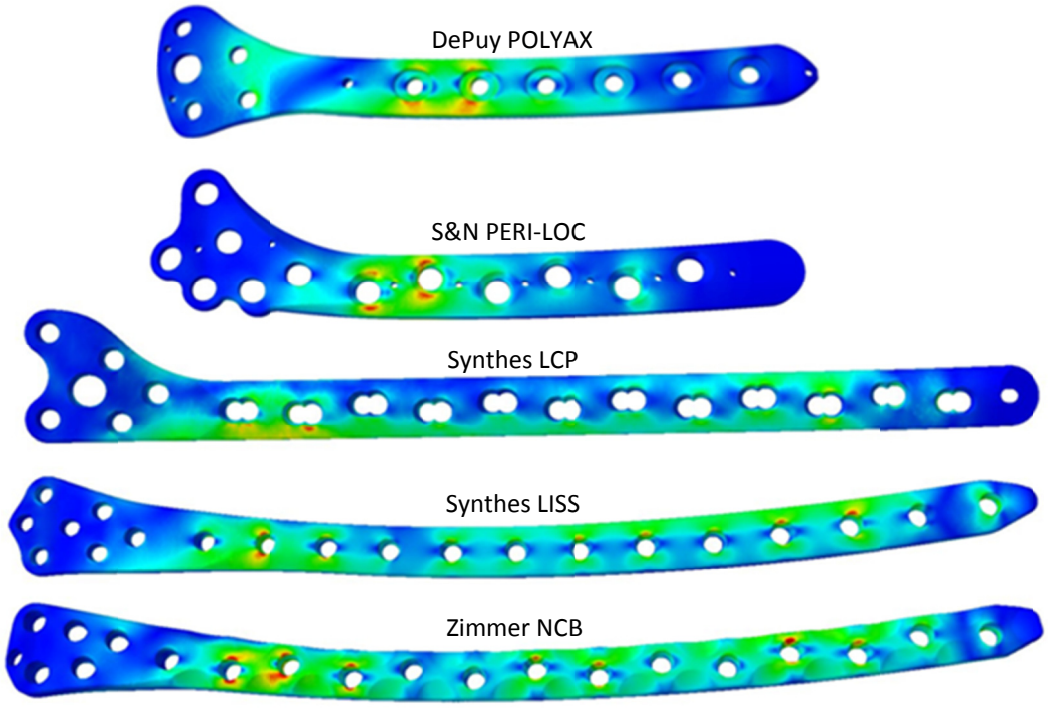

Fig. 87. Stress field for each plate fixated to loaded (normal *q*-angle) fractured femur (not shown) showing areas of stress concentration in yellow/red (each plate having its own stress field scale)

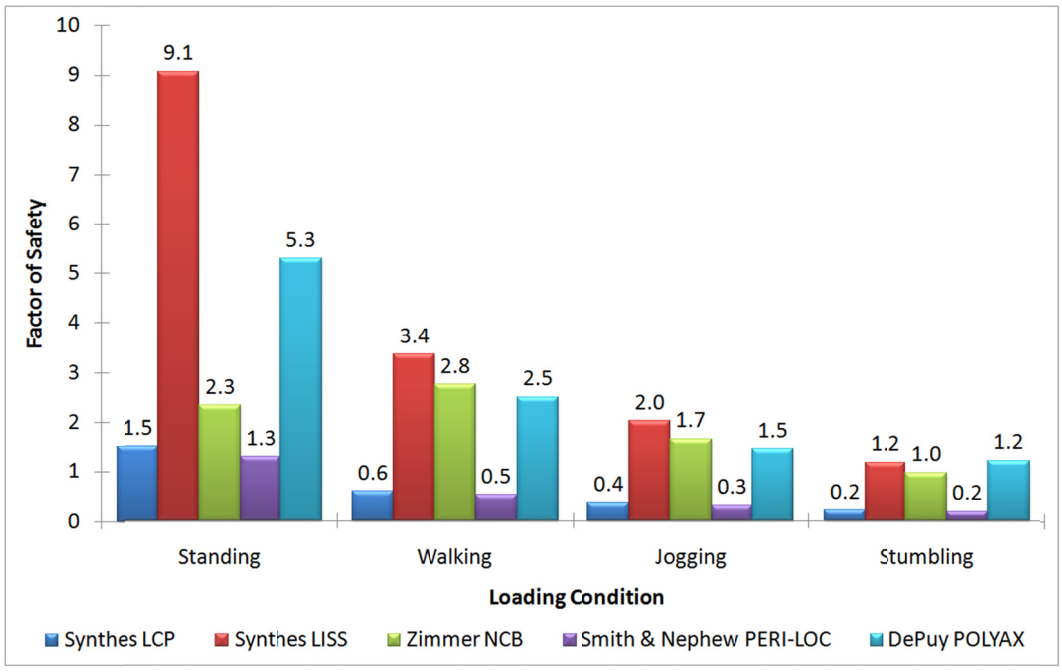

Fig. 88. FEA results of fractured femur fixated with distal locking plates

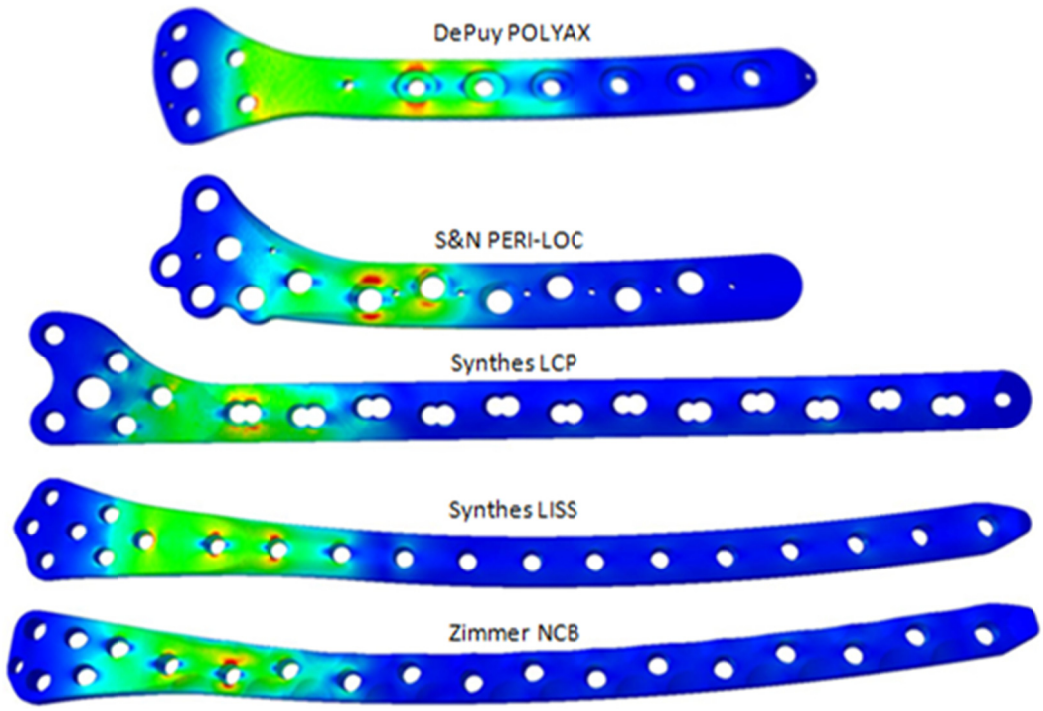

Fig. 89. Stress field for each plate fixated to loaded (normal *q*-angle) fractured femur with bone loss (not shown) showing areas of stress concentration in yellow/red (each plate having its own stress field scale)

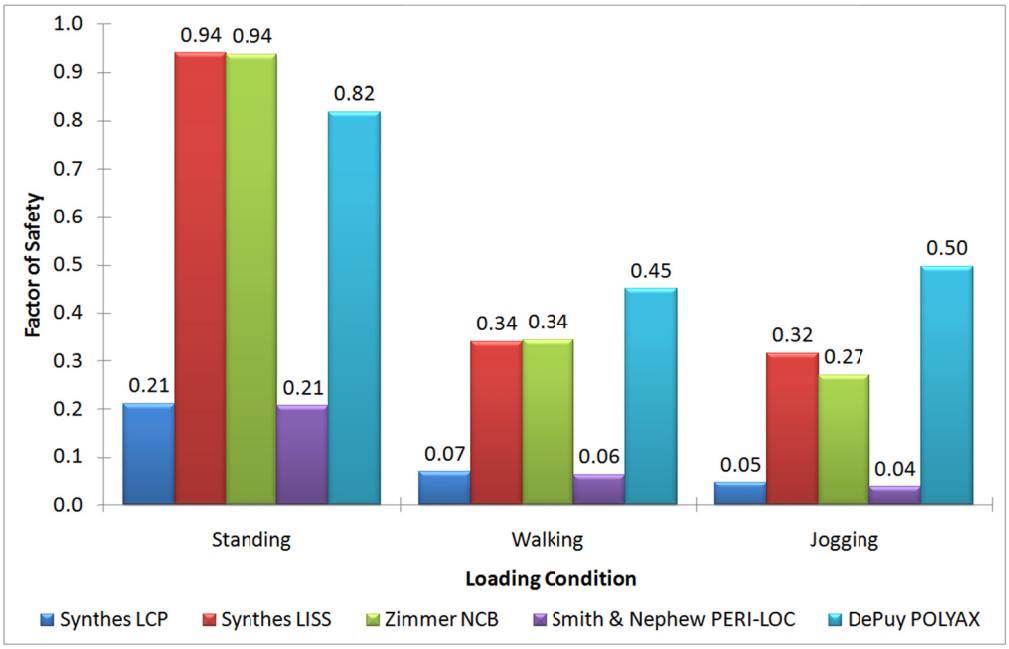

Fig. 90. FEA results of fractured femur with bone loss fixated with distal locking plates

Fig. 91-Fig. 94 illustrate how each of the plate systems affect the biomechanics of the femur by comparing the standing-induced femoral stress fields to that of a femur without plate fixation. In particular, the effects of stress shielding can be observed. It is apparent that throughout the length of plate/diaphysis interface, the femoral stress is significantly reduced compared to a healthy untreated femur. The same is true for the medial side of the diaphysis as well, particularly for the longer plates (Synthes LCP, LISS, and Zimmer NCB).

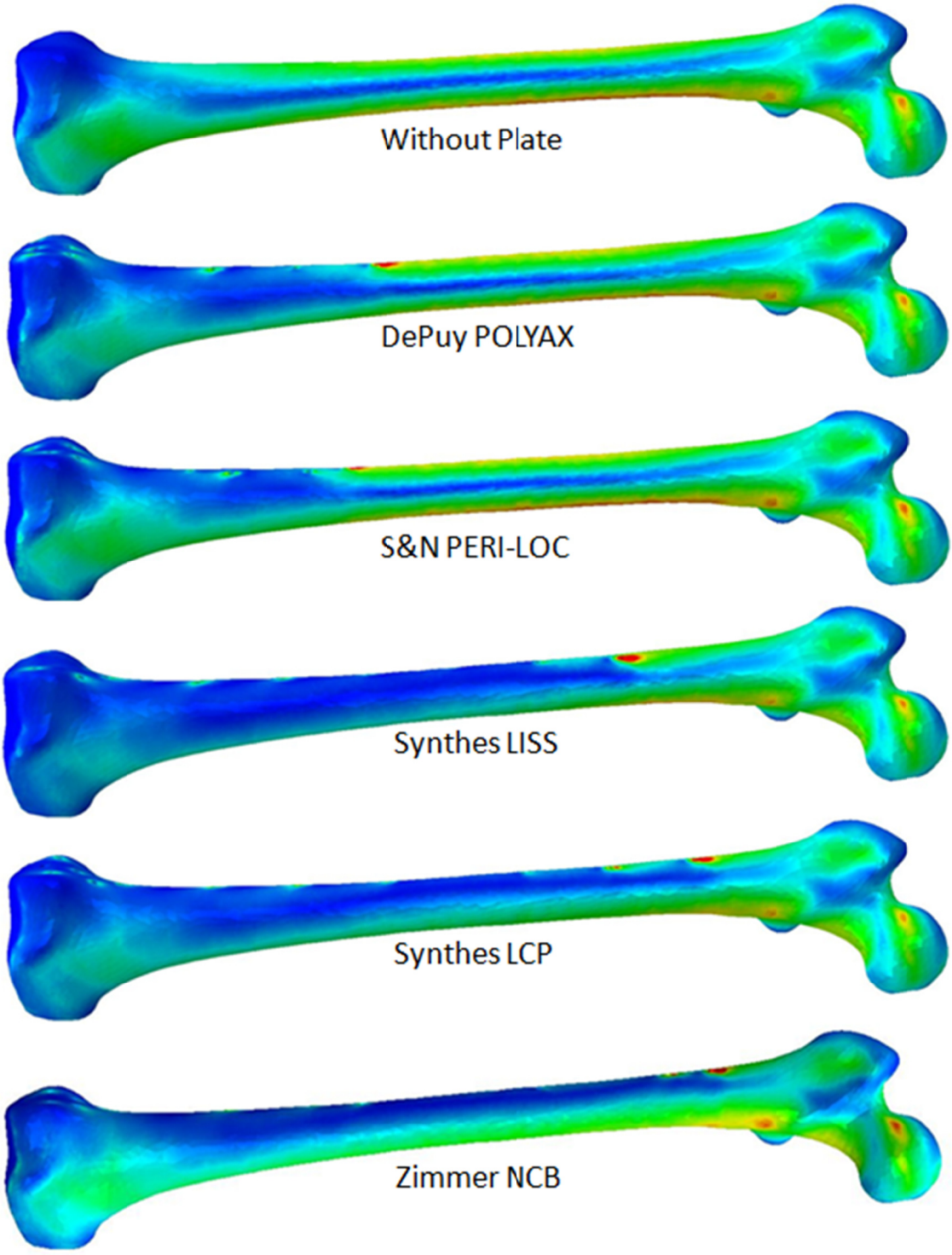

Fig. 91. FEA results illustrating the stress shielding effects of each plate (anterior view)

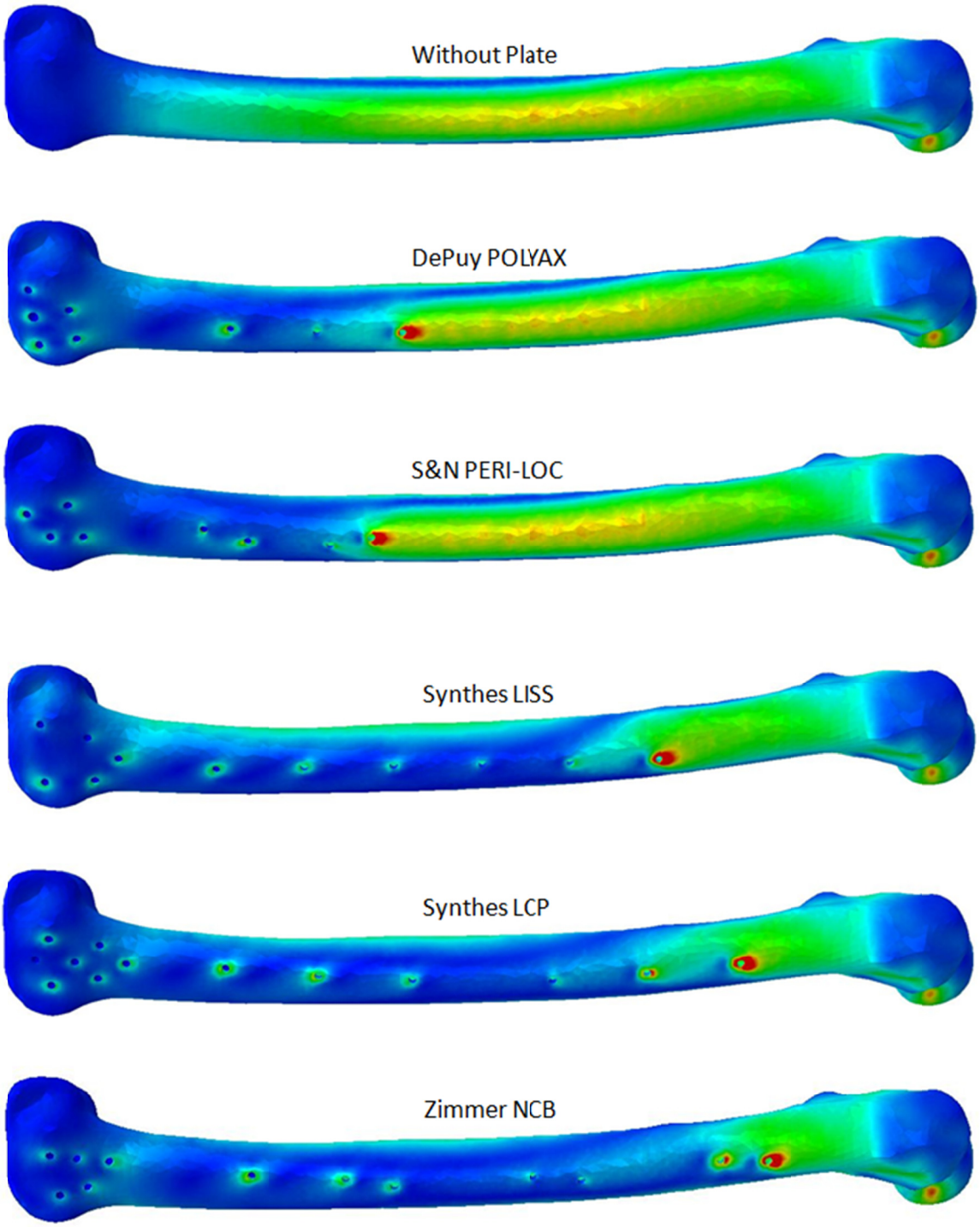

Fig. 92. FEA results illustrating the stress shielding effects of each plate (lateral view)

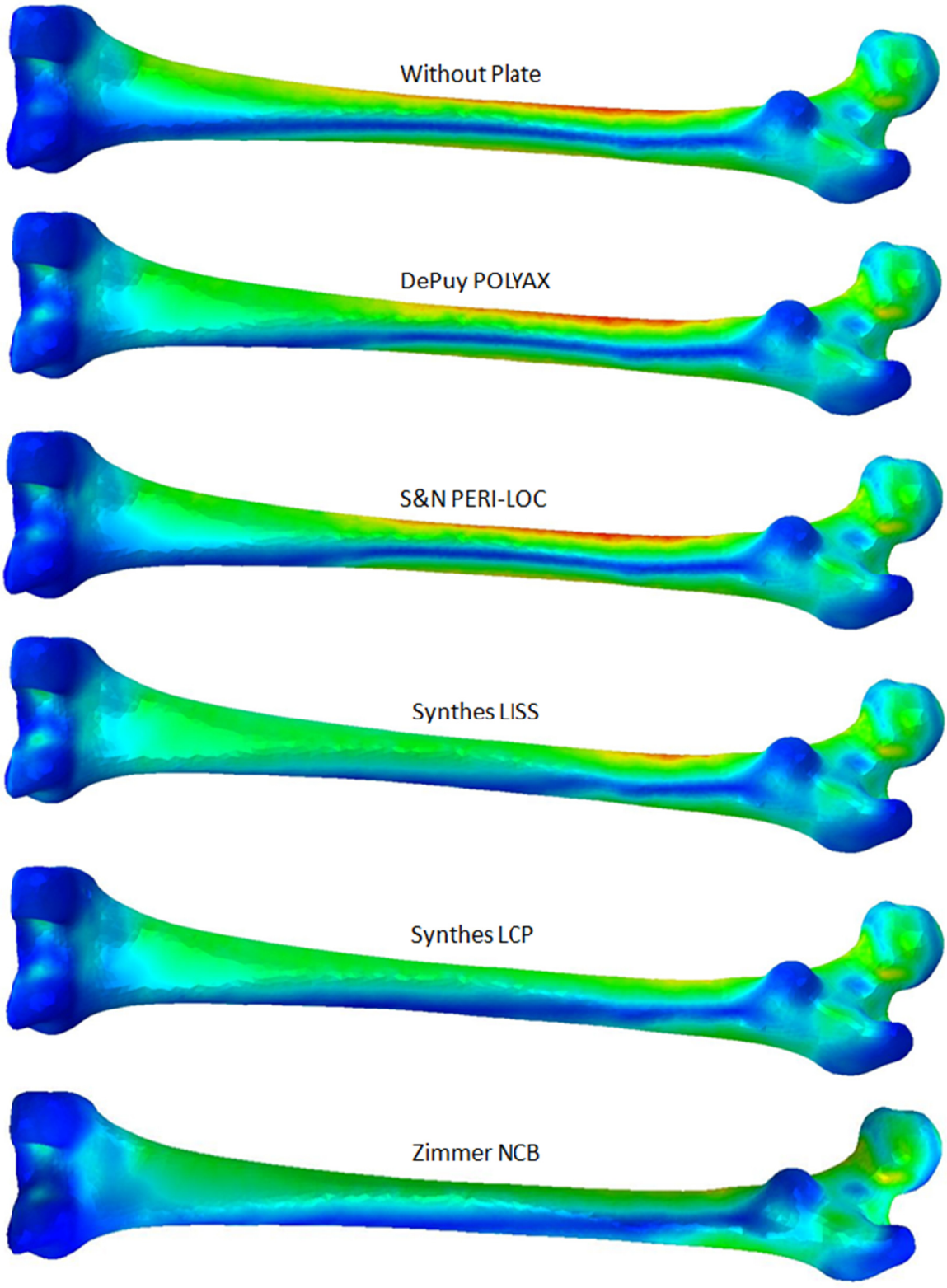

Fig. 93. FEA results illustrating the stress shielding effects of each plate (posterior view)

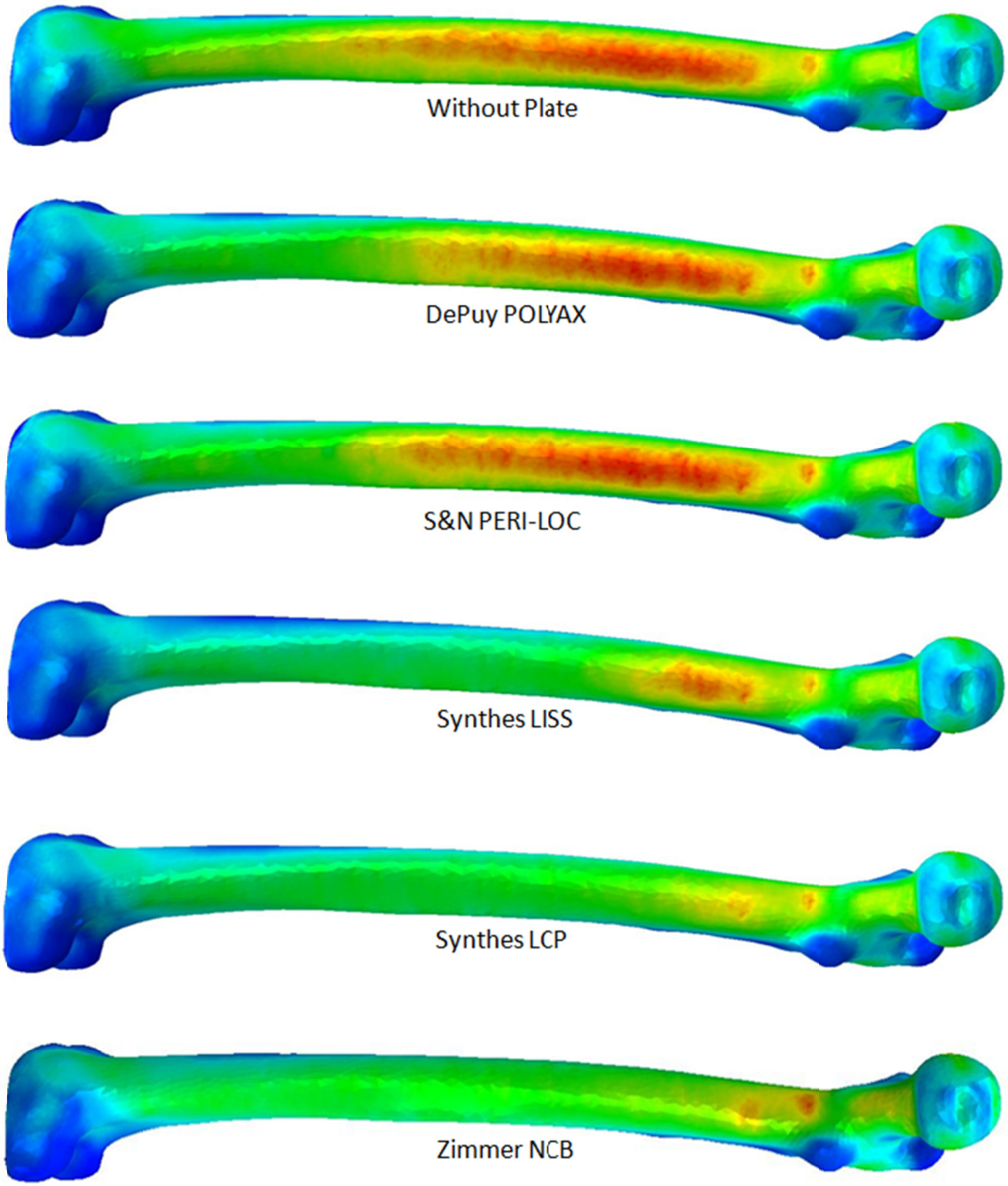

Fig. 94. FEA results illustrating the stress shielding effects of each plate (medial view)

Parametric Analysis

A contour plot of the stress field on the S&N plate is illustrated in fig. 95 where *A*, *B*, *C*, and *D* denote regions of stress concentration.

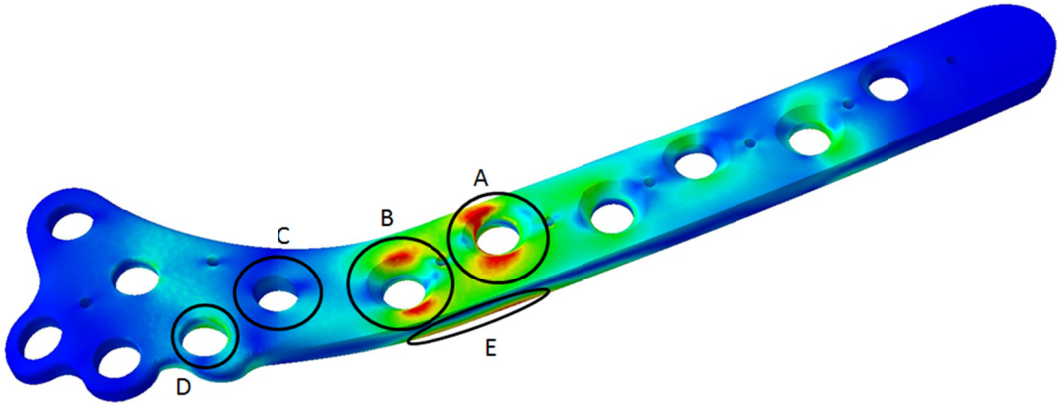

Fig. 95. Stress field contour plot showing stress concentrations on S&N plate

The local maximum von Mises stress in regions *A*, *B*, *C*, *D*, and *E* are tabulated in Table 7 as well as the resulting factor of safety and the S/N ratio of the factor of safety.

Table 7. FEA results of parametric analysis

Simul. No.	Strength (MPa)	Max. Stress (MPa) at location:					Max. Stress (MPa)	Factor of Safety	S/N (F.O.S)
		A	*B*	*C*	*D*	*E*			
1	290	581	292	48	124	277	581	0.50	-6.04
2	290	396	306	73	194	325	396	0.73	-2.71
3	290	157	149	151	119	99	157	1.85	5.33
4	890	417	268	50	122	152	417	2.13	6.59
5	890	221	173	61	129	164	221	4.03	12.10
6	890	253	176	42	107	209	253	3.52	10.93
7	170	141	228	86	298	147	298	0.57	-4.88
8	170	63	96	30	109	32	109	1.56	3.86
9	170	116	72	63	55	48	116	1.47	3.32

The ANOVA results are shown below in Table 8. Of the four design factors examined in this study, the plate material was found to have the highest percent contribution regarding the overall factor of safety, followed by plate thickness and the

use of an oblique screw. The use of hole inserts was found to have negligible effect on the global maximum stress; however, the inserts did reduce local maximum stresses. In other words, while inserts did not have significant effect in reducing plate failure given the simulated loading and fracture conditions, they did aid in reducing stress in regions around vacant holes not in proximity to the fracture.

Table 8. ANOVA results of parametric analysis

Source	D.F.	Sum of Squares, Sx.	Mean Square Vx=Sx/D.F.	ρ%
Material	2	207.64	103.82	60.94%
Thickness	2	102.25	51.13	30.01%
Inserts	2	5.06	2.53	1.49%
Oblique Screw	2	25.76	12.88	7.56%
Total	8	340.71	170.36	100.00%

The main effects are listed below in Table 9 and illustrated in the response curve of fig. 96. For each factor, the level with highest S/N ratio corresponds to the optimal parameter. The optimal parameters are listed below in Table 10. Using Eqs. XVII and XVIII, the overall factor of safety given the optimal parameters was calculated to be 6.56. Since the predicted optimum combination of parameter levels was not in the L_9 design of simulations, an additional simulation was performed with the optimal parameters. The results are found in Table 11. A 12.8% error occurred between the calculated factor of safety and the FEA results.

Table 9. Main effects

Level	*Factor*			
	Material	Thickness	Inserts	Oblique Screw
1	-1.14	-1.44	2.92	3.13
2	9.87	4.42	2.40	1.11
3	0.77	6.53	4.18	5.26

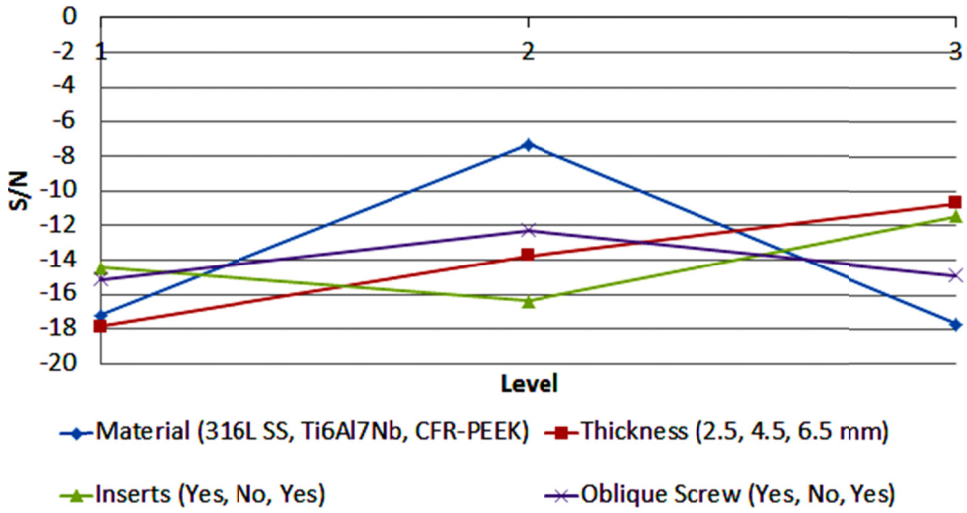

Fig. 96. Response curve for each factor

Table 10. Optimal design parameters

Source	Value	S/N
Material	Ti6Al7Nb	9.87
Thickness	5.5 mm	6.53
Inserts	Yes	4.18
Oblique Screw	Yes	5.26

Table 11. FEA results with optimum parameters

Max. Stress (MPa) at location:					Max. Stress (MPa)	Factor of Safety
A	*B*	*C*	*D*	*E*		
153	127	129	103	86	153	5.82

FEM-Integrated Structural Optimization

Fig. 97 illustrates the optimization history showing the parameter values at each pass. Including the initial static analysis, a total of ten iterations were performed before the optimal was reached. Fig. 98 and Fig. 99 show the maximum stress and total mass, respectively, at each pass. The simulation results after the final optimization pass are

illustrated in Fig. 100. Rounding to the nearest 0.5 mm, the optimum values for the width and thickness of the medial locking plate were determined to be 19.5 mm and 3.5 mm, respectively.

Finally, the structurally optimized plate was modified so that the axial diameter throughout the proximal length on the nail – that which is secured to the diaphysis – had an axial diameter matching the approximated average outer diameter in the sample (28.0 mm, fig. 101). The optimized plate was then assembled into the fracture model used in the comparative performance analysis (fig. 102), where each of the fracture and loading conditions were simulated given the high *q*-angle loading direction (15°). The FEA results comparing the medial locking plate to the five plating systems previously analyzed are illustrated in fig. 103 and Fig. 104. For the intact femur model, the optimized plate actually had a slightly less factor of safety than the Synthes LISS, but in all loading cases neither plate failed, whereas the other plates did. However, for the distal transverse fracture model, the optimized plate outperformed the LISS by a factor of 5 for each load case. Only during stumbling did yielding occur in the optimized plate, while all other plates analyzed yielded during each of the loading scenarios.

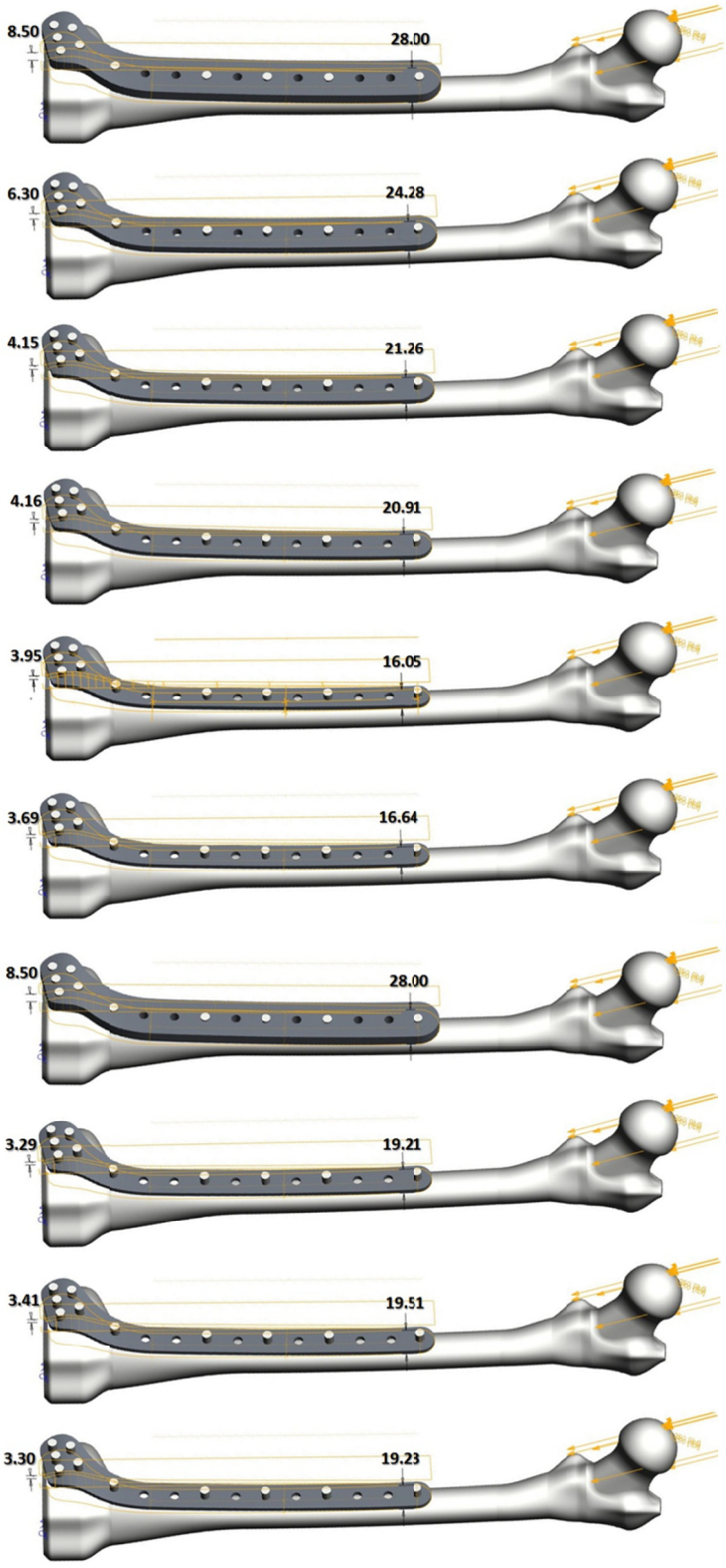

Fig. 97. Optimization history (beginning from top and progressing downward)

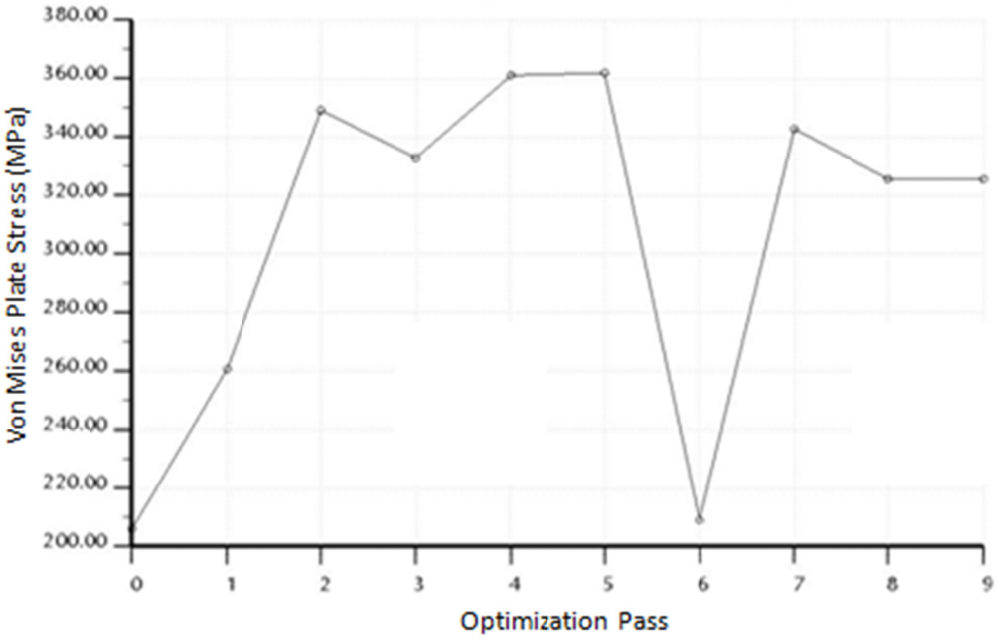

Fig. 98. Optimization history showing the maximum von Mises stress for each iteration

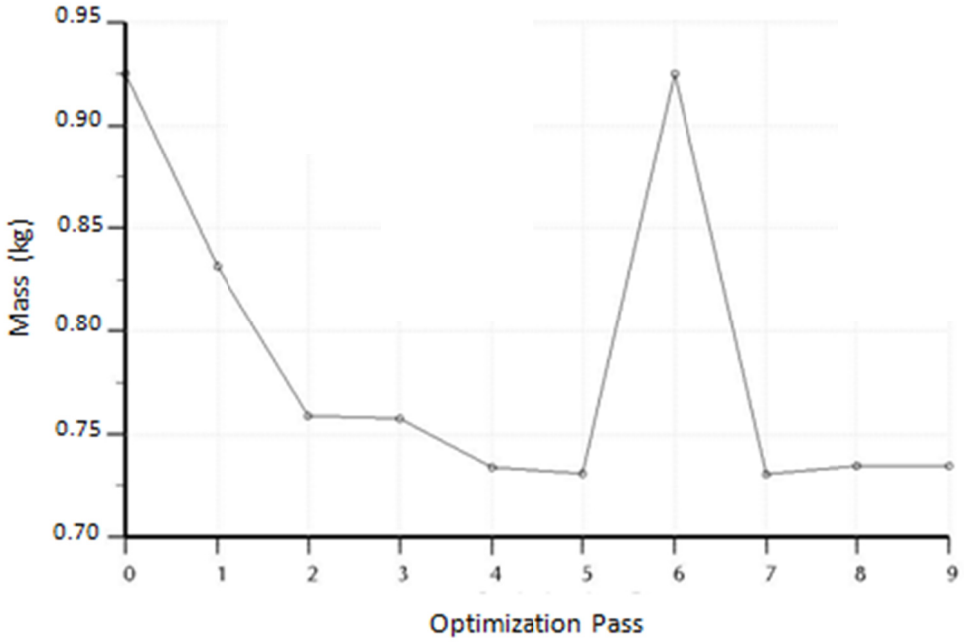

Fig. 99. Optimization history showing the overall mass of the fracture model for each iteration

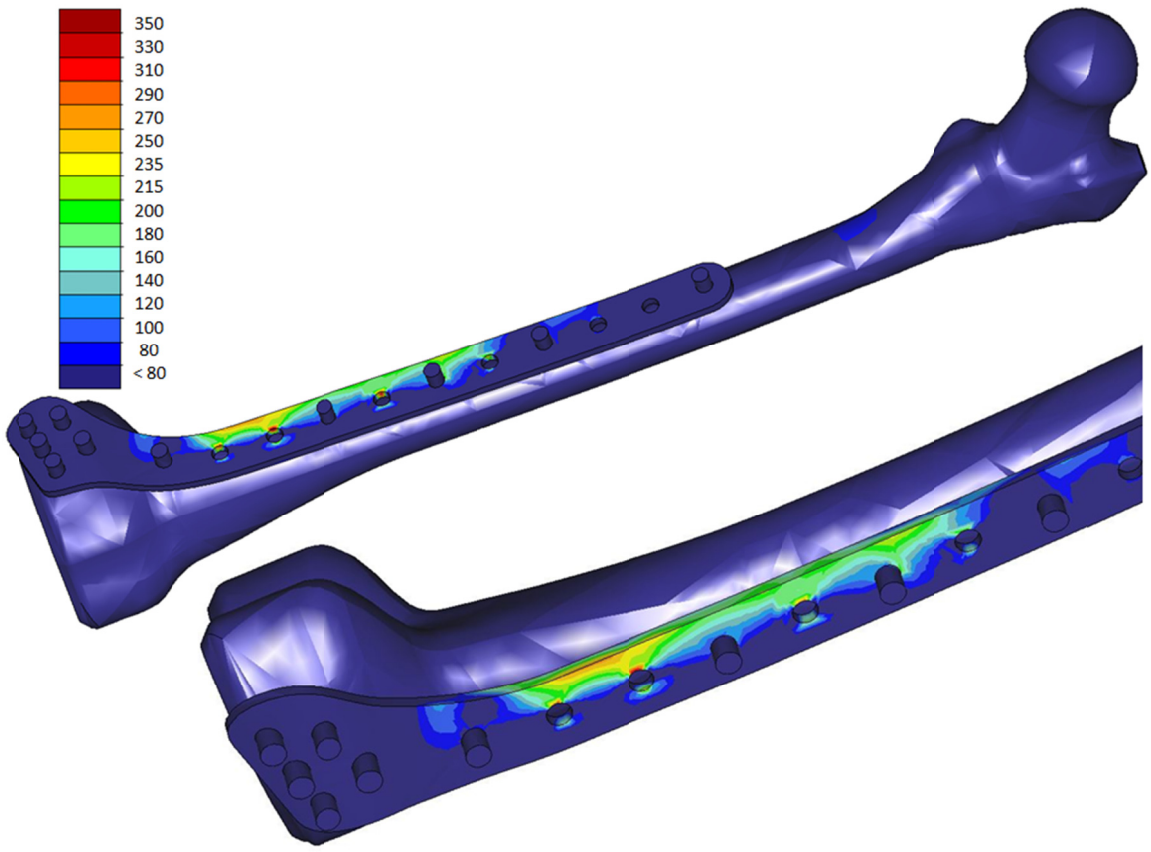

Fig. 100. Structurally optimized plate geometry showing regions of stress concentration

Fig. 101. Final geometry of medial locking plate (with axial contour in the diaphyseal region and rounded edges)

Fig. 102. Fracture model using the optimized MLP (*far left:* fracture with bone loss, *right three:* distal fracture)

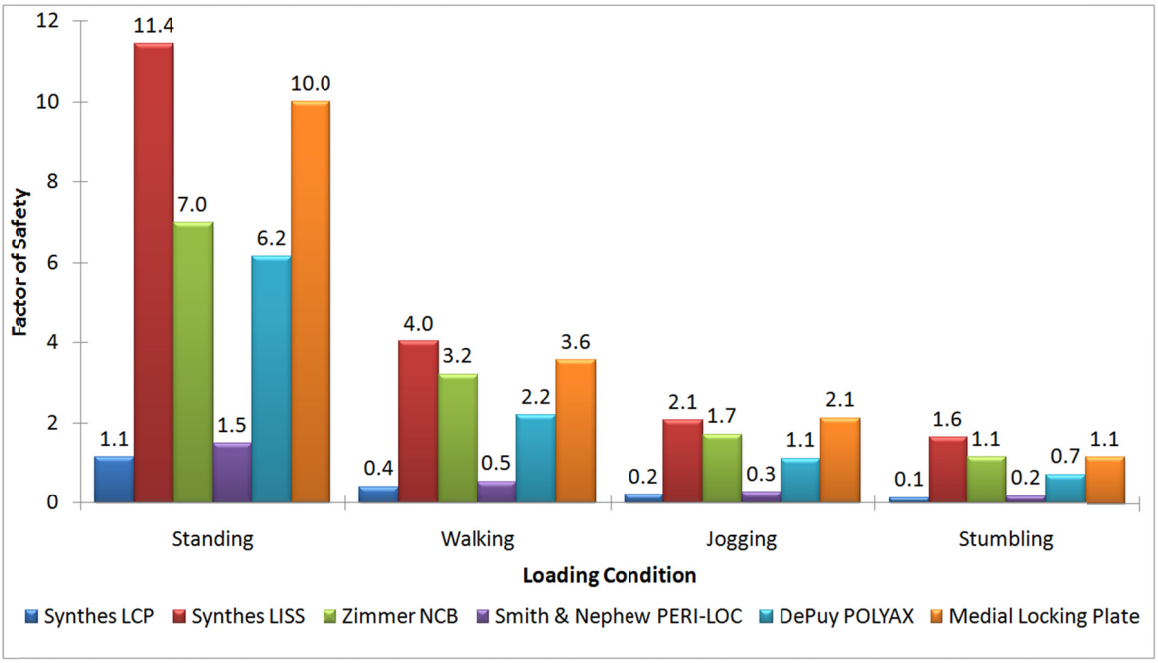

Fig. 103. FEA results of intact femur fixated with distal locking plates (high *q*-angle loading)

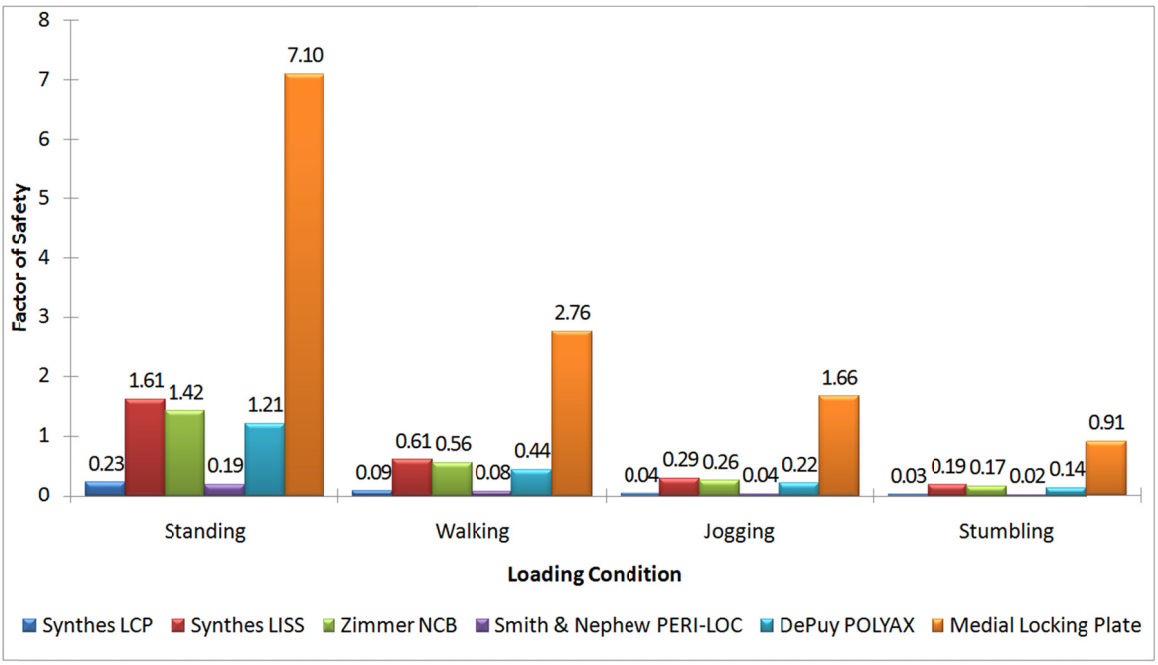

Fig. 104. FEA results of transversely fractured femur fixated with distal locking plates (high *q*-angle loading)

Experimental Testing

Experimental and simulation results are compared in Table 12. The simulation results were acquired from the strain output matrix at locations corresponding the strain gauges. Fig. 105-Fig. 111 illustrate the longitudinal, hoop, and 45° strain curves as a function of hip joint load. Because of the difference in bone geometry between the Sawbones composite femur used for experimental testing and that of the simulated femur model, an acceptable percent difference between simulated and experimental results were assumed to be approximately 30%. For general purposes, it is widely accepted in engineering practice that a percent difference of 20% or less is acceptable when using non-linear finite element methods.

Table 12. Experimental and simulation results

				Longitudinal Strain		
				Exp.	*FEA*	*% Diff.*
Strain	*250 lbf Load*	**Intact Femur**	*Lateral Femur*	-0.0006868	-0.0005800	15.5%
			Medial Femur	-0.0000700	-0.0000660	5.8%
		" " w/ Plate	*Plate*	-0.0000230	-0.0000260	13.0%
			Lateral Femur	-0.0001590	-0.0001560	1.9%
			Medial Femur	-0.0000421	-0.0000409	2.9%
		Fractured, w/ Plate	*Plate*	-0.0001490	-0.0001010	32.2%
		" " w/ Bone Loss	*Plate*	0.0008130	0.0005700	29.9%
	700 lbf Load	**Intact Femur**	*Lateral Femur*	-0.0023783	-0.0017000	28.5%
			Medial Femur	-0.0001028	-0.0001056	2.7%
		" " w/ Plate	*Plate*	-0.0000650	-0.0000646	0.6%
			Lateral Femur	-0.0013460	-0.0008000	40.6%
			Medial Femur	0.0000187	0.0000174	7.0%

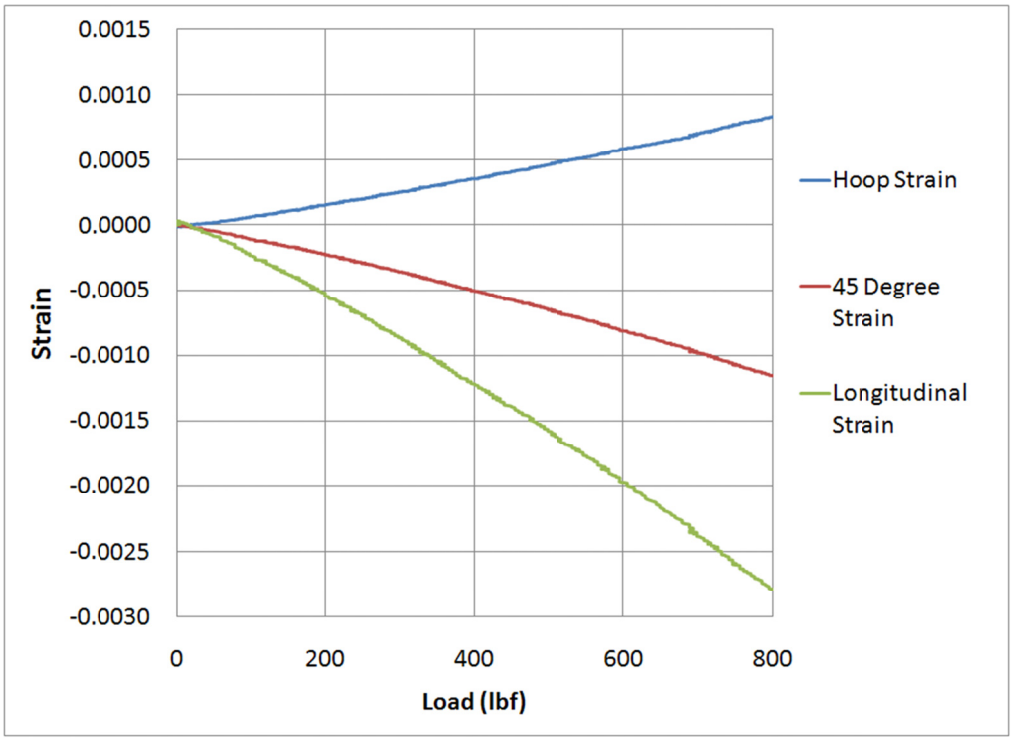

Fig. 105. Experimental results for intact femur (lateral strain gage rosette)

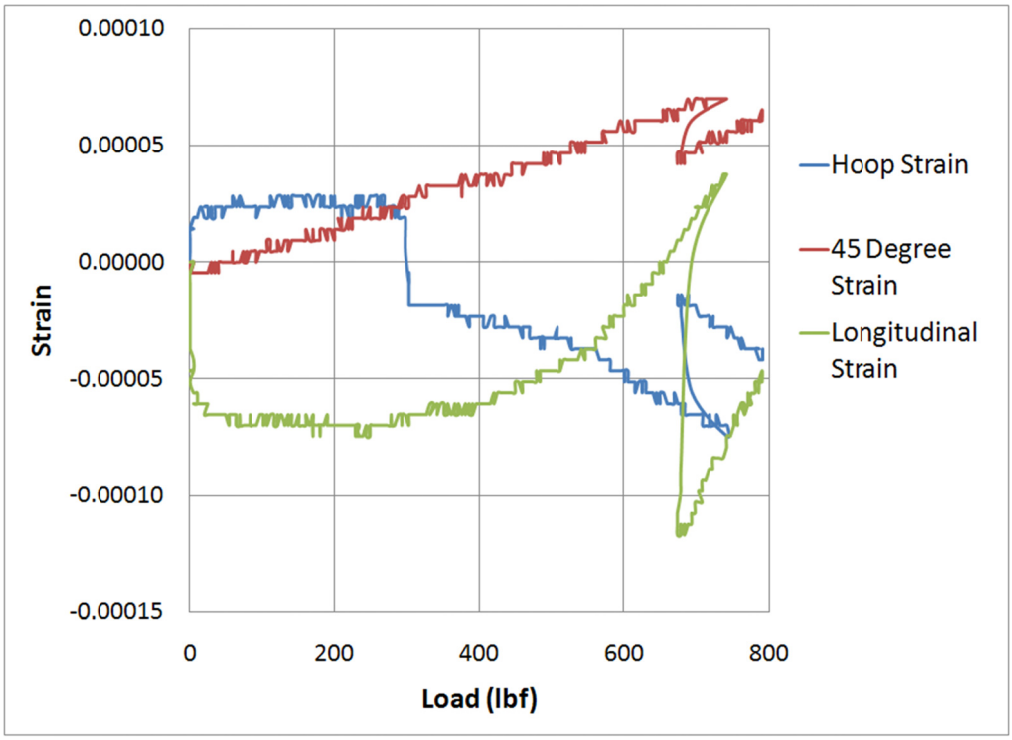

Fig. 106. Experimental results for intact femur (medial strain gage rosette)

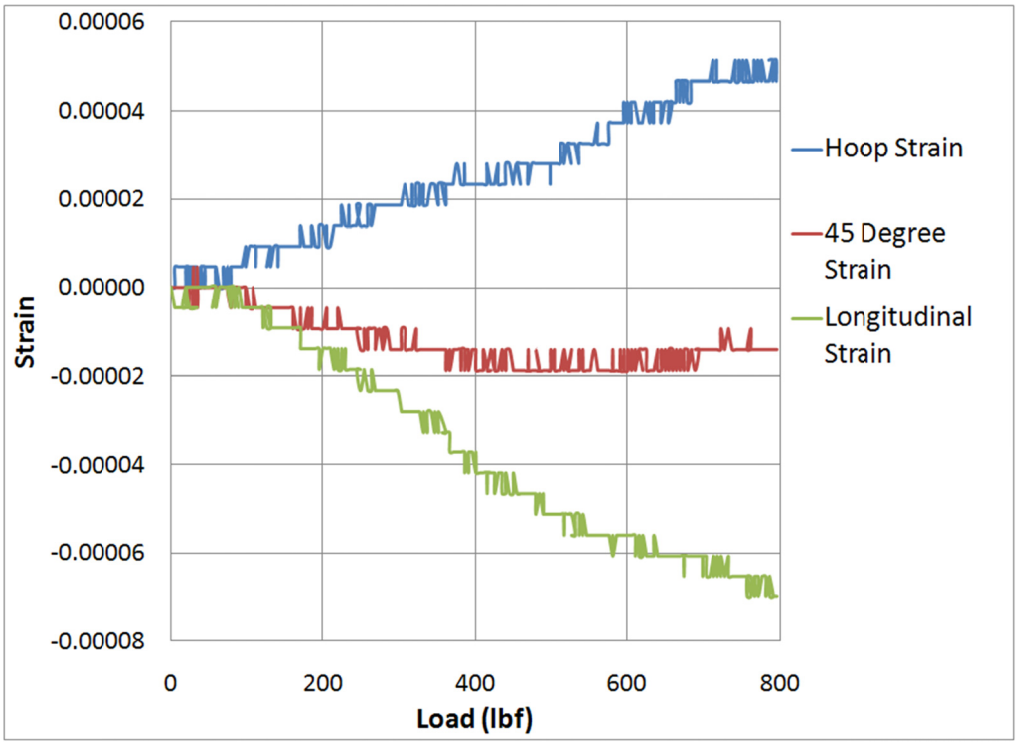

Fig. 107. Experimental results for fixated intact femur (plate strain gage rosette)

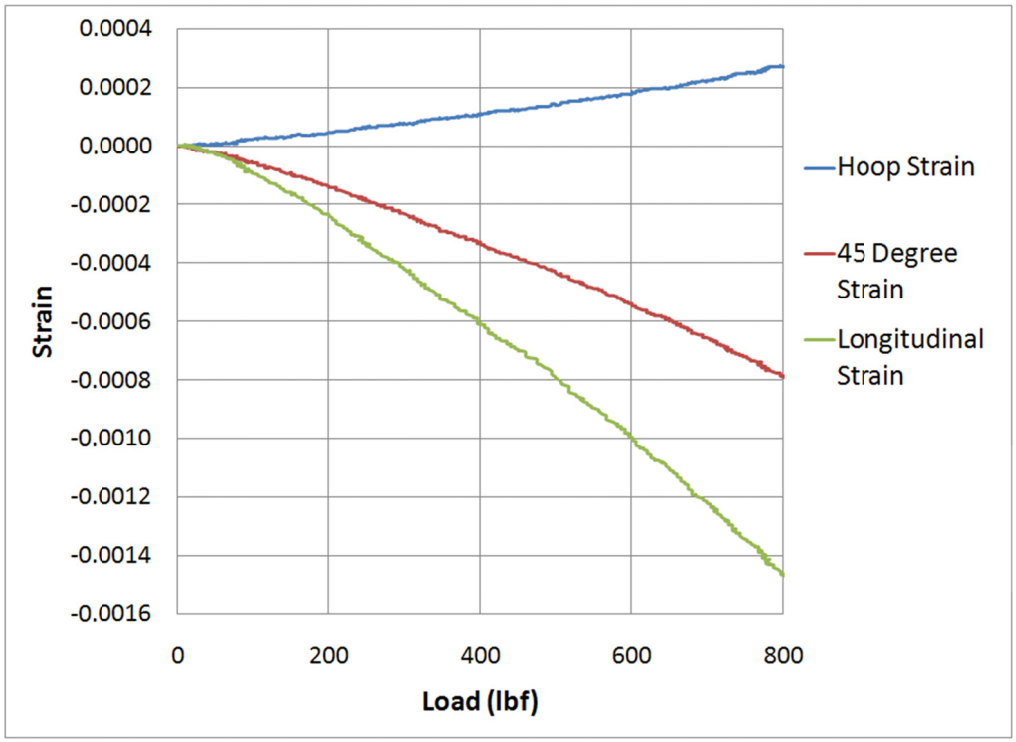

Fig. 108. Experimental results for fixated intact femur (lateral strain gage rosette)

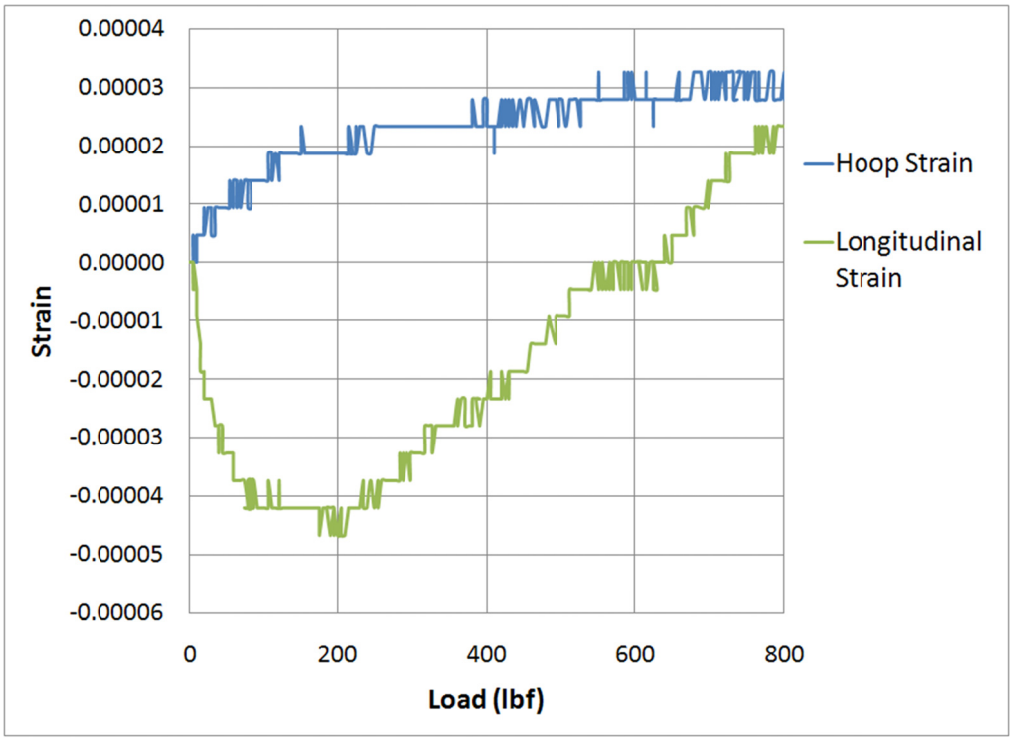

Fig. 109. Experimental results for fixated intact femur (medial strain gage rosette)

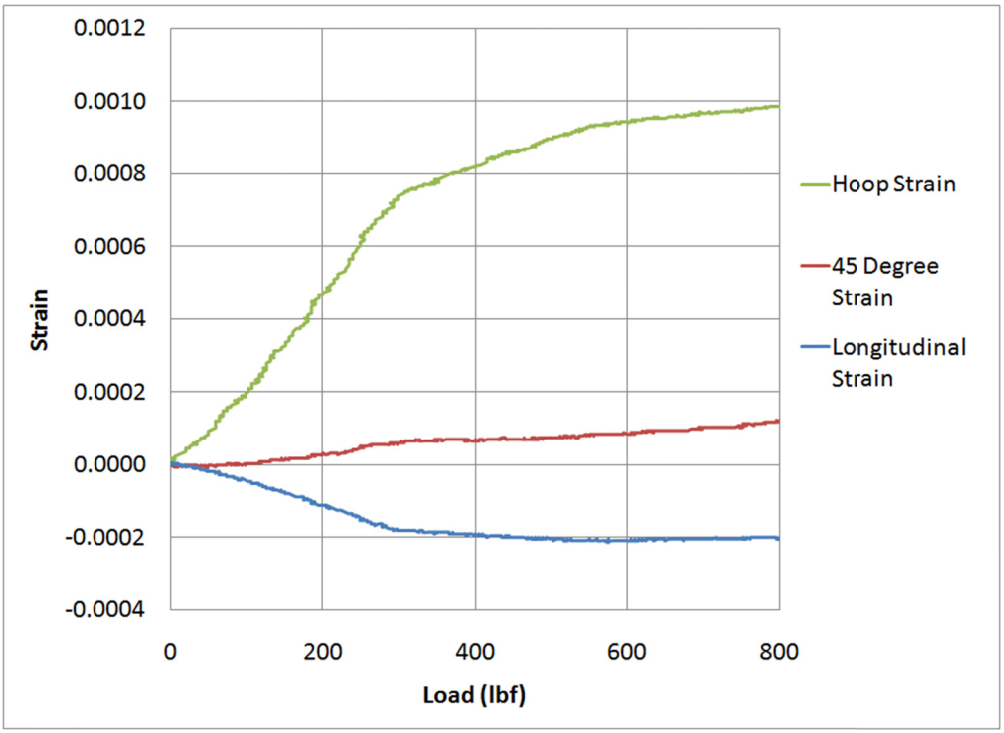

Fig. 110. Experimental results for fixated fractured femur (plate strain gage rosette)

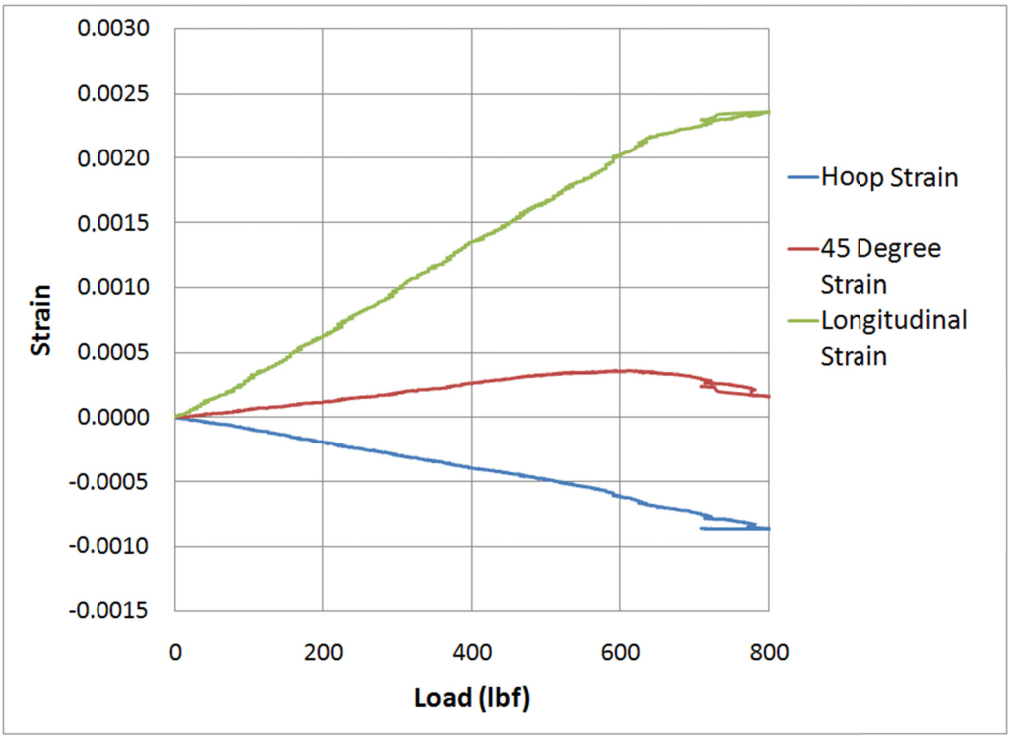

Fig. 111. Experimental results for fixated fractured femur with bone loss (plate strain gage rosette)

Discussion

Shape Optimization

The shape optimization technique, based on the average specimen model, allows design engineers to isolate the shape from the size of features during the design process – as long as they are independent of each other (*i.e.* length does not affect curvature). Statistical analysis of geometry measurements in the previous step help to determine interdependence of design variables. The present case study did not address this variable interdependence because previous studies have already determined that femoral length is not correlated to curvature [87]. Therefore, the models could be scaled without affecting average curvature outcome.

A cue in the statistical analysis performed on the femur sample suggests that the same basic shape is consistent among the population to a certain degree: the location of the most anterior point of the anterior diaphyseal surface (as a function of percent length from the proximal end) was reasonably consistent. The magnitude of curvature varies to a large degree, but relatively little variation seems to exist regarding the location along the diaphysis where curvature is the highest. Coupling statistical results with shape optimization can aid in determining early on whether multiple shapes *may* be necessary to fit the patient population. Finite element simulations followed by experimental mechanical testing and animal/human *in vivo* tests are required for final verification as to whether multiple shapes are necessary. Again, the goal of the computer-aided implant design process is to minimize the time and expenses associated with experimental testing by approaching the optimal design of the entire implant system prior to prototyping.

Simulation-Based Comparative Performance Analysis

Before beginning the development of conceptual designs, it is important to have a clear understanding of how existing competitive devices perform. Clinical studies comparing different devices are expensive and pose risks to the patients. Experimental mechanical testing is also expensive, and limitations of equipment and specimen samples limit the type of loading scenarios that can be accurately reproduced. By verifying simulation results with those found experimentally using simple physiological

conditions, it is inferred that complex simulated physiological conditions – based on the same system – are also verified. This is standard engineering design practice.

The highest percent difference between simulation and experimental results occurred with experiment three (distal transverse fracture fixated with Synthes LISS). This was the only experimental case where the corresponding finite element simulation featured nonlinear contact within the fracture site. The other simulation cases *did* have nonlinear contact constraints assigned between the femur and plate, but only did the fracture with bone loss scenario actually have loading-induce contact in this region during the analysis. The contact pressure within the transverse fracture was much higher and, therefore, had a much higher effect on the results than did plate/femur contact. This could be the cause of the higher percent difference with the transverse fracture case.

Friction within the distal transverse fracture could also have played a role in the higher percent difference between the simulated and experimental results in the transverse fracture case. The experimental test had dry, rough contact, whereas the FE simulation assumed wet contact. Additionally, the initial fracture gap between the femur fragments was higher for the experimental test compared to the corresponding simulation (approximately 0.2 mm verses 0.0001 mm, respectively).

For the remaining three experimental tests, the remarkably low percent difference between experimental and simulation results suggests that that finite element fracture accurately represents human physiological loading conditions. Not

only is this inferred to be true for the simple standing load, but also for any complex quasi-static loads and fixation methods.

Simulation-Based Parametric Analysis

Material properties, particularly the stiffness and strength, were shown to have the greatest impact on plate performance. Stainless steel, having a slightly lower modulus of elasticity, resulted in slightly lower stresses. However, because the strength of the titanium alloy is significantly higher than stainless steel, using titanium yields the highest performance. CFR-PEEK also outperformed stainless steel. Although a higher factor of safety can be achieved using titanium alloy, CFR-PEEK did show to have potential as an alternative. The benefits of its flexibility may prove to outweigh its relatively lower strength when selecting materials for orthopaedic implants.

Increasing the thickness of the plate was the second greatest contributing factor towards plate performance. Intuitively, this is expected as the cross-sectional area is increased. However, two adverse effects arise with increasing thickness. First, increasing implant size potentially increases the inflammation in surrounding tissue [74]. Second, the flexibility of an implant is inversely related to thickness, and decreased flexibility increases the effects of stress shielding [116]. These two design constraints must be examined along with the performance measures for optimum implant design.

Using an oblique screw also aided in increasing the factor of safety. It acts as a stabilizing member in a manner similar to a kickstand on a bicycle. Because current distal femur plates do not offer the ability to implement oblique screws at angles large

enough to give longitudinal support, a new screw/plate interface design would be necessary if this technique is adopted. Optimum angles, given the location of the screw, could be determined using the described method.

Although the overall factor of safety was not significantly affected by the use of screw hole plugs, they are beneficial for reducing local stress concentrations around vacant screw holes. The stress concentration factors in these areas were reduced because the hole was virtually eliminated. However, stress concentrations were still present due to edges around the counter-sink and the reduced thickness near the plugged hole. Eliminating countersink features around the screw holes could help improve the performance effect of inserts.

Structural Optimization

Structural optimization was performed assuming worst-case loading conditions following a full recovery of the patient. Patients are strongly advised to keep weight off of their leg before bone remodeling and healing takes place, let alone participate in activities involving impact, including walking. However, it is impossible to insure that the fracture heals in an "ideal" environment; therefore, design precautions must be taken to ensure the implant can withstand 100% of the patient's weight via static and low impact loading. By using structural optimization techniques to design for extreme loading conditions after full recovery, and by implementing a sufficient factor of safety, the possibly of mechanical failures occurring prior to recovery can be minimized.

Various fracture and loading scenarios can then be simulated using the optimized implant geometry to insure its mechanical integrity against un-recommended loading.

Although titanium alloy – the highest structurally-performing material from the parametric analysis – was used for the present structural analysis, it would be worthwhile to further examine the feasibility of CFR-PEEK plates. By applying the appropriate material properties, the optimum dimensions can be obtained using the established methodology. Further simulations would then be required to ensure mechanical integrity during various fracture and loading conditions as mentioned earlier, followed by *in vivo* testing. Although it is obvious that titanium will outperform CFR-PEEK from a structural point of view, the added long-term benefits of a more flexible CFR-PEEK may prove its superiority.

Finally, a complete distal locked plating system can be designed based on the present case study results and further analysis – particularly dealing with the locking screws themselves. The use of oblique screw orientation for the purpose of structural support showed potential during the parametric analysis. As mentioned previously, a new screw/plate interlocking system needs to be designed to allow for higher angle orientation. The simulation and optimization techniques can then be applied in order to determine the optimum orientation angle.

CHAPTER V. CONCLUSION & RECOMMENDATIONS

Conclusion

The design of load-bearing, internal fracture fixation implants is a complicated process involving the optimization of performance measures while meeting physiological-related design constraints not typically considered in other engineering fields. The developed simulation-based approach is capable of improving contour fit and structural integrity while minimizing weight and stress shielding. Complex loading conditions can be simulated while various implant geometry features, fixation techniques, and materials can be analyzed in an efficient manner compared to traditional trial-and-error methods. The design methodology is not only applicable for femoral fixation implants as demonstrated with the present case studies; it can be utilized for the design of internal fixation implants intended for any fracture location. Ultimately, the comprehensive simulation-based methodology for the design and optimization of orthopaedic internal fixation implants can help in both improving patient care and reducing costs associated with R&D.

Recommendations

Recommended improvements on the design methodology include:

- Expand on statistical variation analysis by determining modes of variation in the bone specimen in addition to the geometry measurements taken in the present study (*e.g.* twisting, shaft axis angle relative to knee joint, etc.)
- Analyze and visualize modes of variation using Polyworks

- Incorporate material selection in structural optimization techniques (including particle volume fraction/size of polymer composites) using ANSYS Workbench.
- Use CT scanner to create CAD model of Sawbones composite specimen for experimental validation of numerical simulations. (a better approach for validation than using a scanned cadaver specimen with geometry different from the test specimen).
- Use CT voxel data to import material properties as a function of bone density into finite element model (adopt and improve on current techniques).
- Predict fatigue failure via cyclic loading (weight-shifting, walking, jogging, and running) and applying material failure criteria.
- Further investigate the use of CFR-PEEK for manufacturing flexible IM nails and locking plates (may need titanium core w/ relatively small cross-sectional area for strength and stability during recovery)
- Apply muscular reaction forces to the finite element fracture models based on experimental measurements.

APPENDIX A

Table 13. Geometry measures and statistics of femur sample

Femur Set	#	Specimen #	Race	Sex	Age	*R* (cm)		*L* (cm)		*SL* (cm)		*OD* (cm)		*ID* (cm)		*T* (cm)		L/OD		*LMAP*	
1	1	HTH 1702	2	2	2	159.8		46.0		31.5		2.44		1.41		0.52		12.9		27.2%	
African American	2	HTH 2867	2	2	2	123.7		45.4		31.2		2.92		1.58		0.67		10.7		30.8%	
Female	3	HTH 0152	2	2	2	142.1	138.1	43.9	45.5	28.8	30.8	2.65	2.64	1.39	1.39	0.63	0.62	10.9	11.7	29.7%	30.4%
Age 70-80	4	HTH 2593	2	2	2	109.9		46.8		31.6		2.74		1.28		0.73		11.5		36.6%	
	5	HTH 1702	2	2	2	154.7		45.2		31.0		2.46		1.31		0.58		12.6		27.8%	
2	1	HTH 1241	2	1	1	88.2		50.2		34.9		3.21		1.70		0.76		10.9		42.6%	
African American	2	HTH 2060	2	1	1	112.3		50.9		35.5		3.56		1.74		0.91		10.0		42.4%	
Male	3	HTH 2113	2	1	1	120.8	106.5	49.5	50.0	34.0	34.3	2.99	3.25	1.56	1.71	0.72	0.77	11.4	10.6	36.0%	39.7%
Age 30-40	4	HTH 2930	2	1	1	127.3		52.9		36.7		3.21		2.00		0.61		11.4		35.2%	
	5	HTH 0327	2	1	1	84.0		46.3		30.4		3.26		1.57		0.85		9.3		42.3%	
3	1	HTH 0700	1	2	1	95.3		43.0		30.4		2.44		1.20		0.62		12.5		39.7%	
Caucasian	2	HTH 0514	1	2	1	107.6		41.3		29.0		2.37		1.15		0.61		12.2		39.5%	
Female	3	HTH 2056	1	2	1	112.3	114.0	44.0	44.0	29.5	30.3	2.42	2.49	1.06	1.25	0.68	0.62	12.2	12.2	32.6%	38.3%
Age 30-40	4	HTH 0552	1	2	1	127.5		46.8		31.7		2.47		1.44		0.52		12.8		33.4%	
	5	HTH 1119	1	2	1	127.0		44.7		30.9		2.73		1.41		0.66		11.3		46.4%	
4	1	HTH 2186	1	1	1	106.1		47.8		31.3		2.60		1.46		0.57		12.0		30.7%	
Caucasian	2	HTH 2100	1	1	1	124.1		49.2		32.1		3.01		1.45		0.78		10.7		32.3%	
Male	3	HTH 0445	1	1	1	172.4	126.8	47.4	46.7	30.6	30.9	2.89	2.84	1.40	1.47	0.75	0.69	10.6	10.9	29.8%	37.6%
Age 30-40	4	HTH 0827	1	1	1	92.0		43.9		30.3		3.10		1.74		0.68		9.8		50.1%	
	5	HTH 0544	1	1	1	139.8		45.0		30.2		2.62		1.28		0.67		11.5		45.3%	
5	1	HTH 3075	2	1	2	108.1		47.1		32.9		3.05		1.73		0.66		10.8		39.3%	
African American	2	HTH 2099	2	1	2	113.2		47.7		33.2		3.22		1.50		0.86		10.3		38.2%	
Male	3	HTH 2642	2	1	2	210.1	131.2	49.5	47.0	33.3	32.0	2.91	3.02	1.47	1.54	0.72	0.74	11.4	10.6	36.6%	39.0%
Age 70-80	4	HTH 1370	2	1	2	119.7		45.2		30.3		3.10		1.59		0.76		9.8		43.3%	
	5	HTH 1898	2	1	2	104.8		45.7		30.2		2.84		1.42		0.71		10.6		37.6%	
6	1	HTH 2870	2	2	1	194.7		42.5		30.6		2.78		1.58		0.60		11.0		38.1%	
African American	2	HTH 1214	2	2	1	98.4		42.2		28.7		2.39		1.12		0.64		12.0		39.6%	
Female	3	HTH 2402	2	2	1	170.3	135.2	45.7	43.5	31.3	30.1	2.67	2.58	1.34	1.43	0.67	0.58	11.7	11.7	35.0%	37.6%
Age 30-40	4	HTH 0461	2	2	1	92.0		44.2		29.9		2.60		1.59		0.51		11.5		40.7%	
	5	HTH 0439	2	2	1	120.6		43.2		30.1		2.45		1.50		0.48		12.3		34.7%	
7	1	HTH 1153	1	2	2	113.5		42.9		30.1		2.72		1.27		0.73		11.1		45.8%	
Caucasian	2	HTH 1755	1	2	2	132.9		44.6		31.2		2.74		1.80		0.47		11.4		43.0%	
Female	3	HTH 2139	1	2	2	105.2	111.8	42.1	43.5	28.7	30.3	2.56	2.66	1.57	1.62	0.50	0.52	11.2	11.4	43.8%	43.2%
Age 70-80	4	HTH 1587	1	2	2	111.9		42.3		30.4		2.46		1.90		0.28		12.4		38.3%	
	5	HTH 1191	1	2	2	95.5		45.3		31.1		2.83		1.58		0.63		11.0		45.1%	
8	1	HTH 1728	1	1	2	96.1		49.5		32.5		3.04		1.48		0.78		10.7		40.4%	
Caucasian	2	HTH 0297	1	1	2	83.0		45.7		29.0		2.83		1.50		0.67		10.3		39.2%	
Male	3	HTH 1823	1	1	2	77.8	108.5	43.2	46.9	27.4	30.4	2.77	2.95	1.96	1.64	0.41	0.66	9.9	10.3	40.2%	38.8%
Age 70-80	4	HTH 1440	1	1	2	208.1		48.4		31.8		2.96		1.77		0.60		10.8		37.2%	
	5	HTH 0236	1	1	2	77.6		47.8		31.4		3.15		1.47		0.84		10.0		37.2%	
Caucasian	*Average*					115.3		45.2		30.5		2.74		1.49		0.62		11.2		39.50%	
	Standard Deviation					31.6		2.5		1.3		0.24		0.24		0.14		0.9		0.05	
	Maximum					208.1		49.5		32.5		3.15		1.96		0.84		12.8		50.07%	
	Minimum					77.6		41.3		27.4		2.37		1.06		0.28		9.8		29.85%	
African American	*Average*					127.7		46.5		31.8		2.87		1.52		0.68		11.1		36.69%	
	Standard Deviation					34.4		2.9		2.2		0.33		0.19		0.12		0.9		0.05	
	Maximum					210.1		52.9		36.7		3.56		2.00		0.91		12.9		43.29%	
	Minimum					84.0		42.2		28.7		2.39		1.12		0.48		9.3		27.20%	
Male	*Average*					118.3		47.6		31.9		3.02		1.59		0.71		10.6		38.79%	
	Standard Deviation					38.6		2.5		2.3		0.23		0.19		0.12		0.7		0.05	
	Maximum					210.1		52.9		36.7		3.56		2.00		0.91		12.0		50.07%	
	Minimum					77.6		43.2		27.4		2.60		1.28		0.41		9.3		29.85%	
Female	*Average*					124.8		44.1		30.4		2.59		1.42		0.58		11.8		37.39%	
	Standard Deviation					27.5		1.6		1.0		0.17		0.22		0.11		0.7		0.05	
	Maximum					194.7		46.8		31.7		2.92		1.90		0.73		12.9		46.42%	
	Minimum					92.0		41.3		28.7		2.37		1.06		0.28		10.7		27.20%	
Age 30-40	*Average*					120.6		46.0		31.4		2.79		1.46		0.66		11.4		38.32%	
	Standard Deviation					29.8		3.2		2.2		0.35		0.24		0.11		0.9		0.05	
	Maximum					194.7		52.9		36.7		3.56		2.00		0.91		12.8		50.07%	
	Minimum					84.0		41.3		28.7		2.37		1.06		0.48		9.3		29.85%	
Age 70-80	*Average*					122.4		45.7		30.9		2.82		1.55		0.64		11.0		37.86%	
	Standard Deviation					40.3		2.5		1.7		0.21		0.19		0.16		0.7		0.03	
	Maximum					210.1		49.5		33.3		3.22		1.96		0.86		12.9		45.79%	
	Minimum					77.6		42.1		27.4		2.44		1.27		0.28		9.8		27.20%	
Total	***Average***					**121.5**		**45.9**		**31.1**		**2.80**		**1.51**		**0.65**		**11.2**		**38.1%**	
	Standard Deviation					33.2		2.7		1.9		0.29		0.22		0.13		0.9		5.4%	
	Maximum					210.1		52.9		36.7		3.56		2.00		0.91		12.9		50.1%	
	Minimum					77.6		41.3		27.4		2.37		1.06		0.28		9.3		27.2%	

Table 14. FEA performance response of femoral plates (norm. q-angle)

Distal Femur Locking Plate	Load Case	Fracture Type	Von Mises Stress (MPa) at location* in plate: A	B	C	D	E	Max.	FOS
Synthes LCP	Standing	Intact	116	66	61	32	64	116	1.77
		Distal transverse fracture	114	136	119	56	77	136	1.51
		" " with bone loss	299	680	971	882	726	971	0.21
	Walking	Intact	347	197	182	97	183	347	0.59
		Distal transverse fracture	345	314	245	113	193	345	0.59
		" " with bone loss	676	1,615	2,928	2,505	2,246	2,928	0.07
	Jogging	Intact	578	329	303	162	305	578	0.35
		Distal transverse fracture	575	499	373	202	319	575	0.36
		" " with bone loss	952	2,293	4,345	3,612	3,378	4,345	0.05
	Stumbling	Intact	540	552	501	276	958	958	0.21
		Distal transverse fracture	958	830	603	380	540	958	0.21
		" " with bone loss	-	-	-	-	-	-	-
Synthes LISS	Standing	Intact	85	33	31	21	47	85	10.35
		Distal transverse fracture	87	84	97	57	55	97	9.07
		" " with bone loss	458	887	864	936	541	936	0.94
	Walking	Intact	255	99	93	64	133	255	3.45
		Distal transverse fracture	262	244	257	124	147	262	3.36
		" " with bone loss	1,178	2,268	2,478	2,585	1,403	2,585	0.34
	Jogging	Intact	420	166	155	107	222	420	2.10
		Distal transverse fracture	437	427	193	170	242	437	2.01
		" " with bone loss	1,280	2,315	2,502	2,786	1,454	2,786	0.32
	Stumbling	Intact	721	282	263	176	403	721	1.22
		Distal transverse fracture	743	716	740	319	342	743	1.18
		" " with bone loss	-	-	-	-	-	-	-
Zimmer NCB	Standing	Intact	279	113	67	53	175	279	3.15
		Distal transverse fracture	106	98	115	378	74	378	2.33
		" " with bone loss	290	560	939	459	620	939	0.94
	Walking	Intact	323	173	132	72	177	323	2.72
		Distal transverse fracture	320	260	274	126	180	320	2.75
		" " with bone loss	456	925	2,561	1,393	1,723	2,561	0.34
	Jogging	Intact	533	236	207	108	251	533	1.65
		Distal transverse fracture	533	428	437	237	289	533	1.65
		" " with bone loss	587	1,285	3,250	1,707	2,145	3,250	0.27
	Stumbling	Intact	889	340	365	212	423	889	0.99
		Distal transverse fracture	906	754	731	449	494	906	0.97
		" " with bone loss	-	-	-	-	-	-	-
Smith & Nephew PERI-LOC	Standing	Intact	67	53	72	52	41	72	2.85
		Distal transverse fracture	77	158	131	27	138	158	1.30
		" " with bone loss	253	948	994	486	896	994	0.21
	Walking	Intact	200	160	217	121	124	217	0.94
		Distal transverse fracture	197	392	307	194	325	392	0.52
		" " with bone loss	606	2,766	3,212	1,106	2,705	3,212	0.06
	Jogging	Intact	333	282	362	155	207	362	0.57
		Distal transverse fracture	366	677	597	459	561	677	0.30
		" " with bone loss	945	4,472	5,508	1,639	4,788	5,508	0.04
	Stumbling	Intact	566	480	616	442	352	616	0.33
		Distal transverse fracture	621	1,124	1,018	854	918	1,124	0.18
		" " with bone loss	-	-	-	-	-	-	-
DePuy POLYAX	Standing	Intact	33	47	57	44	24	57	15.44
		Distal transverse fracture	166	104	46	74	92	166	5.30
		" " with bone loss	789	1,075	987	1,051	885	1,075	0.82
	Walking	Intact	101	142	171	132	73	171	5.15
		Distal transverse fracture	353	312	128	292	329	353	2.49
		" " with bone loss	1,382	1,947	1,739	1,064	1,622	1,947	0.45
	Jogging	Intact	173	234	284	219	122	284	3.10
		Distal transverse fracture	605	540	213	579	448	605	1.45
		" " with bone loss	1,455	2,083	1,955	1,098	2,083	1,767	0.50
	Stumbling	Intact	286	401	483	373	203	483	1.82
		Distal transverse fracture	723	640	248	638	677	723	1.22
		" " with bone loss	-	-	-	-	-	-	-

Table 15. FEA performance response of femoral plates (high q-angle)

Distal Femur Locking Plate	Load Case	Fracture Type	Von Mises Stress (MPa) at location* in plate: A	B	C	D	Max.	FOS
Synthes LCP	Standing	Intact	98	156	179	95	179	1.15
		Distal transverse fracture	480	777	893	862	893	0.23
		" " with bone loss	480	777	893	862	893	0.23
	Walking	Intact	273	432	495	260	495	0.41
		Distal transverse fracture	1,292	2,176	2,409	2,337	2,409	0.09
		" " with bone loss	1,292	2,176	2,409	2,337	2,409	0.09
	Jogging	Intact	496	855	982	520	982	0.21
		Distal transverse fracture	2,643	4,362	4,911	4,742	4,911	0.04
		" " with bone loss	2,643	4,362	4,911	4,742	4,911	0.04
	Stumbling	Intact	844	1,340	1,539	818	1,539	0.13
		Distal transverse fracture	4,181	6,757	7,768	7,500	7,768	0.03
		" " with bone loss	4,181	6,757	7,768	7,500	7,768	0.03
Synthes LISS	Standing	Intact	48	77	-	56	77	11.43
		Distal transverse fracture	511	545	-	524	545	1.61
		" " with bone loss	511	545	-	524	545	1.61
	Walking	Intact	177	218	-	160	218	4.04
		Distal transverse fracture	1,333	1,447	-	1,392	1,447	0.61
		" " with bone loss	1,333	1,447	-	1,392	1,447	0.61
	Jogging	Intact	312	425	-	307	425	2.07
		Distal transverse fracture	2,780	2,998	-	2,881	2,998	0.29
		" " with bone loss	2,780	2,998	-	2,881	2,998	0.29
	Stumbling	Intact	536		-	485	536	1.64
		Distal transverse fracture	4,397	4,742	-	4,558	4,742	0.19
		" " with bone loss	4,397	4,743	-	4,558	4,743	0.19
Zimmer NCB	Standing	Intact	115	126	90	42	126	6.98
		Distal transverse fracture	417	621	480	427	621	1.42
		" " with bone loss	417	621	480	427	621	1.42
	Walking	Intact	134	274	223	106	274	3.21
		Distal transverse fracture	1,078	1,580	1,270	1,134	1,580	0.56
		" " with bone loss	1,078	1,580	1,270	1,134	1,580	0.56
	Jogging	Intact	234	514	427	213	514	1.71
		Distal transverse fracture	3,416	2,638	2,297	2,349	3,416	0.26
		" " with bone loss	3,416	2,638	2,297	2,349	3,416	0.26
	Stumbling	Intact	353	766	641	326	766	1.15
		Distal transverse fracture	3,634	5,257	4,173	3,715	5,257	0.17
		" " with bone loss	3,634	5,257	4,173	3,715	5,257	0.17
Smith & Nephew PERI-LOC	Standing	Intact	138	138	112	44	138	1.49
		Distal transverse fracture	691	872	842	1,052	1,052	0.19
		" " with bone loss	415	314	404	337	415	0.49
	Walking	Intact	385	383	312	267	385	0.53
		Distal transverse fracture	1,718	2,182	2,094	2,629	2,629	0.08
		" " with bone loss	1,718	2,182	2,094	2,629	2,629	0.08
	Jogging	Intact	699	763	615	528	763	0.27
		Distal transverse fracture	3,792	4,792	4,627	5,781	5,781	0.04
		" " with bone loss	3,792	4,792	4,627	5,781	5,781	0.04
	Stumbling	Intact	1,193	1,174	975	831	1,193	0.17
		Distal transverse fracture	5,991	7,577	7,315	9,137	9,137	0.02
		" " with bone loss	5,991	7,577	7,315	9,137	9,137	0.02
DePuy POLYAX	Standing	Intact	45	130	143	45	143	6.15
		Distal transverse fracture	497	729	671	707	729	1.21
		" " with bone loss	497	729	671	707	729	1.21
	Walking	Intact	124	370	401	126	401	2.19
		Distal transverse fracture	1,347	1,982	1,832	1,886	1,982	0.44
		" " with bone loss	1,347	1,982	1,832	1,886	1,982	0.44
	Jogging	Intact	246	718	787	249	787	1.12
		Distal transverse fracture	2,646	4,019	3,698	3,795	4,019	0.22
		" " with bone loss	2,646	4,019	3,698	3,795	4,019	0.22
	Stumbling	Intact	389	1,135	1,245	394	1,245	0.71
		Distal transverse fracture	4,193	6,282	5,807	5,996	6,282	0.14
		" " with bone loss	4,193	6,282	5,807	5,996	6,282	0.14
Medial Locking Plate	Standing	Intact	52	69	88	68	88	10.00
		Distal transverse fracture	64	91	124	105	124	7.10
		" " with bone loss	332	705	960	1,034	1,034	0.85
	Walking	Intact	146	194	247	191	247	3.56
		Distal transverse fracture	168	226	319	259	319	2.76
		" " with bone loss	-	-	-	-	-	-
	Jogging	Intact	230	326	416	322	416	2.12
		Distal transverse fracture	277	384	529	418	529	1.66
		" " with bone loss	-	-	-	-	-	-
	Stumbling	Intact	453	603	769	594	769	1.14
		Distal transverse fracture	504	669	969	773	969	0.91
		" " with bone loss	-	-	-	-	-	-

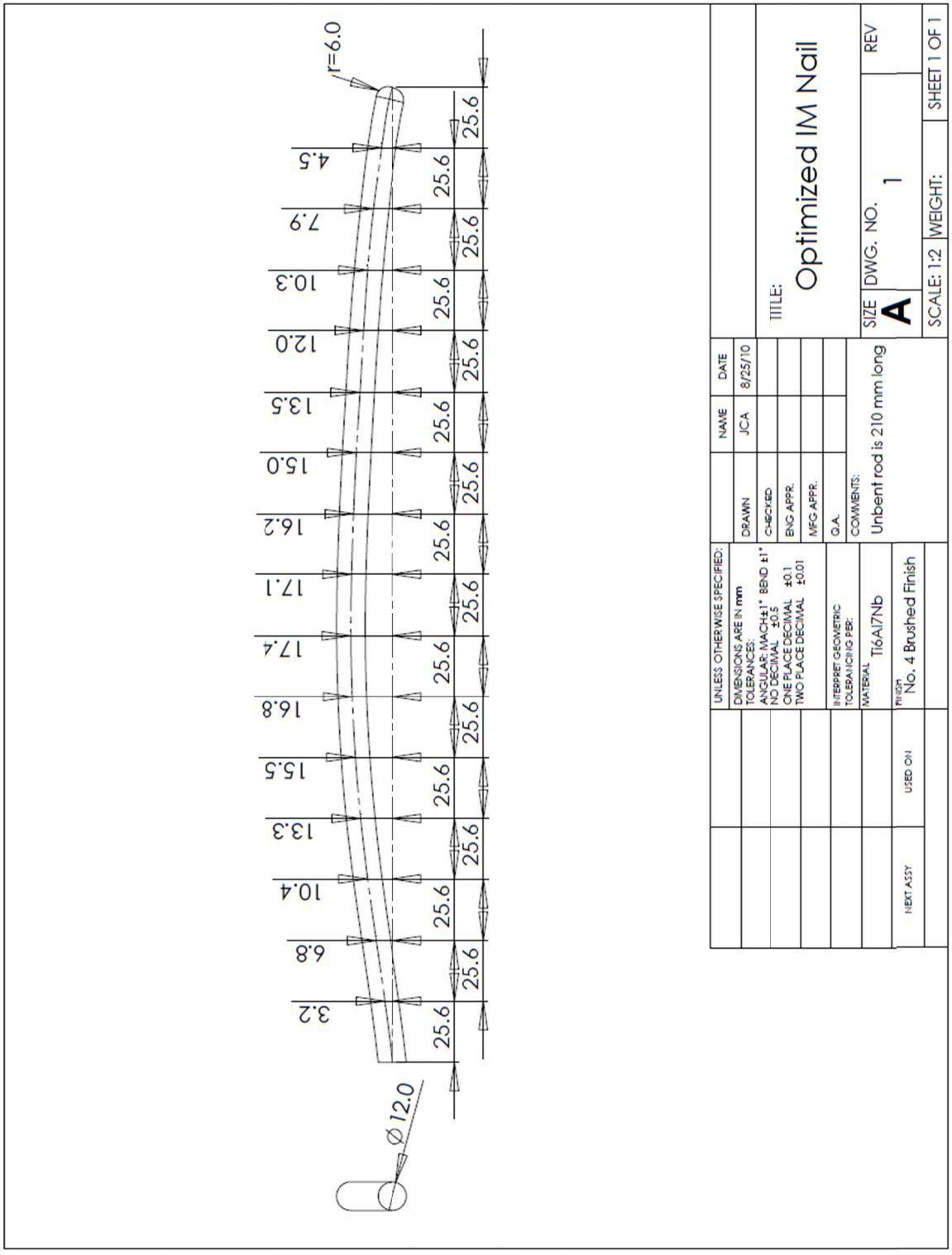

Fig. 112. IM nail prototype schematic with optimized curvature

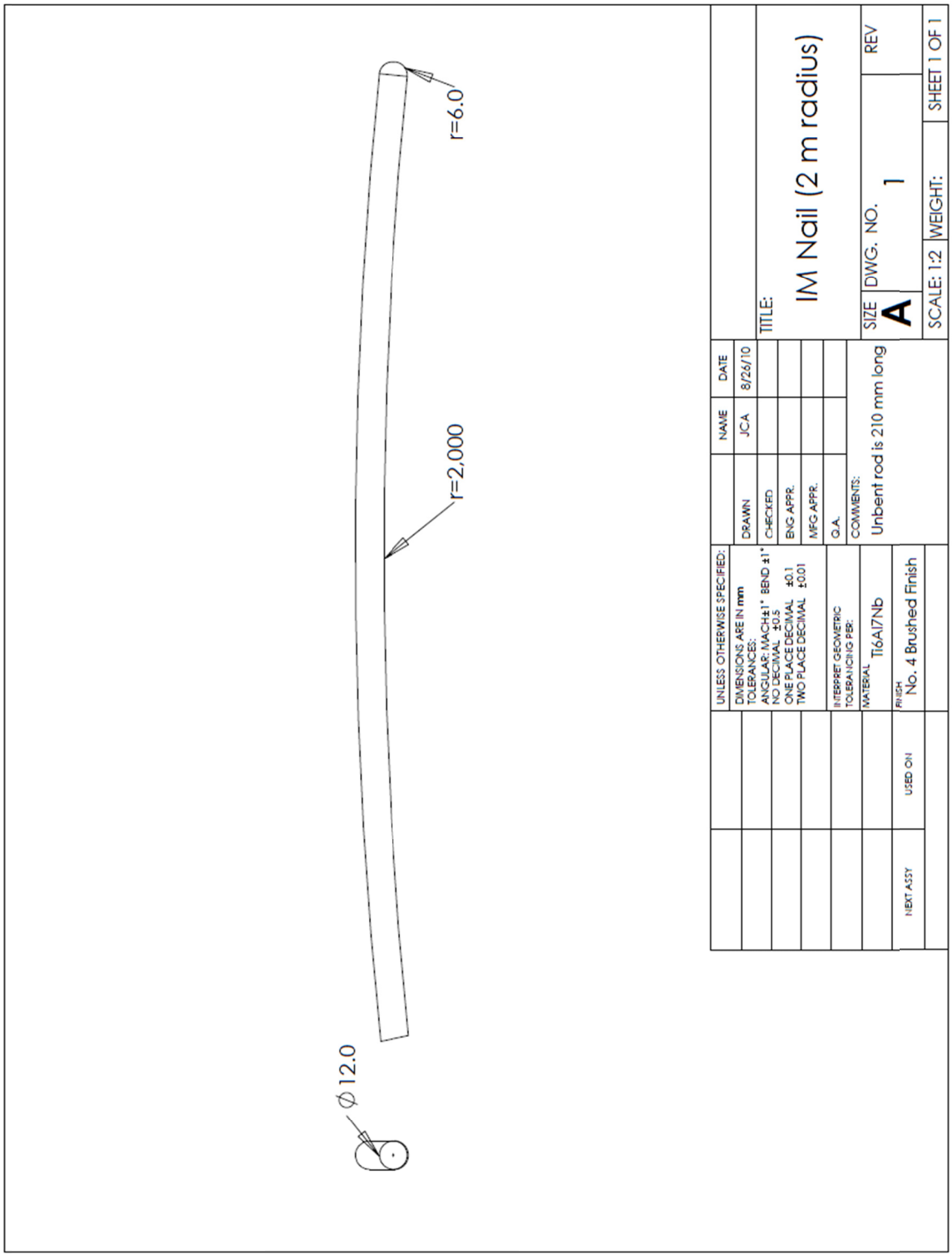

Fig. 113. IM nail prototype schematic with 2 m radius of curvature

APPENDIX B

Automated Image Segmentation Code (Matlab)

```
function varargout = Segmentator(varargin)

%  SEGMENTATOR M-file for Segmentator.fig
%      A fully-automated CT image segmentation program specific to bone CT scans.
%
%      Imports a set of DICOM files corresponding to a 3-D digital CT scan and determines the spatial
%      coordinates of voxels representing cortical and cancellous bone.  The program is unique in that the
%      surface integrity of the thin cortical walls in the proximal and distal condyles is preserved (i.e. no
%      holes or islands).

%      SEGMENTATOR, by itself, creates a new SEGMENTATOR or raises the existing
%      singleton*.
%
%      H = SEGMENTATOR returns the handle to a new SEGMENTATOR or the handle to
%      the existing singleton*.
%
%      SEGMENTATOR('CALLBACK',hObject,eventData,handles,...) calls the local
%      function named CALLBACK in SEGMENTATOR.M with the given input arguments.
%
%      SEGMENTATOR('Property','Value',...) creates a new SEGMENTATOR or raises the
%      existing singleton*.  Starting from the left, property value pairs are
%      applied to the GUI before Segmentator_OpeningFcn gets called.  An
%      unrecognized property name or invalid value makes property application
%      stop.  All inputs are passed to Segmentator_OpeningFcn via varargin.
%
%  Author: Josh Arnone
%  Date: May 6, 2010

% ------------------------------------------------------------------------ %

% Begin initialization code
gui_Singleton = 1;
gui_State = struct('gui_Name',       mfilename, ...
                   'gui_Singleton',  gui_Singleton, ...
                   'gui_OpeningFcn', @Segmentator_OpeningFcn, ...
                   'gui_OutputFcn',  @Segmentator_OutputFcn, ...
                   'gui_LayoutFcn',  [], ...
                   'gui_Callback',   []);
if nargin && ischar(varargin{1})
  gui_State.gui_Callback = str2func(varargin{1});
end

if nargout
   [varargout{1:nargout}] = gui_mainfcn(gui_State, varargin{:});
else
   gui_mainfcn(gui_State, varargin{:});
end
% End initialization code
```

```
% ------------------------------------------------------------------------ %

% --- Executes just before Segmentator is made visible.
function Segmentator_OpeningFcn(hObject, eventdata, handles, varargin)

% Choose default command line output for Segmentator
handles.output = hObject;

% Update handles structure
guidata(hObject, handles);

% ------------------------------------------------------------------------ %

% --- Outputs from this function are returned to the command line.
function varargout = Segmentator_OutputFcn(hObject, eventdata, handles)

% Get default command line output from handles structure
varargout{1} = handles.output;

% ------------------------------------------------------------------------ %

% --- Executes on button press in Generate_pushbutton.
function Generate_pushbutton_Callback(hObject, eventdata, handles)

% Set number of scan slices, pixel rows, pixel columns, and slice thickness
num_of_slices = str2num(get(handles.Slice_edit,'String'));
row_num = str2num(get(handles.RowNum_edit,'String'));
col_num = str2num(get(handles.ColNum_edit,'String'));
slice_thickness = 2;

% Set voxel intensity limits for cortical and cancellous bone
lower_limit_1 = str2num(get(handles.CorticalLowerLimit_edit,'String'));
upper_limit_1 = str2num(get(handles.CorticalUpperLimit_edit,'String'));
lower_limit_2 = str2num(get(handles.CancellousLowerLimit_edit,'String'));
upper_limit_2 = str2num(get(handles.CancellousUpperLimit_edit,'String'));

% Set cropping planes for plotting results
row_min = str2num(get(handles.RowsLowerLimit_edit,'String'));
row_max = str2num(get(handles.RowsUpperLimit_edit,'String'));
col_min = str2num(get(handles.ColumnsLowerLimit_edit,'String'));
col_max = str2num(get(handles.ColumnsUpperLimit_edit,'String'));

% Begin time counter
tic

% Open Waitbar
% h = waitbar(0,'Computing...')%,'CreateCancelBtn','setappdata(h,"canceling",1)');

% Step 1/9
% Initialize the 3D CT scan array with zeros
CT_scan = zeros(row_num, col_num, slice_thickness*num_of_slices - 1);
clf

% Import voxel intensity data from CT DICOM files into CT_scan array
```

```
disp('Importing CT scan slices (step 1 of 9)')
for ii = 1:num_of_slices
   jj = num_of_slices + 1 - ii;
   slice_num = num2str(jj);                    % Turns jj into a string
   CT_slice = sprintf('Slice%s.dcm', slice_num);   % Creates a string for current filename
   current_slice = dicomread(CT_slice);          % Load the DICOM file from current directory
   CT_scan(:,:,2*ii-1) = current_slice;          % Puts the file into a slice of CT scan matrix
end
toc
% waitbar(0.111,h)

% Initialize the 3D point cloud arrays with zeros
cortical = zeros(row_num, col_num, slice_thickness*num_of_slices-1);
cancellous = zeros(row_num, col_num, slice_thickness*num_of_slices-1);

% Step 2/9
% Begin image segmentation loop for cortical bone
disp('Segmenting cortical bone (step 2 of 9)')
for kk = 1:num_of_slices
   for jj = 1:col_num
      for ii = 1:row_num
         if ((lower_limit_1 <= CT_scan(ii,jj,slice_thickness*kk-1)) ...
         && (CT_scan(ii,jj,slice_thickness*kk-1) < upper_limit_1))
            cortical(jj,ii,slice_thickness*kk-1) = 1;
         end
      end
   end
end
toc
% waitbar(0.222,h)

% Step 3/9
% Begin image segmentation loop for cancellous bone
disp('Segmenting cancellous bone (step 3 of 9)')
for kk = 1:num_of_slices
   for jj = 1:col_num
      for ii = 1:row_num
         if ((lower_limit_2 <= CT_scan(ii,jj,slice_thickness*kk-1))) ...
         && (CT_scan(ii,jj,slice_thickness*kk-1) < upper_limit_2) ...
         && (cortical(ii,jj,2*kk-1) ~= 1)
            cancellous(jj,ii,slice_thickness*kk-1) = 1;
         end
      end
   end
end
toc
% waitbar(0.333,h)

% Step 4/9
% Begin image segmentation loops for thin, less dense, cortical walls of
% proximal and distal condyles (edge detection: user-specified contrast in
% voxel intensity)
disp('Detecting outer edges of low density cortical walls of condyles (step 4 of 9)')
cortical_temp =  zeros(row_num, col_num, slice_thickness*num_of_slices-1);
```

```
for kk = 1:num_of_slices
   for jj = 2:col_num-1
      for ii = 2:row_num-1
         if (CT_scan(ii,jj,slice_thickness*kk-1) - CT_scan(ii+1,jj,slice_thickness*kk-1)) > 300 ...
         || (CT_scan(ii,jj,slice_thickness*kk-1) - CT_scan(ii+1,jj+1,slice_thickness*kk-1)) > 300 ...
         || (CT_scan(ii,jj,slice_thickness*kk-1) - CT_scan(ii,jj+1,slice_thickness*kk-1)) > 300 ...
         || (CT_scan(ii,jj,slice_thickness*kk-1) - CT_scan(ii-1,jj+1,slice_thickness*kk-1)) > 300 ...
         || (CT_scan(ii,jj,slice_thickness*kk-1) - CT_scan(ii-1,jj,slice_thickness*kk-1)) > 300 ...
         || (CT_scan(ii,jj,slice_thickness*kk-1) - CT_scan(ii-1,jj-1,slice_thickness*kk-1)) > 300 ...
         || (CT_scan(ii,jj,slice_thickness*kk-1) - CT_scan(ii,jj-1,slice_thickness*kk-1)) > 300 ...
         || (CT_scan(ii,jj,slice_thickness*kk-1) - CT_scan(ii+1,jj-1,slice_thickness*kk-1)) > 300
            cortical_temp(jj,ii,slice_thickness*kk-1) = 1;
            cancellous(jj,ii,slice_thickness*kk-1) = 0;
         end
      end
   end
end
for kk = 1:num_of_slices
   for jj = 2:col_num-1
      for ii = 2:row_num-1
         if cortical_temp(ii,jj,slice_thickness*kk-1) == 1
            cortical(ii,jj,slice_thickness*kk-1) = 1;
         end
      end
   end
end
toc
% waitbar(0.444,h)

% Step 5/9
% Convert small cortical bone "islands" within cancellous bone region to
% cancellous bone
disp('Removing noise (step 5 of 9)')
cortical_temp =  zeros(row_num, col_num, slice_thickness*num_of_slices-1);
for nn = 1:3
   for kk = 1:num_of_slices
      for jj = 2:col_num-1
         for ii = 2:row_num-1
            if cortical(ii,jj,slice_thickness*kk-1) == 1
               cortical_count = 0;
               cancellous_count = 0;
               if cortical(ii+1,jj,slice_thickness*kk-1) == 1
                  cortical_count = cortical_count + 1; end
               if cortical(ii+1,jj+1,slice_thickness*kk-1) == 1
                  cortical_count = cortical_count + 1; end
               if cortical(ii,jj+1,slice_thickness*kk-1) == 1
                  cortical_count = cortical_count + 1; end
               if cortical(ii-1,jj+1,slice_thickness*kk-1) == 1
                  cortical_count = cortical_count + 1; end
               if cortical(ii-1,jj,slice_thickness*kk-1) == 1
                  cortical_count = cortical_count + 1; end
               if cortical(ii-1,jj-1,slice_thickness*kk-1) == 1
                  cortical_count = cortical_count + 1; end
               if cortical(ii,jj-1,slice_thickness*kk-1) == 1
```

```
                    cortical_count = cortical_count + 1; end
                if cortical(ii+1,jj-1,slice_thickness*kk-1) == 1
                    cortical_count = cortical_count + 1; end
                if cancellous(ii+1,jj,slice_thickness*kk-1) == 1
                    cancellous_count = cancellous_count + 1; end
                if cancellous(ii+1,jj+1,slice_thickness*kk-1) == 1
                    cancellous_count = cancellous_count + 1; end
                if cancellous(ii,jj+1,slice_thickness*kk-1) == 1
                    cancellous_count = cancellous_count + 1; end
                if cancellous(ii-1,jj+1,slice_thickness*kk-1) == 1
                    cancellous_count = cancellous_count + 1; end
                if cancellous(ii-1,jj,slice_thickness*kk-1) == 1
                    cancellous_count = cancellous_count + 1; end
                if cancellous(ii-1,jj-1,slice_thickness*kk-1) == 1
                    cancellous_count = cancellous_count + 1; end
                if cancellous(ii,jj-1,slice_thickness*kk-1) == 1
                    cancellous_count = cancellous_count + 1; end
                if cancellous(ii+1,jj-1,slice_thickness*kk-1) == 1
                    cancellous_count = cancellous_count + 1; end
                if cortical_count <= 3 && cancellous_count >= 5
                    cortical_temp(ii,jj,slice_thickness*kk-1) = 1;
                    cancellous(ii,jj,slice_thickness*kk-1) = 1;
                end
            end
        end
    end
    for kk = 1:num_of_slices
        for jj = 2:col_num-1
            for ii = 2:row_num-1
                if cortical_temp(ii,jj,slice_thickness*kk-1) == 1
                    cortical(ii,jj,slice_thickness*kk-1) = 0;
                end
            end
        end
    end
end
toc
% waitbar(0.555,h)

% Step 6/9
% Convert cancellous bone voxels that are adjacent to cortical bone to
% cortical bone
disp('Removing holes in cortical wall - method 1 (step 6 of 9)')
cortical_temp =  zeros(row_num, col_num, slice_thickness*num_of_slices-1);
for kk = 1:num_of_slices
    for jj = 2:col_num-1
        for ii = 2:row_num-1
            if cancellous(ii,jj,slice_thickness*kk-1) == 1
                if (cortical(ii+1,jj,slice_thickness*kk-1) == 1 ...
                || cortical(ii+1,jj+1,slice_thickness*kk-1) == 1 ...
                || cortical(ii,jj+1,slice_thickness*kk-1) == 1 ...
                || cortical(ii-1,jj+1,slice_thickness*kk-1) == 1 ...
                || cortical(ii-1,jj,slice_thickness*kk-1) == 1 ...
```

```
            || cortical(ii-1,jj-1,slice_thickness*kk-1) == 1 ...
            || cortical(ii,jj-1,slice_thickness*kk-1) == 1 ...
            || cortical(ii+1,jj-1,slice_thickness*kk-1) == 1)
               cortical_temp(ii,jj,slice_thickness*kk-1) = 1;
               cancellous(ii,jj,slice_thickness*kk-1) = 0;
            end
         end
      end
   end
end
for kk = 1:num_of_slices
   for jj = 2:col_num-1
      for ii = 2:row_num-1
         if cortical_temp(ii,jj,slice_thickness*kk-1) == 1
            cortical(ii,jj,slice_thickness*kk-1) = 1;
         end
      end
   end
end
toc
% waitbar(0.666,h)

% Step 7/9
% Fill in holes within cancellous bone (due to bone density variation)
disp('Removing holes within cancellous bone (step 7 of 9)')
cancellous_temp =  zeros(row_num, col_num, slice_thickness*num_of_slices-1);
for nn = 1:5
   for kk = 1:num_of_slices
      for jj = 2:col_num-1
         for ii = 2:row_num-1
            if cortical(ii,jj,slice_thickness*kk-1) == 0 ...
            && cancellous(ii,jj,slice_thickness*kk-1) == 0
               cancellous_count = 0;
               if cancellous(ii+1,jj,slice_thickness*kk-1) == 1
                  cancellous_count = cancellous_count + 1; end
               if cancellous(ii+1,jj+1,slice_thickness*kk-1) == 1
                  cancellous_count = cancellous_count + 1; end
               if cancellous(ii,jj+1,slice_thickness*kk-1) == 1
                  cancellous_count = cancellous_count + 1; end
               if cancellous(ii-1,jj+1,slice_thickness*kk-1) == 1
                  cancellous_count = cancellous_count + 1; end
               if cancellous(ii-1,jj,slice_thickness*kk-1) == 1
                  cancellous_count = cancellous_count + 1; end
               if cancellous(ii-1,jj-1,slice_thickness*kk-1) == 1
                  cancellous_count = cancellous_count + 1; end
               if cancellous(ii,jj-1,slice_thickness*kk-1) == 1
                  cancellous_count = cancellous_count + 1; end
               if cancellous(ii+1,jj-1,slice_thickness*kk-1) == 1
                  cancellous_count = cancellous_count + 1; end
               if cancellous_count >= 4
                  cancellous_temp(ii,jj,slice_thickness*kk-1) = 1;
               end
            end
         end
```

```
        end
    end
    for kk = 1:num_of_slices
        for jj = 2:col_num-1
            for ii = 2:row_num-1
                if cancellous_temp(ii,jj,slice_thickness*kk-1) == 1
                    cancellous(ii,jj,slice_thickness*kk-1) = 1;
                end
            end
        end
    end
end
toc
% waitbar(0.777,h)

% Step 8/9
% Convert cancellous bone voxels that are exposed to the outer bone surface
% to cortical bone
disp('Removing holes in cortical walls - method 2 (step 8 of 9)')
cortical_temp =  zeros(row_num, col_num, slice_thickness*num_of_slices-1);
for nn = 1:3
    for kk = 1:num_of_slices
        for jj = 2:col_num-1
            for ii = 2:row_num-1
                if cancellous(ii,jj,slice_thickness*kk-1) == 1
                    cortical_count = 0;
                    empty_count = 0;
                    if cortical(ii+1,jj,slice_thickness*kk-1) == 1
                        cortical_count = cortical_count + 1; end
                    if cortical(ii+1,jj+1,slice_thickness*kk-1) == 1
                        cortical_count = cortical_count + 1; end
                    if cortical(ii,jj+1,slice_thickness*kk-1) == 1
                        cortical_count = cortical_count + 1; end
                    if cortical(ii-1,jj+1,slice_thickness*kk-1) == 1
                        cortical_count = cortical_count + 1; end
                    if cortical(ii-1,jj,slice_thickness*kk-1) == 1
                        cortical_count = cortical_count + 1; end
                    if cortical(ii-1,jj-1,slice_thickness*kk-1) == 1
                        cortical_count = cortical_count + 1; end
                    if cortical(ii,jj-1,slice_thickness*kk-1) == 1
                        cortical_count = cortical_count + 1; end
                    if cortical(ii+1,jj-1,slice_thickness*kk-1) == 1
                        cortical_count = cortical_count + 1; end
                    if cancellous(ii+1,jj,slice_thickness*kk-1) == 0 ...
                    && cortical(ii+1,jj,slice_thickness*kk-1) == 0
                        empty_count = empty_count + 1; end
                    if cancellous(ii+1,jj+1,slice_thickness*kk-1) == 0 ...
                    && cortical(ii+1,jj+1,slice_thickness*kk-1) == 0
                        empty_count = empty_count + 1; end
                    if cancellous(ii,jj+1,slice_thickness*kk-1) == 0 ...
                    && cortical(ii,jj+1,slice_thickness*kk-1) == 0
                        empty_count = empty_count + 1; end
                    if cancellous(ii-1,jj+1,slice_thickness*kk-1) == 0 ...
                    && cortical(ii-1,jj+1,slice_thickness*kk-1) == 0
```

```
                    empty_count = empty_count + 1; end
                if cancellous(ii-1,jj,slice_thickness*kk-1) == 0 ...
                && cortical(ii-1,jj,slice_thickness*kk-1) == 0
                    empty_count = empty_count + 1; end
                if cancellous(ii-1,jj-1,slice_thickness*kk-1) == 0 ...
                && cortical(ii-1,jj-1,slice_thickness*kk-1) == 0
                    empty_count = empty_count + 1; end
                if cancellous(ii,jj-1,slice_thickness*kk-1) == 0 ...
                && cortical(ii,jj-1,slice_thickness*kk-1) == 0
                    empty_count = empty_count + 1; end
                if cancellous(ii+1,jj-1,slice_thickness*kk-1) == 0 ...
                && cortical(ii+1,jj-1,slice_thickness*kk-1) == 0
                    empty_count = empty_count + 1; end
                if cortical_count >= 1 && empty_count >= 1
                    cortical_temp(ii,jj,slice_thickness*kk-1) = 1;
                    cancellous(ii,jj,slice_thickness*kk-1) = 0;
                end
            end
        end
    end
    for kk = 1:num_of_slices
        for jj = 2:col_num-1
            for ii = 2:row_num-1
                if cortical_temp(ii,jj,slice_thickness*kk-1) == 1
                    cortical(ii,jj,slice_thickness*kk-1) = 1;
                end
            end
        end
    end
end
toc
% waitbar(0.888,h)

% Step 9/9
% Plot cropped 3D point cloud of cortical and cancellous bone
disp('Plotting cortical and cancellous bone point clouds (step 9 of 9)')
figure(1)
hold;
axis([row_min row_max col_min col_max 5 slice_thickness*248-1]);
view(20,20)
for kk = 1:num_of_slices
    for jj = col_min:col_max
        for ii = row_min:row_max
            if cortical(ii,jj,slice_thickness*kk-1) == 1
                plot3(ii,jj,slice_thickness*kk-1);
            end
            if cancellous(ii,jj,slice_thickness*kk-1) == 1
                plot3(ii,jj,slice_thickness*kk-1,'r');
            end
        end
    end
end
hold;
```

```
% End time counter
toc
% waitbar(1,h)
% setappdata(h,'Canceling...',0)
% close(h)

% --------------------------------------------------------------------- %

% Set user-defined "number of slices" as a variable
function Slice_edit_Callback(hObject, eventdata, handles)

num_of_slices = str2num(get(hObject,'String'));

if(isempty(num_of_slices))
   set(hObject,'String',259);
end

guidata(hObject,handles);


% --- Executes during object creation, after setting all properties.
function Slice_edit_CreateFcn(hObject, eventdata, handles)

if ispc && isequal(get(hObject,'BackgroundColor'), get(0,'defaultUicontrolBackgroundColor'))
   set(hObject,'BackgroundColor','white');
end

% --------------------------------------------------------------------- %

% Set user-defined "number of columns" as a variable
function ColNum_edit_Callback(hObject, eventdata, handles)

col_num = str2num(get(hObject,'String'));

if(isempty(col_num))
   set(hObject,'String',512);
end

guidata(hObject,handles);


% --- Executes during object creation, after setting all properties.
function ColNum_edit_CreateFcn(hObject, eventdata, handles)

if ispc && isequal(get(hObject,'BackgroundColor'), get(0,'defaultUicontrolBackgroundColor'))
   set(hObject,'BackgroundColor','white');
end

% --------------------------------------------------------------------- %

% Set user-defined "number of rows" as a variable
function RowNum_edit_Callback(hObject, eventdata, handles)
```

```
row_num = str2num(get(hObject,'String'));

if(isempty(row_num))
   set(hObject,'String',512);
end
guidata(hObject,handles);


% --- Executes during object creation, after setting all properties.
function RowNum_edit_CreateFcn(hObject, eventdata, handles)

if ispc && isequal(get(hObject,'BackgroundColor'), get(0,'defaultUicontrolBackgroundColor'))
   set(hObject,'BackgroundColor','white');
end

% ------------------------------------------------------------------------ %

% Set user-defined "lower voxel intensity limit for cancellous bone" as a
% variable
function CancellousLowerLimit_edit_Callback(hObject, eventdata, handles)

lower_limit_2 = str2num(get(hObject,'String'));

if(isempty(lower_limit_2))
   set(hObject,'String',-800);
end

guidata(hObject,handles);


% --- Executes during object creation, after setting all properties.
function CancellousLowerLimit_edit_CreateFcn(hObject, eventdata, handles)

if ispc && isequal(get(hObject,'BackgroundColor'), get(0,'defaultUicontrolBackgroundColor'))
   set(hObject,'BackgroundColor','white');
end

% ------------------------------------------------------------------------ %

% Set user-defined "upper voxel intensity limit for cancellous bone" as a
% variable
function CancellousUpperLimit_edit_Callback(hObject, eventdata, handles)

upper_limit_2 = str2num(get(hObject,'String'));

if(isempty(upper_limit_2))
   set(hObject,'String',0);
end

guidata(hObject,handles);


% --- Executes during object creation, after setting all properties.
function CancellousUpperLimit_edit_CreateFcn(hObject, eventdata, handles)
```

```
if ispc && isequal(get(hObject,'BackgroundColor'), get(0,'defaultUicontrolBackgroundColor'))
    set(hObject,'BackgroundColor','white');
end

% --------------------------------------------------------------------

% Set user-defined "lower voxel intensity limit for cortical bone" as a
% variable
function CorticalLowerLimit_edit_Callback(hObject, eventdata, handles)

lower_limit_1 = str2num(get(hObject,'String'));

if(isempty(lower_limit_1))
    set(hObject,'String',0);
end

guidata(hObject,handles);


% --- Executes during object creation, after setting all properties.
function CorticalLowerLimit_edit_CreateFcn(hObject, eventdata, handles)

if ispc && isequal(get(hObject,'BackgroundColor'), get(0,'defaultUicontrolBackgroundColor'))
    set(hObject,'BackgroundColor','white');
end

% --------------------------------------------------------------------

% Set user-defined "upper voxel intensity limit for cortical bone" as a
% variable
function CorticalUpperLimit_edit_Callback(hObject, eventdata, handles)

upper_limit_1 = str2num(get(hObject,'String'));

if(isempty(upper_limit_1))
    set(hObject,'String',2000);
end

guidata(hObject,handles);


% --- Executes during object creation, after setting all properties.
function CorticalUpperLimit_edit_CreateFcn(hObject, eventdata, handles)

if ispc && isequal(get(hObject,'BackgroundColor'), get(0,'defaultUicontrolBackgroundColor'))
    set(hObject,'BackgroundColor','white');
end

% --------------------------------------------------------------------

% Set user-defined "column lower limit" (for cropping) as a variable
function ColumnsLowerLimit_edit_Callback(hObject, eventdata, handles)
```

```
col_min = str2num(get(hObject,'String'));

if(isempty(col_min))
   set(hObject,'String',0);
end

guidata(hObject,handles);


% --- Executes during object creation, after setting all properties.
function ColumnsLowerLimit_edit_CreateFcn(hObject, eventdata, handles)

if ispc && isequal(get(hObject,'BackgroundColor'), get(0,'defaultUicontrolBackgroundColor'))
   set(hObject,'BackgroundColor','white');
end

% ------------------------------------------------------------------- %

% Set user-defined "column upper limit" (for cropping) as a variable
function ColumnsUpperLimit_edit_Callback(hObject, eventdata, handles)

col_max = str2num(get(hObject,'String'));

if(isempty(col_max))
   set(hObject,'String',512);
end

guidata(hObject,handles);

% --- Executes during object creation, after setting all properties.
function ColumnsUpperLimit_edit_CreateFcn(hObject, eventdata, handles)

if ispc && isequal(get(hObject,'BackgroundColor'), get(0,'defaultUicontrolBackgroundColor'))
   set(hObject,'BackgroundColor','white');
end

% ------------------------------------------------------------------- %

% Set user-defined "row lower limit" (for cropping) as a variable
function RowsLowerLimit_edit_Callback(hObject, eventdata, handles)

row_min = str2num(get(hObject,'String'));

if(isempty(row_min))
   set(hObject,'String',0);
end

guidata(hObject,handles);


% --- Executes during object creation, after setting all properties.
function RowsLowerLimit_edit_CreateFcn(hObject, eventdata, handles)

if ispc && isequal(get(hObject,'BackgroundColor'), get(0,'defaultUicontrolBackgroundColor'))
```

```
    set(hObject,'BackgroundColor','white');
end

% ------------------------------------------------------------------- %

% Set user-defined "crop upper limit" (for cropping) as a variable
function RowsUpperLimit_edit_Callback(hObject, eventdata, handles)

row_max = str2num(get(hObject,'String'));

if(isempty(row_max))
    set(hObject,'String',512);
end

guidata(hObject,handles);


% --- Executes during object creation, after setting all properties.
function RowsUpperLimit_edit_CreateFcn(hObject, eventdata, handles)

if ispc && isequal(get(hObject,'BackgroundColor'), get(0,'defaultUicontrolBackgroundColor'))
    set(hObject,'BackgroundColor','white');
end
```

VITA

Josh Arnone was born in Independence, Missouri, on August 15th, 1984, the son of Larry and Susan Arnone. After completing high school at Oak Grove High School, Oak Grove, Missouri in 2003, he attended the University of Missouri in Columbia, Missouri from 2003-2011. He graduated with a Bachelor of Science degree in mechanical engineering in 2007, and in 2011 he graduated with a Doctor of Philosophy degree in mechanical engineering with an emphasis in biomechanical engineering.

BIBLIOGRAPHY

1. Gelaude, F., Vander Sloten, J., Lauwers, B., 2008, "Accuracy Assessment of CT-Based Outer Surface Femur Meshes," *Computer-Aided Surgery*, **13**, 188–199
2. Benameur, S., Mignotte, M., Labelle, H., De Guise, J.A., 2005, "A Hierarchical Statistical Modeling Approach for the Unsupervised 3-D Biplanar Reconstruction of the Scoliotic Spine," *IEEE Transactios on Biomedical Engineering*, **52**, 2041-2057
3. Zheng, G., Schumann, S., 2009, " 3D Reconstruction of a Patient-Specific Surface Model of the Proximal Femur from Calibrated X-Ray Radiographs: A validation Study," *Medical Physics*," **36**, 1155-1166
4. Mitton, D., Landry, C., Vuron, S., Skalli, W., Laveste, F., De Guise, J.A., 200, "3D Reconstruction Method from Biplanar Radiography Using Non-Stereocorresponding Points and Elastic Deformable Meshes," *Medical Biological Engineering and Computing*, **38**, 133-139
5. Schmutz, B., Reynolds, K.J., Slavotinek, J.P., 2006, "Development and Validation of a Generic 3D Model of the Distal Femur," *Computational Methods in Biomechanics*," **9**, 305-312
6. Cerveri, P., Marchente, M., Bartels, W., Corten, K., Simon, J.P., Manzotti, A., 2010, "Automated Method for Computing the Morphological and Clinical Parameters of the Proximal Femur Using Heuristic Modeling Techniques," *Annals of Biomedical Engineering*, **38**, 1752-1766

7. Ryu, J.H., Kim, H.S., Lee, K.H., 2004, “Contour-Based Algorithms for Generating 3D CAD Models from Medical Images,” *International Journal of Advanced Manufacturing Technology*, **24**, 112-119
8. Goh, J.C.H., Lee, P.V.S., Toh, S.L., Ooi, C.K., 2005, “Development of an Integrated CAD-FEA Process for Below-Knee Prosthetic Sockets,” *Clinical Biomechanics*, **20**, 623-629
9. Ciocca, L., De Crescenzio, F., Fantini, M., Scotti, R., 2009, “CAD/CAM and Rapid Prototyped Scaffold Construction for Bone Regenerative Medicine and Surgical Transfer of Virtual Planning: A Pilot Study,” *Computerized Medical Imaging and Graphics*, **33**, 58-62
10. Kidder, J., Mason, E., Nnaji, B.O., 1996, “3-D Model Acquisition, Design, Planning and Manufacturing of Orthopaedic Implants: A Framework,” *SPIE*, **2911**, 9-22
11. Lorensen, W.E., Cline, H.E., 1987, “Marching Cubes: A High Resolution 3D Surface Construction Algorithm,” *ACM SIGGRAPH Computer Graphics*, **21**, 163-169
12. Newman, T.S., Yi, H., 2006, “A Survey of the Marching Cubes Algorithm,” *Computers & Graphics*, **30**, 854-879
13. Lockwood, C.A., Lynch, J.M., Kimbel, W.H., 2002, “Quantifying Temporal Bone Morphology of Great Apes and Humans: An Approach Using Geometric Morphometrics,” *Journal of Anatomy*, **201**, 447–464
14. Gargouri, I., De Guise, J.A., 2007, “Automated Method for Clinic and Morphologic Analysis of Bones Using Implicit Modeling Technique,” Conf. Proc. IEEE Eng. Med. Biol.. 5095–5098

15. Kim, J.S., Park, T.S., Park, S.B., Kim, J.S., Kim, I.Y., Kim, S.I., 2000, “Measurement of Femoral Neck in 3D, Part 1: 3D Imaging Method” *Medical Biological Engineering and Computing*, **38**, 603–609
16. Kim, J.S., Park, T.S., Park, S.B., Kim, J.S., Kim, I.Y., Kim, S.I., 2000, “Measurement of Femoral Neck in 3D, Part 2: 3D Modeling Method” *Medical Biological Engineering and Computing*, **38**, 610–616
17. Laporte, S., Skalli, W., De Guise, J.A., Lavaste, F., Mitton, D., 2003, “A 3D Reconstruction Method for Stereoradiography Based on 2D and 3D Contours: Application to the Distal Femur,” *Computer Methods in Biological Engineering*, **6,** 1–6
18. Le Bras, A., Laporte, S., Bousson, V., Mitton, D., De Guise, J.A., Laredo, J.D., Skalli, W., 2004, “3D Reconstruction of the Proximal Femur with Low-Dose Digital Stereoradiography,” *Computer-Aided Surgery*, **9**, 51–57
19. Sugano, N., Noble, P.C., Kamaric, A., 1998, “A Comparison of Alternative Methods of Measuring Femoral Anteversion,” *Journal of Computer Assisted Tomography*,” **22**, 610–614
20. Worz, S., Rohr, K., 2006, “Localization of Anatomical Point Landmarks in 3D Medical Images by Fitting 3D Parametric Intensity Models,” *Medical Imaging Analysis*, **10**, 41–58
21. Eberly, D., 1996, *Ridges in Image and Data Analysis*, Kluwer Academic Publishers, Dordrecht

22. Atkins, M.S., Mackiewich, B.T., 1998, “Fully Automatic Segmentation of the Brain in MRI,” IEEE Trans Medical Imaging, **17**, 98–107

23. Zhu, Y., Yan, H., 1997, “Computerized Tumor Boundary Detection Using a Hopfield Neural Network,” IEEE Trans Medical Imaging, **16**, 55–67

24. Lee, H.H., 2010, *Finite Element Simulations with ANSYS Workbench 12: Theory, Applications, & Case Studies*, Schroff Development Corporation, Mission

25. Brekelmans, W.A.M., Poort, H.W., Sloof, T.J.J.H., 1972, “A New Method to Analyze the Mechanical Behaviour of Skeletal Parts,” *Acta Orthopaedica Scandinavica*, **43**, 301-317

26. Kluess, D., Souffrant, R., Mittelmeier, W., Wree, A., Klaus-Peter, S., Bader, R., 2009, “A Convenient Approach for Finite-Element-Analyses of Orthopaedic Implants in Bone Contact: Modeling and Experimental Validation,” *Computer Methods and Programs in Biomedicine*, **95**, 23-30

27. Chui, C.K., Wang, Z., Zhang, J., Ong, J.S.K., Bian, L., Teo, J.C.M., Yan, C.H., Ong, S.H., Wang, S.C., Wong, H.K., Teoh, S.H., 2009, “A Component-Oriented Software Toolkit for Patient-Specific Finite Element Model Generation,” *Advances in Engineering Software*, **40**, 184-192

28. Langton, C.M., Pisharody, S., Keyak, J.H., 2009, “Comparison of 3D Finite Element Analysis Derived Stiffness and BMD to Determine the Failure Load of the Excised Proximal Femur,” *Medical Engineering & Physics*, **31**, 668-672

29. Viceconti, M., Davinelli, M., Taddei, F., Capello, A., 2004, “Automatic Generation of Accurate Subject-Specific Bone Finite Element Models to be Used in Clinical Studies,” *Journal of Biomechanics*, **37**, 1597-1605

30. Towfighian, S., Behdinan, K., Papini, M., Saghir, Z., Zalzal, P., de Beer, J., 2008, “Finite Element Modeling of Low-Speed Femur Reaming Using Reamers with Irregular Tooth Spacing,” *Journal of Sound and Vibration*, **318**, 868-883

31. Gefen, A., 2002, “Computational Simulations of Stress Shielding and Bone Resorption Around Existing and Computer-Designed Orthopaedic Screws,” *Medical and Biological Engineering and Computing*, **40**, 311-322

32. Shivanna, K.H., Tadepalli, S.C., Grosland, N.M., 2010, “Feature-Based Multiblock Finite Element Mesh Generation,” *Computer Aided Design*, **42**, 1108-1116

33. Easley, S.K., Pal, S., Tomaszewski, P.R., Petrella, A.J., Rullkoetter, P.J., Laz, P.J., 2007, “Finite Element-Based Probabilistic Analysis Tool for Orthopaedic Applications,” *Computer Methods and Programs in Biomedicine*, **85**, 32-40

34. Lennon, A.B., Prendergast, P.J., 2001, “Evaluation of Cement Stresses in Finite Element Analyses of Cemented Orthopaedic Implants,” *Journal of Biomechanical Engineering*, **123**, 623-628

35. Huiskes, R., Chao, E.Y.S., 1983, “A Survey of Finite Element Analysis in Orthopedic Biomechanics: The First Decade,” *Journal of Biomechanics*, **16**, 385-409

36. Keyak, J.H., Meagher, Skinner, H.B., Mote, C.D., 1990, “Automated Three Dimensional Finite Element Modeling of Bone: A New Method,” *Journal of Biomedical Engineering*, **12**, 389-397

37. Anderson, A.E., Peters, C.L., Tuttle, B.D., Weiss, J.A., 2005, “Subject-Specific Finite Element Model of the Pelvis: Development, Validation and Sensitivity Studies, *Journal of Biomechanical Engineering*, **127**,364–373

38. Bachtar, F., Chen, X., Hisada, T., 2006, “Finite Element Contact Analysis of the Hip Joint, *Medical and Biological Engineering and Computing*, **44**, 643–651

39. Dalstra, M., Huiskes, R., van Erning, L., 1995, “Development and Validation of a Three-Dimensional Finite Element Model of the Pelvic Bone,” *Journal of Biomechanical Engineering*, **117**, 272–278

40. Dalstra, M., Huiskes, R., 1995, “Load Transfer Across the Pelvic Bone,” *Journal of Biomechanical Engineering*, **28**, 715–724

41. Dawson, J.M., Khmelniker, B.V., McAndrew, M.P., 1999, “Analysis of the Structural Behavior of the Pelvis During Lateral Impact Using the Finite Element Method,” *Accident Analysis and Prevention*, 31, 109–119

42. Garcia, J.M., Doblare, M., Seral, B., Seral, F., Palanca, D., Gracia, L., 2000, “Three-Dimensional Finite Element Analysis of Several Internal and External Pelvis Fixations,” *Journal of Biomechanical Engineering*, **122**, 516–522

43. Kaku, N., Tsumura, H., Taira, H., Sawatari, T., Torisu, T., 2004, “Biomechanical Study of Load Transfer of the Pubic Ramus Due to Pelvic Inclination After Hip Joint Surgery Using a Three-Dimensional Finite Element Model, *Journal of Orthopaedic Science*, **9**, 264–269

44. Kluess, D., Martin, H., Mittelmeier, W., Schmitz, K., Bader, R., 2007, “Finite-Element-Analysis into Impingement-Related Implant Failure of Total Hip Replacement,” *Mater. Test.*, **49**, 330–336

45. Kluess, D., Martin, H., Mittelmeier, W., Schmitz, K., Bader, R., 2007, “Influence of Femoral Head Size on Impingement, Dislocation and Stress Distribution in Total Hip Replacement,” *Medical Engineering & Physics*, **29**, 465–471

46. Schultze, W., Kluess, Martin, D., Hingst, V., Mittelmeier, W., Schmitz, K.P., Bader, R., 2007, “Finite Element Analysis of a Cemented Ceramic Femoral Component for the Real Assembly Situation in Total Knee Arthroplasty,” *Biomedical Technology (Berlin)*, **52**, 301–307

47. Spears, J.R., Pfleiderer, M., Schneider, E., Hille, E., Morlock, M.M., 2001, “The Effect of Interfacial Parameters on Cup-Bone Relative Micromotions. A Finite Element Investigation,” *Journal of Biomechanical Engineering*, 34, 113–120

48. Manley, M.T., Ong, K.L., Kurtz, S.M., 2006, “The Potential for Bone Loss in Acetabular Structures Following THA,” *Clinical Orthopaedics and Related Research*, **453**, 246–253

49. Oki, H., Ando, M., Omori, H., Okumura, Y., Negoro, K., Uchida, K., Baba, H., 2004, “Relation Between Vertical Orientation and Stability of Acetabular Component in the Dysplastic Hip Simulated by Nonlinear Three-Dimensional Finite Element Method,” *International Journal of Artificial Organs*, **28**, 1050–1054

50. Thompson, M.S., Northmore-Ball, M.D., Tanner, K.E., 2002, “Effects of Acetabular Resurfacing Component Material and Fixation on the Strain Distribution in the Pelvis, *Proceedings of the Institution of Mechanical Engineers [H]*, **216**, 237–245
51. Rho, J.Y., Hobatho, M.C., Ashman, R.B., 1995, “Relations of Mechanical Properties to Density and CT Numbers in Human Bone, *Medical Engineering & Physics*, **17**, 347–355
52. Snyder, S.M., Schneider, E., 1991, “Estimation of Mechanical Properties of Cortical Bone by Computed Tomography,” *Journal of Orthopaedic Research*, **9**, 422–431
53. Wall, W.A., Frenzel, M.A., Cyron, C., 2008, “Isogeometric Structural Shape Optimization,” *Computer Methods in Applied Mechanics and Engineering*, **197**, 2976-2988`
54. Annicchiarico, W., Cerrolaza, M., 2001, “Structural Shape Optimization 3D Finite-Element Models Based on Genetic Algorithms and Geometric Modeling,” *Finite Elements in Analysis and Design*, **37**, 403-415
55. Bennet, J., Botkin, M., 1984, “Structural Shape Optimization with Geometric Problem Description and Adaptive Mesh Refinement,” *AIAA Journal*, **23**, 458–464
56. Kurowski, P.M., 2010, *Engineering Analysis with SolidWorks Simulation 2010*, Schroff Development Corporation, Mission
57. Shih, R.H., 2009, *Introduction to Finite Element Analysis: Using Pro/Mechanica Wildfire 5.0*, Schroff Development Corporation, Mission
58. Lagaros, N.D., Papadrakakis, M., Kokossalakis, G., 2002, “Structural Optimization Using Evolutionary Algorithms,” *Computers & Structures*, **80**, 571-589

59. Almeida, F.S., Awruch, A.M., 2009, “Design Optimization of Composite Laminated Structures Using Genetic Algorithms and Finite Element Analysis,” *Composite Structures*, **88**, 443-454

60. Liu, X., Yi, W.J., Li, Q.S., Shen, P.S., 2007, “Genetic Evolutionary Structural Optimization,” *Journal of Constructional Steel Research*, **64**, 305-311

61. Calvel, S., Mongeau, M., 2007, “Black-Box Structural Optimization of a Mechanical Component,” *Computers and Industrial Engineering*, **53**, 514-530

62. Bruns, T.E., 2007, “Topology Optimization by Penalty (TOP) Method,” *Computer Methods in Applied Mechanics and Engineering*, **196**, 4430-4443

63. Wang, S., Wang, M.Y., 2006, “A Moving Superimposed Finite Element Method for Structural Topology Optimization,” *International Journal for Numerical Methods in Engineering*,” **65**, 1892-1922

64. Kayabasi, O., Ekici, B., 2006, “The Effects of Static, Dynamic, and Fatigue Behavior on Three-Dimensional Shape Optimization of Hip Prosthesis by Finite Element Method,” *Materials & Design*, **28**, 2269-2277

65. Gefen, A., 2002, “Optimizing the Biomechanical Compatibility of Orthopedic Screws for Bone Fracture Fixation,” *Medical Engineering and Physics*, **24**, 337-347

66. Gerhart, T., Hayes, W.C., Stern, S.H., 1986, “Biomechanical Optimization of a Model Particulate Composite for Orthopaedic Applications,” *Journal of Orthopaedic Research*, **4**, 76-85

67. Ueda, T., Wada, A., Hasegawa, K., Endo, Y., Takikawa, Y., Hasegawa, T., Hara, T., 2010, “Design Optimization of Surgical Drills Using the Taguchi Method,” *Journal of Biomechanical Science and Engineering*, **5**, 603-614

68. Goyal, K.S., Skalak, A.S., Marcus, R.E., Vallier, H.A., Cooperman, D.R., 2007, “Analysis of Anatimic Periarticular Tibial Plate Fit on Normal Adults,” *Clinical Orthopaedics and Related Research*, **461**, 245-257

69. Schmutz, B., Wullschleger, M.E., Kim, H., Noser, H., Schütz, M.A., 2008, “Fit Assessment of Anatomic Plates for the Distal Medial Tibia,” *Journal of Orthopaedic Trauma*, **22**, 258-263

70. Kozic, N., Weber, S., Büchler, P., Lutz, C., Reimers, N., Ballester, M.Á.G., Reyes, M., 2010, “Optimization of Orthopaedic Implant Design Using Statistical Shape Space Analysis Based on Level Sets,” *Medical Image Analysis*, **14**, 265-275

71. Nowak, M., 2006, “Structural Optimization System Based on Trabecular Bone Surface Adaptation,” *Struct. Multidisc. Optim.*, **32**, 241-249

72. Harrigan, T.P., Hamilton, J.J., 1994, “Bone Remodeling and Structural Optimization,” *Journal of Biomechanics*, **27**, 323-328

73. Dee, R., Hurst, L.C., Gruber, M.A., Kottmeier, S.A., 1997, *Principals of Orthopaedic Practice*, McGraw-Hill, New York, 27-28

74. Black, J., Hastings, G., 1998, Handbook of Biomaterial Properties, Chapman & Hall, London

75. Mow, V.C., Huiskes, R., 2005, Basic Orthopedic Biomechanics and Mechano-Biology, Lippincott Williams & Wilkins, Philadelphia, 135-139

76. Bredbenner, T.,L., Snyder, S.A., Mazloomi, F.R., Le, T., Wilber, R.G., 2005, "Subtrochanteric Fixation Stability Depends on Discrete Fracture Surface Points," *Clinical Orthopaedics and Related Research*, **432**, 217-225

77. Crist, B.D., Dart, B.R., Czuwala, P.J., Olney, B.W., Pence, C.D, 2006 "Using Flexible Nails to Improve Stabilization of Proximal Femur Fractures in Adolescents," *American Journal of* Orthopaedics, **1**, 37-41

78. Cusick, R.P., Lucas, G.L., McQueen, D.A., Graber, C.D., 2000, "Construct Stiffness of Different Fixation Methods for Supracondylar Femoral Fractures above Total Knee Prostheses," *American Journal of Orthopaedics*, **29**, 695-699

79. Farooq, M.A., Clements, J.P., Miles, A.W., 2006 "In Vitro Monitroing of Hoop Strains during Impaction Grafting of the Femur," *Hip International*, **16**, 223-231

80. Cristofolini, L., Cappello, A., McNamara, B.P., Viceconti, M, 1996 "A Minimal Parametric Model of the Femur to Describe Axial Elastic Strain in Response to Loads," *Medical Engineering and Physics*, **18**, 502-14

81. Firoozbakhsh, K., Behzadi, K., DeCoster, T.A., Moneim, M.S., Naraghi, F.F., 1995, "Mechanics of Retrograde Nail versus Plate Fixation for Supracondylar Femur Fractures," *Journal of Orthopaedic Trauma*, **9**, 152-157

82. Fujishiro, T., Nishikawa, T., Niikura, T., Takikawa, S., Nishiyama, T., Mizuno, K., Yoshiya, S., Kurosaka, M., 2005 "Impaction Bone Grafting with Hydroxyapatite: Increased Femoral Component Stability in Experiments Using Sawbones," *Acta Orthopaedica*, **76**, 550-554

83. Bergmann, Graichen, F., Rohlmann, A., 1993, “Hip Joint Loading During Walking and Running, Measured in Two Patients,” Journal of Biomechanics, 26, 969-990
84. Phadke, M.S, 1989, “Quality Engineering Using Robust Design,” Prentice-Hall, Englewood, California
85. Dee, K.C., Puleo, D.A., Bizois, R., 2002, An Introduction to Tissue-Biomaterial Interactions, John Wiley and Sons Ltd, New York, NY
86. Kyle, R.F., Winquist, R.A., 2005, “M/DN Femoral Interlocking & Recon Nail Intramedullary Fixation Surgical Technique,” Zimmer, Inc.
87. Egol, K.A., Chang, E.Y., Cvitkovic, J., Kummer, F.J., 2004, “Mismatch of Current Intramedullary Nails with the Anterior Bow of the Femur,” Journal of Orthopedic Trauma, 18, 410-415
88. Harper, M.C., Carson, W.L., 1987, “Curvature of the Femur and the Proximal Entry Point for an Intramedullary Rod,” Clinical Orthopedics, 220, 155-161
89. Zuber, K., Schneider, E., Eulenberger, J., Perren, S.M., 1988, “Shape and Dimension of the Femoral Cavity with Regard to Fit of Intramedullary Implants,” Unfallchirurg, 91, 314-319
90. Bruns, W., Bruce, M., Prescott, G., Maffulli, N., 2002, “Temporal Trends in Femoral Curvature and Length in Medieval and Modern Scotland,” American Journal of Physical Anthropology, 119, 224-230
91. Nobel, P.C., Alexander, J.W., Lindahl, L.J., 1988, “The Anatomical Basis of Femoral Component Design,” Clinical Orthopedics, 235, 148-165

92. Leung, K.S., Procter, P., Robioneck, B., 1996, “Geometric Mismatch of the Gamma Nail to the Chinese Femur,” Clinical Orthopedics, 323, 42-48

93. Johnson, K.D., Tencer, A., 1990, “Mechanics of Intramedullary Nails for Femoral Fractures,” Unfallchirurg, 93, 506-511

94. Damron, T.A., Palomino, K., Roach, S., 1999, “Long Gamma Nail Stabilization of Pathologic and Impending Pathologic Femur Fractures,” Univ Pa Orthopedic Journal, 12, 13-20

95. Gausepohl, T., Pennig, D., Koebke, J., Harnoss, S., 2002, “Anterograde Femoral Nailing: an Anatomic Determination of the Correct Entry Point,” Injury, 33, 701:705

96. Harma, A., Germen, B., Karakas, H.M., Elmali, N., Inan, M., 2005, “The Comparison of Femoral Curves of Contemporary Intramedullary Nails,” Surg Radiol Anat

97. Dittmar, M., 2002, “Functional and Postural Lateral Preferences in Humans: Interrelations and Life Span Age Differences,” Human Biology, 74, 569-585

98. Gilbert, B.M., 1975, “Anterior Femoral Curvature: Its Probable Basis and Utility as a Criterion of Racial Assessment, American Journal of Physical Anthropology, 45, 601-604

99. Gill, W.G., 2001, “Racial Variation in the Proximal and Distal Femur: Heritability and Forensic Utility, Journal of Forensic Science, 45, 791-799

100. Trudell M.B., 1999, “Anterior Femoral Curvature Revisited: Race Assessment from the Femur, Journal of Forensic Science, 44, 700-707

101. Stewart, T.D., 1962, “Anterior Femoral Curvature: Its Utility for Race Identification,” Human Biology, 34, 49-62

102. Zimmer, Inc., Kyle, R.F, Winquist, R.A., 2003, M/DN® Femoral Interlocking & Recon Nail Intramedullary Fixation Surgical Technique

103. Wheeless, C.R., 2009, "Femoral Shaft Frx: Reaming vs Non Reaming," Wheeless Textbook of Orthopaedics, http://www.wheelessonline.com/ortho/femoral_shaft_frx_reaming_and_nailing_maneuver, 26 July, 2009

104. ASM International Handbook Committee, 1990, Metals Handbook, 10th ed., vol. 1, ASM International, Materials Park, OH

105. Strauss, E.J., Schwarzkopf, R., Kummer, F., Egol, K.A., 2008, "The Current Status of Locked Plating: The Good, the Bad, and the Ugly," Journal of Orthopedic Trauma, 22, 479-486

106. Gardner, M.J., Helfet, D.L., Lorich, D.G., 2004, "Has Locked Plating Completely Replaced Conventional Plating?" American Journal of Orthopedics, 33, 439-446

107. Sommer, C., Gautier, E., Muller, M., Helfet, D., Wagner, M., 2003 "First Clinical Results of the Locking Compression Plate (LCP)," Injury, 34, S-B43–S-B45

108. Hussain, P.B., Mohammad, M., 2004, "Failure Analysis of Stainless Steel Femur Fixation Plate," Medical Journal of Malaysia, 59, 180-181

109. Crist, B.D., Assistant Professor, Co-Director of Trauma Services, 2009, Columbia, MO (Personal Communication)

110. Sanders, B.S., Bullington, A.B., McGillivary, G.R., 2007, "Biomechanical Evaluation of Locked Plating in Proximal Humeral Fractures," Journal of Shoulder and Elbow Surgery, 16, 229-234

111. Gardner, M.J., Nork, S.E., Huber, P., Krieg, J.C., 2009, “Stiffness Modulation of Locking Plate Constructs Using Near Cortical Slotted Holes: A Preliminary Study,” Journal of Orthopedic Trauma, 23, 281-287

112. Ratcliff, J.R., Werner, F.W., Green, J.K., 2007, “Medial Buttress Versus Lateral Locked Plating in a Cadaver Medial Tibial Fracture Model,” Journal of Orthopedic Trauma, 21, 444-448

113. Gardner, M.J., Brophy, R.H., Campbell, D., 2005, “The Mechanical Behavior of Locking Compression Plates Compared with Dynamic Compression Plates in a Cadaver Radius Model,” Journal of Orthopedic Trauma, 19, 597-603

114. Stoffel, K., Dieter, U., Stachowiak, G., 2003, “Biomechanical Testing of the LCP – How Can Stability in Locked Internal Fixators be Controlled?” Injury, 34, B11-B19

115. Gardner, M.J., Griffith, M.H., Demetrakopoulos, D., 2006, “Hybrid Locked Plating of Osteoporotic Fractures of the Humerus,” Journal of Bone Joint Surgery, 88, 1962-1967

116. Sumner, D.R., Galante, J.O., 1991, “Determinants of Stress Shielding,” Clinical Orthopaedics and Related Research, 274, 202-212

117. Cowin, S.C., 2001, Bone Mechanics Handbook, CRC Press LLC, Boca Raton, 10-9, 35-10

118. Scholes, S.C., Unsworth, A., 2006 “Investigating the Potential of Implantable Grade PEEK as a Bearing Material Against Various Conterfaces,” European Society for Biomaterials Conference, Nantes, France

119. Massey, L.K., 2005, Effects of Sterilization Methods on Plastics and Elastomers - The Definitive User's Guide and Databook (2nd Edition), William Andrew Publishing/ Plastics Design Library, Norwich, NY